Evolution of two-phase flow in networks of branching microchannels

Yu Song

École Polytechnique

Laboratoire d'Hydrodynamique (LadHyX)

Thèse présentée pour obtenir le grade de

DOCTEUR DE L'ÉCOLE POLYTECHNIQUE
Spécialité : Mécanique

par

Yu SONG

Evolution of two-phase flow in networks of branching microchannels*

*Évolution d'un écoulement diphasique dans des réseaux branchés de microcanaux
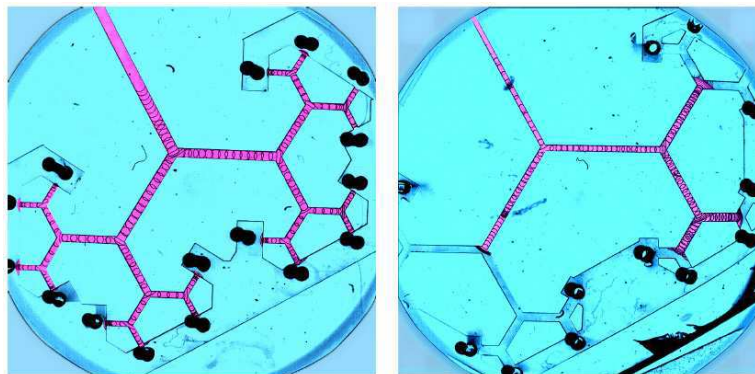
Soutenue le 19 Novembre 2010 devant le jury composé de:

Charles Baroud	Directeur de thèse	École Polytechnique
Paul Manneville	Directeur de thèse	École Polytechnique
Matthias Heil	Rapporteur	University of Manchester, UK
Franck Plouraboué	Rapporteur	IMFT, Toulouse
Marie-Caroline Jullien	Examinateur	ESPCI, Paris
Daniel Isabey	Président du jury	INSERM, Paris

Abstract

The transport of liquid plugs in networks of branching channels is experimentally studied. Liquid plugs are pushed at different driving conditions in a tree-like network of microchannels with widths either narrowing or widening with the generation number. The global flow pattern can be either symmetric or asymmetric, with daughter plugs dividing in synchrony or asynchrony as a function of the driving force and the network geometry. This behavior is explained by plug interactions at work in a fundamental element of the network, which consists of three adjacent bifurcations. When a single plug is pushed at constant pressure, its daughters can reach the exits only if the driving pressure is higher than the thresholds in the network. For a plug pushed at constant flow rate, its daughters can arrive at the exits of the narrowing network even when the flow rate is low. Conversely, in the widening network, only some daughters can reach the exits while others get stuck at intermediate bifurcations. Moreover, a linear relation between the driving pressure and total flow rate in the network is derived and found to be applicable in the presence of successive plugs. In this case, the total flow rate can be influenced by the initial distance between plugs when the driving pressure and plug lengths are fixed. Furthermore, some preliminary results about network reopening through plug ruptures at high pressure driving are also presented.

Keywords: Microfluidics, Networks, Two-phase flow, Liquid plug

Résumé

Nous étudions expérimentalement le transport des bouchons liquides dans les réseaux branchés de microcanaux. Les bouchons liquides sont poussés sous différentes conditions dans un réseau arborescent de microcanaux de largeur croissante ou décroissante avec le numéro de génération. Le motif global d'écoulement peut être symétrique ou asymétrique, avec des bouchons se divisant de manière synchrone ou asynchrone, selon la nature et l'intensité de la force de poussée et la géométrie du réseau. Ce comportement s'explique par des interactions entre bouchons à l'œuvre au sein d'un élément fondamental du réseau composé de trois bifurcations adjacentes. Quand un unique bouchon est poussé à pression constante, ses descendants atteignent les sorties du réseau uniquement si la pression est supérieure aux seuils du réseau. Les descendants d'un bouchon poussé à débit constant, atteignent toujours les sorties d'un réseau de largeur décroissante, même lorsque le débit est faible. Inversement, dans un réseau à largeur croissante, seuls certains descendants peuvent atteindre les sorties alors que les autres restent bloqués aux bifurcations intermédiaires du réseau. De plus, nous montrons qu'une relation linéaire existe entre la pression et le débit total dans le réseau, dont la validité est vérifiée en présence de bouchons successifs. Dans ce cas, le débit total varie avec la distance initiale entre les bouchons, à pression et longueurs de bouchons fixées. Finalement, des résultats préliminaires sont présentés, concernant la réouverture sous haute pression de réseaux par ruptures des bouchons.

Mots-clés: Microfluidiques, Réseaux, Écoulement diphasique, Bouchon liquide

Contents

Chapter 1

Introduction

1.1 Motivation of the study

We are motivated by two-phase flows that take place in the pulmonary airways. Since the airway is coated with a liquid lining, the flow of air can be impeded by discrete plugs that are formed in pathological situations (Grotberg, 1994). In addition, the instillation of liquid into the airway is very common in medical treatments such as partial liquid ventilation and drug delivery (Leach *et al.*, 1996). In these cases, the ultimate distribution of liquid within the pulmonary tree is of great importance but not clearly understood yet. The difficulties include: (1) the nonlinear relation between the local pressure jump and flow rate due to the presence of liquid plugs in the conduit; (2) introduction of bifurcations, which changes the flow behavior and introduces more daughter plugs through plug division; (3) interactions between daughter plugs in distinct subregions of the tree; and (4) flow evolution at different lengthscales resulting from the inherent complexity of the lung structure.

For these reasons, most previous studies have considered either the detailed motion of a single plug in one conduit and one bifurcation or the statistics of liquid transport in the network on a global scale. There remains a large gap between the understanding about the two-phase flow that develops in one straight channel (or one bifurcation) and the global organization of the flow in networks of connected channels. Therefore, we aim to build a simple model, representing the basic building element of the airway structure, which allows experimental investigations of liquid transport in this element with fine control over the parameters and can be adopted in studies about flow in the whole pulmonary tree.

As illustrated in figure 1.1, the complex structure in the conducting zone of the airway, generations 0 to 16, can be simplified as a branching binary tree. We particularly focus on the transport of liquid plugs in the middle section of the lung, generations 9 to 16, where the diameters of bronchioles become small so that microfluidic techniques are relevant. Networks consisting
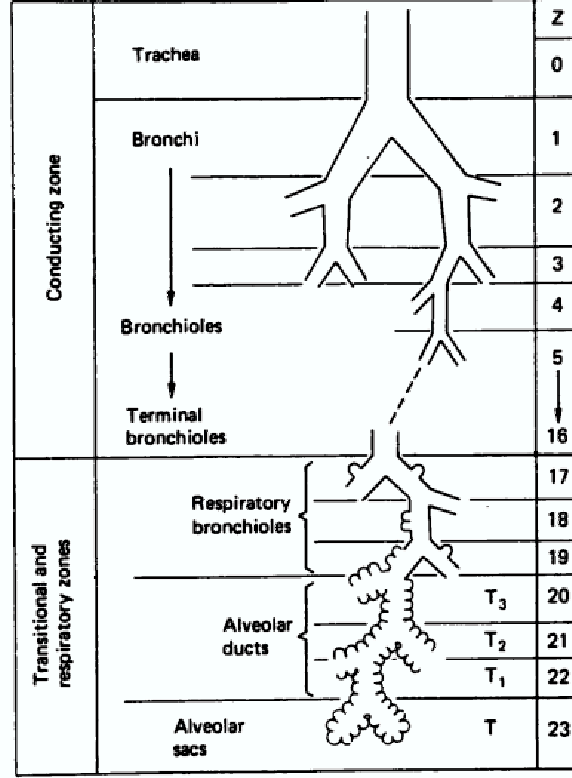
Figure 1.1: Simplified image of the structures in the pulmonary airway. There are branching binary network in the conducting zone, generations 0 to 16, and clusters of small ducts in the respiratory zone, generations 17 to 23. Taken from (Weibel, 1984).

of a few generations of branching microchannels are made to model the binary structure of the airway. By injecting liquid plugs into the network and pushing them at different pressures or flow rates, we can record the motion of plugs with the help of a microscope and fast camera. Based on the images thus obtained, the flows, including plug advancements across generations and divisions at bifurcations, are studied.

1.2   Two-phase flows in networks

1.2.1   Liquid plug in the pulmonary airway

The pulmonary airway presents a branching network of complex structures which is illustrated in figure 1.2. The inner airway is coated with a thin layer of liquid, which protects the underlying cells from drying and traps inhaled particles that are dangerous to the lung (Grotberg, 2001). However, when the volume of liquid is sufficiently large, the lining may experience a surface-tension-driven (Rayleigh-Plateau) instability which causes the closure of airways, for example by the formation of liquid plugs (Halpern & Grotberg, 1992; Otis et al., 1993). The schematic
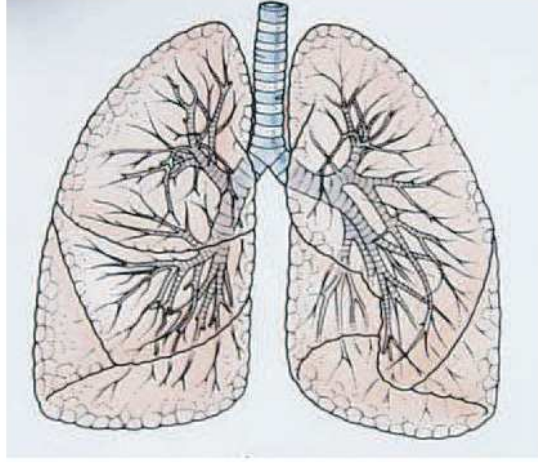
Figure 1.2: Image illustrating the structures of the airway in the lung.
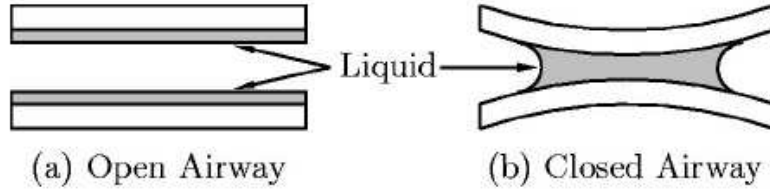
Figure 1.3: The schematic picture of a branch of the airway. (a) Open with the liquid lining. (b) Closed by a liquid plug. Taken from (Majumdar *et al.*, 2003).

pictures show a section of the airway that is open, figure 1.3(a), and closed by a liquid plug, figure 1.3(b).

The airway closure caused by surface-tension-driven instabilities has been studied experimentally (Macklem *et al.*, 1970) and theoretically (Heil *et al.*, 2008). In Heil's paper, they described the mechanics of plug formation by instabilities of the liquid lining and illustrated the possible equilibrium states of the liquid lining in the axisymmetric rigid airways, as shown in figure 1.4. Supposing that the liquid had a lining with uniform thickness as shown in image (a), the instability introduced by some perturbation caused the deformation of the lining, with the possible new configurations shown in figures 1.4(b) and (d). In all the configurations, the air-liquid interfaces had to be a surface of constant mean curvature to avoid motion induced by curvature variation. The resulting state, whether a liquid plug could be formed, depended on the initial thickness of the liquid film, h_0 noted in figure 1.4(a). A minimum value of h_0, h_{min}, was required to form a liquid plug. When $h_0 < h_{min}$, the lining would be stabilized as the unduloid shaped interface (figure 1.4(b)).
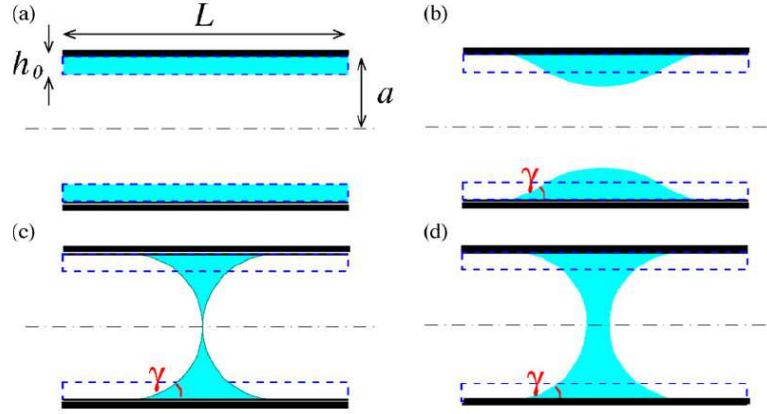
Figure 1.4: Four possible equilibrium states of liquid lining in an axisymmetric rigid airways: (a) an axially uniform film of liquid; (b) an unduloid shaped interface; (c) a minimum liquid bridge; (d) a liquid plug of finite thickness. Taken from (Heil *et al.*, 2008).

Plug formation is naturally present in the breathing cycle of healthy people, which happens near the end of expiration when the airway diameter is small (Grotberg, 2001). However, the closure of airway may cause respiratory problems if it remains for a long time. Moreover, the airway can be occluded in pathological situations (Grotberg, 1994) such as asthma, pneumonia, or respiratory distress syndrome when the flow of air is blocked by liquid plugs. In these situations, the subsequent reopening of the airway becomes an important issue (Grotberg & Jensen, 2004). Previous studies have investigated the reopening in many aspects, ranging from (1) the effects of viscoelasticity of the liquid lining (Hsu *et al.*, 1996; Low *et al.*, 1997) to (2) dynamic instabilities of pressure during the inflating process (Alencar *et al.*, 2002), (3) the sequence of sound waves associated with the explosive opening (Alencar *et al.*, 2001) and (4) the mechanical model related to the lung structure (Majumdar *et al.*, 2001). These studies have been performed using different approaches, such as experiments, simulations, and theoretical analysis, and it is normally acknowledged that the reopening process involves the dynamics of the liquid lining and/or the elasticity of the airway.

On the other hand, the instillation of liquid, especially surfactant, into the pulmonary airway is very common in medical treatments. Surfactant insufficiency can result from either prematurity or from protein leakage from the vascular system as a result of a septic infection. Particularly with premature babies, it may be necessary to deliver surfactant to reopen and stabilize airways (Bertram & Gaver, 2005). These treatments include partial liquid ventilation, in which ventilation with perfluorocarbon liquids improves lung function in conditions such as surfactant deficiency and dysfunction (Leach *et al.*, 1996), and Surfactant Replacement Therapy, which can
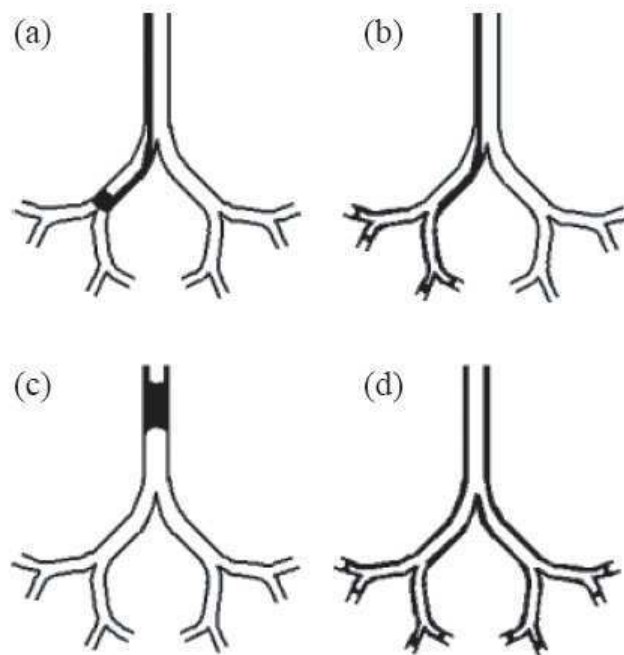
Figure 1.5: Schematic images of the liquid transport and distribution in two cases. Case A: (a) initially inserted liquid and (b) localized distribution of liquid after inspiration. Case B: (c) a plug formed in the trachea and (d) more uniform distribution of liquid after inspiration. Taken from (Cassidy *et al.*, 2001*a*).

be employed to reduce the incidence of respiratory distress syndrome for premature neonates (Engle & the Committee on Fetus & Newborn, 2008).

In these cases of drug delivery, the only available control over the plug distribution is at the entrance of the network, at the level of the patient's trachea. Once the liquid is injected, little is known, in reality, about the ultimate distribution of liquid within the pulmonary tree, although some people have attempted to investigate the delivery process (Halpern *et al.*, 1998; Espinosa & Kamm, 1999; Cassidy *et al.*, 2001*a*; Bull *et al.*, 2004; Kleinstreuer *et al.*, 2008). Using an experimental method, Cassidy *et al.* (2001*a*) traced the transport of the liquid bolus of surfactant after it was injected into the trachea of an excised rat lung and found that the formation of plugs led to more uniform distribution of surfactant in the lung. Two methods were used in their experiments: in Case A, the liquid inserted into the trachea fell very rapidly into the airways and drained by gravity; Case B involved the formation of a plug in the liquid instillation. Images were given for the liquid distribution before and after the inspiration in two cases, as shown in figure 1.5. For the liquid that was drained by gravity, the formation of plug could happen in a subsequent generation, as shown in figure 1.5(a), when the liquid was driven through the airway by inspiration. This resulted in a limited liquid dispersion in the deeper airways, image (b). However, when the liquid was instilled as a plug as shown in figure 1.5(c), it

was transported in a homogeneous pattern, image (d). At the same time, it was also found that there was liquid deposited on the airway wall behind the plug that was advancing.

1.2.2 Immiscible displacement in porous media

The motion of immiscible fluids in complex geometry, such as porous media, has also been a typical problem, in which people have been interested for a long time. The multiphase flows in porous structures can be found in many fields such as agriculture, chemistry, biology, construction and petroleum engineering (Sahimi, 1993). Examples include oil displacement process in petroleum industry (Chandler *et al.*, 1982), flows of water and air in the vadose zone in the subsurface environment (Olbricht, 1996) and the flow of aqueous-liquid-gas mixtures in the underground reservoir rocks (Gerritsen & Durlofsky, 2005).

For all these phenomena, the basic issue lies in the displacement of multiphase fluids in structured pores, in which little mechanism is applicable for the complex interaction among capillary force, viscosity and gravity. People have studied the global behavior of the flow by local units either by simulations (Koplik, 1982) or statistical approach (Larson *et al.*, 1981). With the Laplace Law expressing the relation between the capillary pressure and interface curvatures, Lenormand investigated, experimentally and theoretically, the mechanism of displacement of one fluid by another in etched networks with pores (Lenormand *et al.*, 1983; Lenormand & Zarcone, 1985). Good agreement was found between experiments and calculations. Two mechanisms involved in the meniscus displacement were summarized in his later paper (Lenormand, 1990), as shown in figures 1.6 and 1.7.

When the wetting liquid was invading the pores, the deformation of interface in the pore (figures 1.6(a) and (b)) introduced a variation of capillary pressure. At a given pressure, the meniscus touched the opposite wall, figure 1.6(c), and the liquid "instantaneously" invaded the adjacent channels toward the next pores as shown in figure 1.6(d). In the other case, the liquid first advanced along the rough walls of adjacent channels as shown in figure 1.7(a), which formed a film coating the channels. However, at a certain pressure, the motion of the film turned out to be unstable, resulting in the formation of a plug that filled the channel and helped invading the pore, figure 1.7(b). It was also found that in a media with small pore-to-throat ratio (aspect ratio), where the size of the pore was small compared to the channel connecting the pores, the liquid invaded the pore through interface advances. In media with large aspect ratio, the main mechanism in imbibition was the collapse in the adjacent channels, as shown in figure 1.7.

Although these findings seem direct at a single pore scale, they can lead to complicated interactions at the macroscopic scale, for example in the wetting process on structured materials (Courbin *et al.*, 2007). More broadly, the displacement of multiphase interfaces and the ultimate
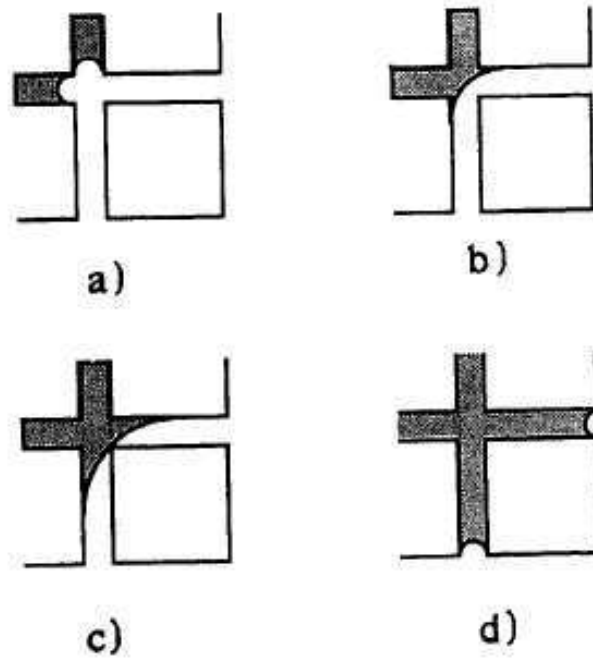
Figure 1.6: Mechanics of pore invasion of the wetting liquid (black). (a) and (b): The radius of curvature of the meniscus increases as the liquid invades the media. The interface touches the wall (c) and the fluid invades the adjacent channels (d). Taken from (Lenormand, 1990).
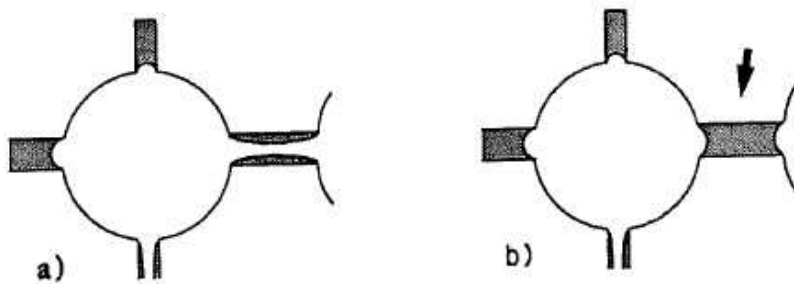
Figure 1.7: Mechanics of collapse of the wetting fluid (black). The wetting liquid advances along the wall (a) until its film becomes unstable and collapses in the channel (b). Taken from (Lenormand, 1990).

macroscopic distribution of different fluids vary according to the global topology of the porous media (Berejnov *et al.*, 2008; Xu *et al.*, 2008).

1.2.3 Microfluidic approach

Microfluidic techniques, the control and regulation of flows along with the design and fabrication of channels at small scale, have attracted much attention in the past decades (Stone *et al.*, 2004). Besides the scale, microfluidic problems are characterized by small Reynolds numbers. The Reynolds number $\mathrm{Re} = \rho_l U D/\eta$ compares fluid inertia with viscous effects. In this formula, ρ_l is the fluid density, U the characteristic velocity, D the characteristic diameter and η the fluid viscosity. In most microfluidic regimes, Re is very small and inertial forces are negligible, so that the flow is governed by the Stokes equations. In studies involving bubbles or drops, the Bond number is often used to compare the gravity to the surface tension. It is defined as $\mathrm{Bo} = \rho_l a D^2/\gamma$, where a denotes the gravity acceleration and γ is the surface tension. The capillary length L_C for a given fluid can be known when $\mathrm{Bo} = 1$. If $D < L_\mathrm{C}$, $\mathrm{Bo} < 1$ and the effects of gravity become small compared to surface tension effects. Since L_C is generally around a few millimeters for most liquids, the effects of gravity can be neglected at micro scales. There is another important parameter, the capillary number $\mathrm{Ca} = \eta U/\gamma$, which compares the fluid viscosity with surface tension. Ca distinguishes the flow by the importance of surface effects over viscosity as the scale varies.

From the technical point of view, the introduction of soft lithography into the field of microfabrication was a great progress in microfluidics by simplifying and speeding the fabrication process (Xia & Whitesides, 1998). Once the patterned surface with microstructures is fabricated, the microchannels can be made of polydimethylsiloxane (PDMS) through a simple procedure, which can be repeated to fabricate more than 50 replicas. Since then, microfluidics has developed rapidly in many related fields such as chemical reactions in networks (Delamarche *et al.*, 1998; Song *et al.*, 2003), in vitro biological studies about tissues (Huh *et al.*, 2007), physical mixing of two fluids (Gunther *et al.*, 2005; Garstecki *et al.*, 2005) and liquid transport through passive pumps driven by capillary forces (Zimmermann *et al.*, 2007; Gervais & Delamarche, 2009).

At the same time, microfluidics has opened a wide range of possibilities for addressing questions of complex flows, e.g. studies about multiphase flows (Darhuber & Troian, 2005; Gunther & Jensen, 2006), which refer to flows in microscale where surface tension is important. Due to the ability to offer fine control over the geometry and provide detailed optical access to the fluid behavior, microfluidic devices have also been employed in modeling flows in networks (Lenormand *et al.*, 1983; Krishnamurthy & Peles, 2007; Berejnov *et al.*, 2008) and in the investigation
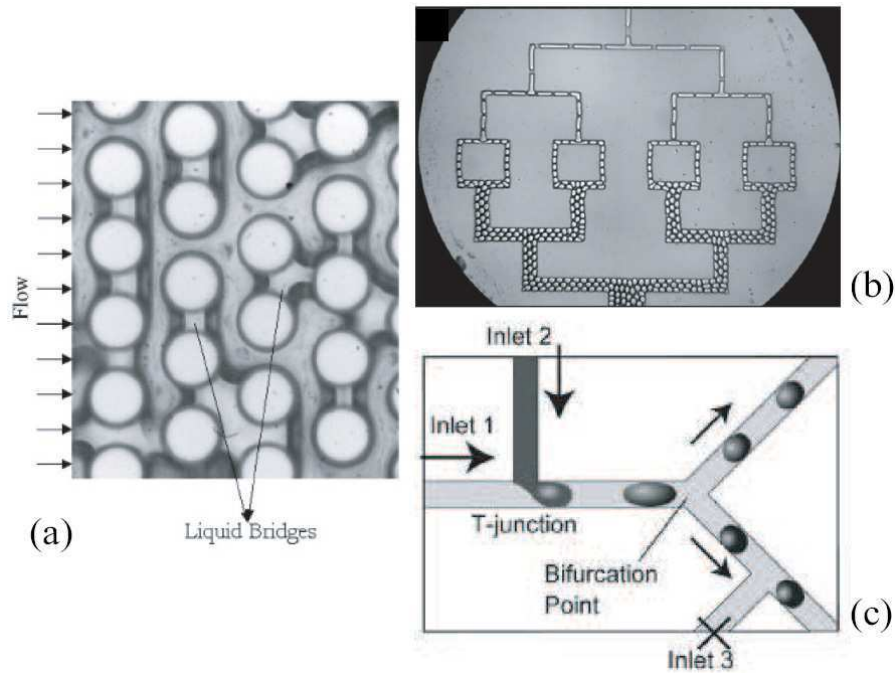
Figure 1.8: (a) Gas-liquid flow over structured surface with micropillars. When the gas flows at a high velocity, here 14 m/s, liquid bridges are formed between pillars. (Krishnamurthy & Peles, 2007). (b) Droplet breakups at T shape junctions. Small droplets are formed during sequential breakups of drops at successive junctions and the drop sizes can be controlled by changing the lengths of the daughter channels. (Link *et al.*, 2004). (c) Hydrodynamic control of droplet division at a bifurcation. When no liquid is introduced through Inlet 3, the droplets have equal divisions as shown here. When the continuous phase is flowing into the system from Inlet 3, smaller droplets will go into the lower branch. (Yamada *et al.*, 2008).

of flows involving the passage of droplets through bifurcations (Link *et al.*, 2004; Schindler & Ajdari, 2008; Yamada *et al.*, 2008).

Some previous studies about two-phase flows in complex geometry, in which microfluidics is employed, are illustrated in figure 1.8. Figure 1.8(a) is obtained in the investigation of gas-liquid flow over structured surface with micropillars, where the flow patterns vary according to the velocities of the injected gas and liquid. Liquid bridges are formed during the liquid traverse of the pillars when the gas velocity is high. Figure 1.8(b) illustrates the study of droplet breakups at bifurcations. The presence of successive bifurcations is found to be helpful in forming small droplets through the breakups of long drops. Figure 1.8(c) shows that the ratio between the sizes of the daughter droplets can be controlled by varying hydrodynamic situations in two daughter branches.

Microfluidics has also been proposed recently as a way to model branching geometry in the lung, at least in the generations where gravity and inertial effects are negligible (Baroud *et al.*, 2006). The relevant region is characterized by lengthscale below the capillary length and small

Reynolds numbers. The two criteria $D < L_C$ and $Re < 1$ are met in a large range of generations of the lung, starting from about generation 9 through the respiratory bronchioles, to around generation 20 (Weibel, 1984).

1.2.4   Flows in complex geometries

In the fluid flows in networks, complex dynamics can always result from the nonlinear relation between the local pressure and flow rate, for example when the flow propagates in compliant conduits (Hazel & Heil, 2003) or in the presence of immiscible interfaces (Howell *et al.*, 2000). In such situations, the local flow-rate fluctuations lead to instantaneous, global reequilibration of the pressure, thus producing long-range couplings in the flow. This can play a dominant role for flows in porous or biological media, where the evolution of multiphase flows occurs through a competition between viscous and capillary effects, both of which are influenced by the local details of the geometry. Generalizing these studies can yield understandings of many mysterious phenomena in nature: for example, the water transport in plants (West *et al.*, 1999; McCulloh *et al.*, 2003), the physiological organization of animals' vascular systems (Murray, 1926) and the exploration of optimal transport networks (Katifori *et al.*, 2010; Corson, 2010). Furthermore, the large scale rearrangement in complex geometries, involving the modeling of fluid transport, social interactions and disease propagation in networks, has also been a challenging issue of long standing interest with many related applications (Strogatz, 2001; Newman, 2003).

1.3   Preliminary understanding of the physics

Many efforts have been made to study the contact of two kinds of liquids and a solid surface in the previous decades (Dussan, 1979). However, the difficulties arise due to the interactions between the immiscible interfaces and the complex geometry, which can significantly affect the statics and the dynamics of the liquid flow. Some fundamental results are found in previous studies about the moving contact line on horizontal (Tanner, 1979) or rough surfaces (Jansons, 1985) and in capillaries (Hoffman, 1975). When considering the flow in a confined geometry, the contact dynamics as well as the geometry constraint become more important (Ajaev & Homsy, 2006). Bretherton (1961) made great contribution to the investigation about the motion of a long bubble in tubes. The nonlinear relation between the driving pressure P and bubble's capillary number Ca was found to be $P \propto \mathrm{Ca}^{2/3}$ when the capillary number is very small (Ca $<$ 5×10^{-3}). Predictions of the bubble profile in the capillary tube could be made by using this model. Later on, Wong *et al.* (1995) studied the bubble motions in different polygonal capillaries and the pressure drop across the bubble was found to scale as $\mathrm{Ca}^{2/3}$. A similar problem was

Liquid plug

Flow
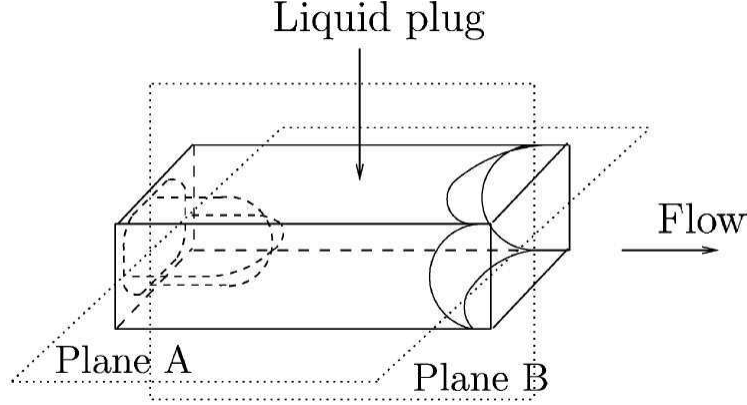
Plane A

Plane B

Figure 1.9: Schematic of a plug of wetting liquid in the rectangular channel. Planes A and B denote the in-plane and in-thickness sections. The curvatures of the air-liquid interfaces in the two planes are illustrated. Taken from (Ody *et al.*, 2007).

investigated by Hodges *et al.* (2004) who considered a viscous drop in a cylindrical tube and the liquid viscosity was found to have an effect on the film thickness around the drop.

Recently, some characteristics of the drop motion in milli- or micro-sized tubes have been found (Stone *et al.*, 2004; Fujioka & Grotberg, 2004; Fuerstman *et al.*, 2007). The pressure jump in the tube due to the presence of drops was studied numerically (Fujioka & Grotberg, 2004) and experimentally (Aussillous & Quéré, 2000; Pehlivan *et al.*, 2006). A nonlinear relationship between pressure difference and flow rate of the drop was introduced by surface tension, through the addition of Laplace pressure (Bico & Quéré, 2001; Ody *et al.*, 2007). For a single plug of wetting liquid in a straight rectangular microchannel, the relation between the driving pressure and the plug's capillary number was obtained by taking into account the changes of the interface curvatures in both Plane A and B, as shown in figure 1.9. While the plug was advancing, the front interface, illustrated by solid curves deformed and exhibited a non-zero contact angle with the channel wall although the liquid was wetting. Meanwhile, a thin film of liquid was deposited on the walls of the channel behind the plug, which changed the curvature of the rear interface illustrated by dashed curves. Based on this approach, the following formula was found to be valid for a long plug of wetting liquid moving at low capillary numbers in a rectangular microchannel whose width was much larger than the height: $P_{\text{dr}} = F\text{Ca} + G\text{Ca}^{2/3}$, in which P_{dr} was the driving pressure and F,G were functions of the channel geometry, the physical and geometrical properties of the plug.

While these nonlinearities already appeared in flow through straight channels, they were amplified when the plug passed a bifurcation since the interfaces must strongly deform in this case, which was also explored in (Ody *et al.*, 2007): The presence of a bifurcation could lead to
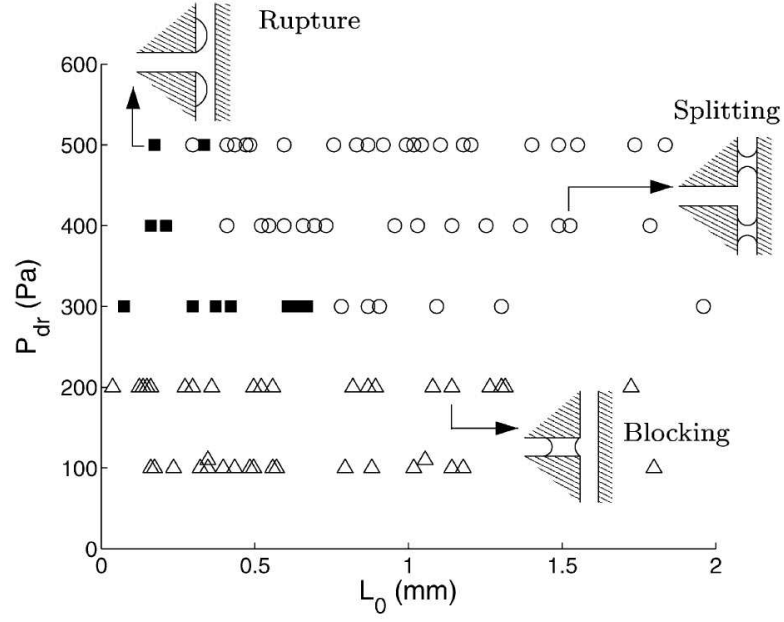
Figure 1.10: Phase diagram for the plug behavior at a T-bifurcation. Taken from (Ody *et al.*, 2007).

a local blockage if the pressure was below some threshold value. Instead of passing through the bifurcation, the plug stopped after it entered the bifurcation (experimental data points denoted by $\triangle$ in figure 1.10). When a short plug was pushed at a pressure higher than the threshold, it ruptured ($\blacksquare$) and the maximum length for a plug to rupture L_{crit} was found to vary as a function of the driving pressure. If the plug was longer than L_{crit} and pushed by a pressure higher than the threshold, it passed through the bifurcation and split into two daughters. These were summarized in figure 1.10 as the phase diagram for plug behavior at a T-bifurcation.

The existence of a threshold pressure was also verified in capillary-valve experiments, where the flow was regulated simply due to the strong variation of the channel geometry, both in rectangular channels (Man *et al.*, 1998; Cho *et al.*, 2007) and in axisymmetric tubes (Chen *et al.*, 2008). A sequence of images showing how this kind of valve works is given in figure 1.11, where a minimum value of pressure is required across the liquid (black part inside the channel) to make the valve burst. This pressure can be calculated at the stage when the liquid interface is just about to burst as shown in figure 1.11(b). After that, the liquid can flow through the valve, figure 1.11(c). The flow is controlled by just changing the driving pressure and the capillary burst valves are widely used in Lab on a CD applications (Madou *et al.*, 2006; Chakraborty *et al.*, 2009), chemical assay (Duffy *et al.*, 1999; Lai *et al.*, 2004) and physics exploration (Vig *et al.*, 2009). When several valves are connected in a predesigned system, multiple steps of experiments can easily be implemented (LaCroix-Fralish *et al.*, 2009).
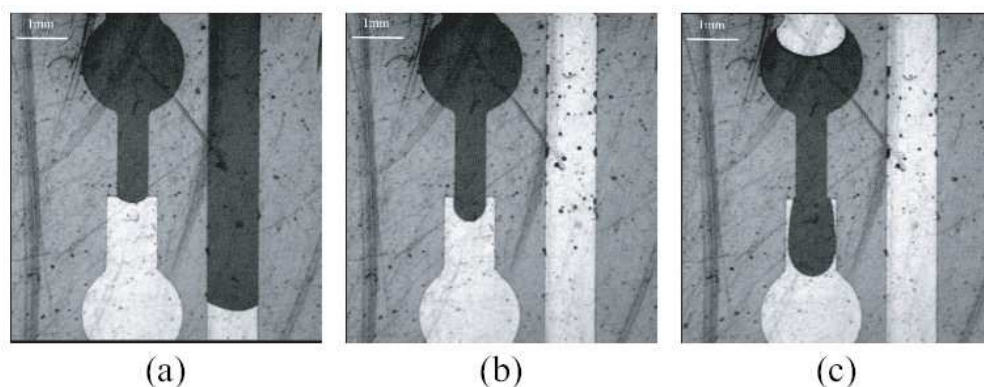
Figure 1.11: Image sequence of the bursting of a capillary valve, where the black part represents liquid. (a) The liquid interface touches the valve edge at the center of the left channel. (b) The very moment just before the valve bursts. (c) The valve has burst, which makes the liquid flow into the lower chamber. Taken from (Cho *et al.*, 2007).

In the case of fluid mechanics, the introduction of bifurcation can further change the behavior of two-phase flow containing bubbles or droplets (Engl *et al.*, 2005; Jousse *et al.*, 2006). For instance, the symmetry of the bubble splitting at a bifurcation depends on the flow's capillary number and the angle the bifurcation plane makes with the horizontal (Calderon *et al.*, 2005). When a liquid plug flows through a junction and divides into two daughters, the sizes of daughter plugs will be influenced by the liquid volumes in the downstream branches (Cassidy *et al.*, 2001*b*). All these effects make the flow more complicated, especially in the presence of a few bifurcations. Therefore, although people have studied flows in networks consisting of many bifurcations theoretically (Corson, 2010) and numerically (Kitaoka *et al.*, 1999; van Ertbruggen *et al.*, 2005), there are few experimental observations where the flow can be realized under fine control.

1.4 Outline of the thesis

In this thesis, we start from the criteria for choosing the network geometry to model the structure of the airways, followed by the introduction of plug motions in the straight channel and across the bifurcation in Chapter 2. The plug motion in the straight channel is predicted by the formula expressed in (Ody *et al.*, 2007), which provides a general idea of the flow. Meanwhile, the capillary pressure variation due to the interface deformations during the plug's passage through a bifurcation is discussed in term of adding a capillary pressure difference across the plug.

A detailed description of the experimental setup is given in Chapter 3. Contents of this part include the procedure of microfabrication, an illustration of the network geometry, the

experimental configurations and realizations. There are also discussions about the fundamental observations and measurements.

Experimental investigation of the transport of a single plug in the network is presented in Chapter 4. A single plug injected into a binary network of five generations of narrowing channels is pushed either at constant pressure or at constant flow rate. Different flow behaviors are found for pressure and flow rate drivings at different values. Moreover, the transport of liquid can be strongly modified when the plug is pushed at constant flow rate in the network with widening channels.

Further, the flow involving a train of plugs pushed at a constant pressure is explored in Chapter 5. These experiments are done in the narrowing network when a few plugs are injected into the network and flow through different generations. A linear relation between the driving pressure and the total flow rate is derived and found to account for the resistance associated with daughters of one plug in the network. This relation is proved to be applicable in the presence of a train of successive plugs.

Besides the transport of liquid plugs in the network, some preliminary results on the reopening process of airways occluded by a random distribution of liquid plugs are presented in Chapter 6. A straight channel or a network is initially closed by liquid plugs, which have a random or quasi-random distribution, and later opened by breaking plugs at a very high pressure drop between the channel inlet and exits. Since the plugs are broken successively in a very short time, this reopening process is considered as a result of cascades of plugs ruptures.

The last chapter is devoted to our conclusion and some perspectives for future work.

Chapter 2

Models of the plug motion

2.1   Description of the network

The network considered in the thesis is designed in this way: there are several generations of branching channels, which have the same shape but different sizes. At each generation, the cross-section area of the channel is rectangular with a height $h = 50$ μm and width w which changes with the generation number at a constant rate ρ. The generation number starts from 0 so the channel width in the ith generation $(i \geq 1)$ is $w_i = w_{i-1}\rho = w_0\rho^i$, where the subscript denotes the generation number and w_0 is the width of the first generation. The channel length decreases at another ratio $\rho' < 1$, which avoids the intersection of branches in the same generation. The angle α, which the daughter channel makes with the parent channel as shown in figure 2.1, measures half the angle between the two daughter branches of the same origin and is kept constant in the network.

The top view of an example network is shown in figure 2.1, where the numbers indicate the generation number of the channel. There are eight generations in total. The width ratio $\rho = 0.6$ and the bifurcation half-angle is $\alpha = 45°$. A basic unit of three connected channels is taken out from the network and the perspective view is zoomed in figure 2.2. This unit consists of one parent channel in generation i and two daughter channels in generation $i+1$, and is repeated in the network. The dimensions of channels are labeled in the figure, the height h and width w_i (or $w_{i+1} = w_i\rho$) on the cross-section as well as the channel length L_{channel} perpendicularly to the cross-section.

For networks with the channels of same size in generation 0, the channel widths can be different in other generations due to the width ratio ρ. Since $w_i = w_0\rho^i$, the channels get narrower with the generation number when $\rho < 1$ while becoming wider in networks with $\rho > 1$. This can be seen in figure 2.3, where the variations of channel widths in networks with ρ ranging from 0.3 to 1.3 are plotted by fixing $w_0 = 720$ μm.

15
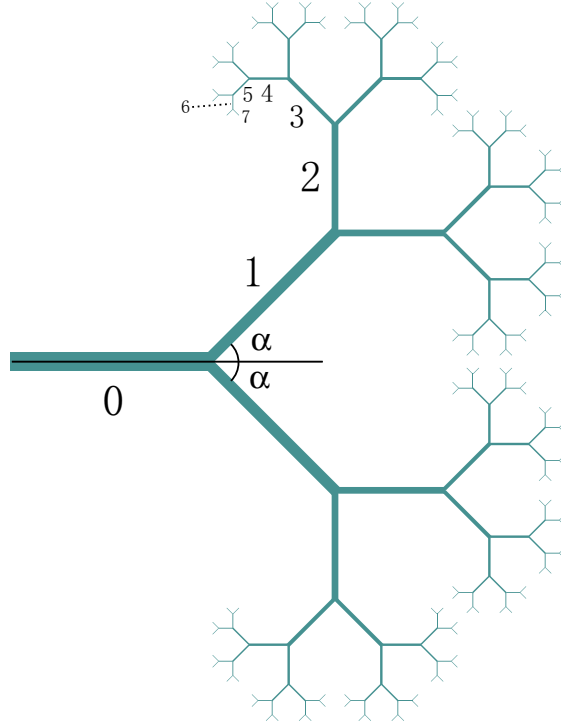
Figure 2.1: Top view of a network with eight generations of branching channels to illustrate the design of networks. The width ratio $\rho = 0.6$ and the bifurcation half-angle $\alpha = 45°$.
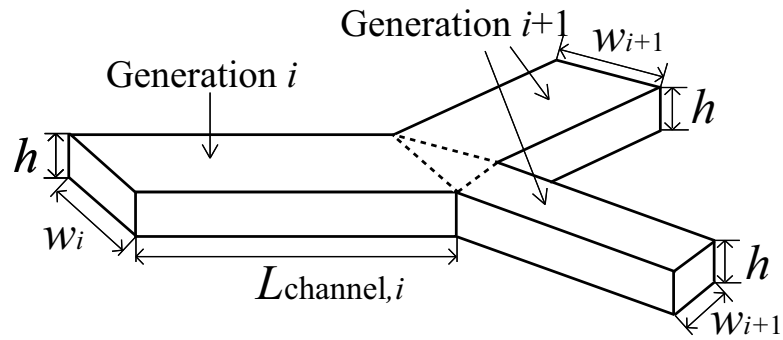
Figure 2.2: Perspective view of the basic unit consisting of one parent channel in generation i and two daughter channels in generation $i+1$. The cross-section of each channel measures $h \times w$, with w varies with the generation number and the channel length is denoted as L_{channel}. The angle between two daughter channels is 2α as shown in the top view in figure 2.1.
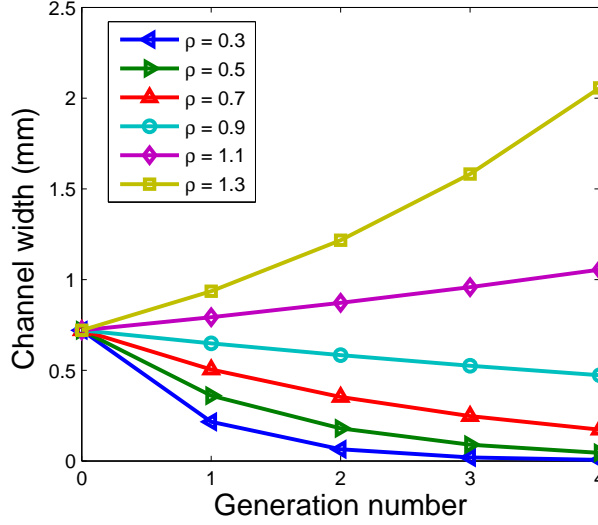
Figure 2.3: Variation of channel width with the generation number. The width of the first generation is $w_0 = 720$ μm and the width ratio ρ changes from 0.3 to 1.3.

When a liquid plug is injected into the network from generation 0 and then pushed through, it will advance across successive generations and divide into two daughters when passing a bifurcation. We assume each plug divides into two daughters of equal size, which also agrees with experimental observations, so all the plugs in the same level of generation have the same length L_i. The plug length varies as $L_i = L_0/(2\rho)^i$ according to mass conservation, where L_0 is the initial length of the plug measured in the first generation.

For a network with $\rho < 0.5$, the daughter becomes longer while the plug is advancing through different generations. When $\rho = 0.5$ all the plugs have the same length in different generations. The plug length becomes smaller as the plug moves in a network with $\rho > 0.5$. This is summarized in figure 2.4(a) where $L_0 = 2$ mm and the width ratio of the network changes from 0.3 to 1.3. Since the channel length decreases at the ratio ρ', which agrees with the fact that the bronchiole sizes decrease in the airway, it is reasonable that the plug length also decreases with the generation number. Otherwise the plugs in the later generations may fill the short channels, for example when $\rho = 0.3$, which will change the flow characteristics. Therefore, the networks with $\rho > 0.5$ is mainly considered and figure 2.4(a) is zoomed at the curves for $\rho > 0.5$ in 2.4(b). The rate of the plug length variation increases when ρ increases, which means that the plug is shortened very quickly through generations. The initial plug injected has to be long enough to avoid the plug breaking because of small size in the later generations, especially when $\rho > 1$.

The plug has different types of motion according to its position in the network, as shown in figure 2.5. It can move in the straight channel, when both the interfaces are inside the channel as
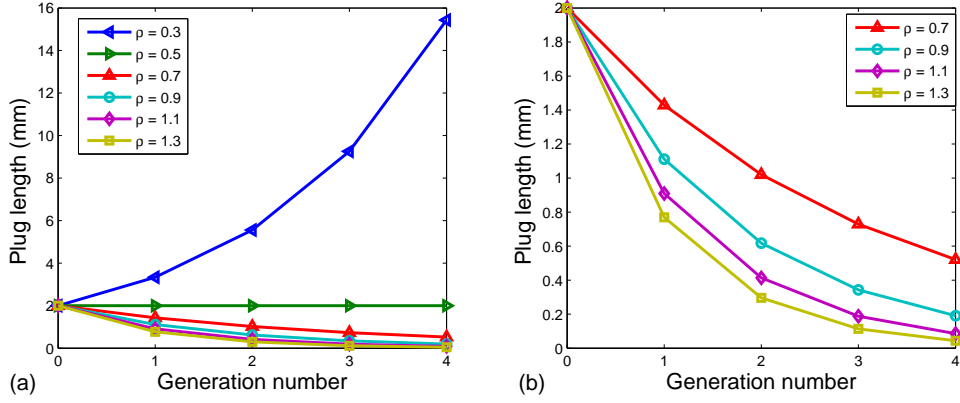
Figure 2.4: Variation of plug length with the generation number. The initial plug length $L_0 = 2$ mm and the width ratio of the network changes (a) from 0.3 to 1.3 and (b) from 0.7 to 1.3. For $\rho < 0.5$, L_i increases with the generation number i, remains the same for $\rho = 0.5$ and decreases with i for $\rho > 0.5$.
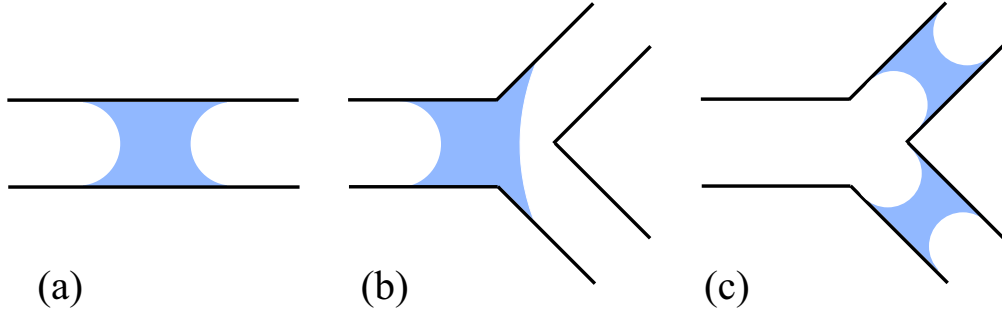
Figure 2.5: Plug motions in the network. (a) Moving in the straight channel. (b) Passing through a bifurcation. (c) Divided into two daughter plugs that move in their respective channels.

shown in (a), or pass the bifurcation, when at least one interface is at the bifurcation (b). After its passage through the bifurcation, the plug divides into two daughters as shown in figure 2.5(c) and the daughters continue the behavior of their parent as shown in (a). Basically, there are two types of motions, i.e. either the plug moves in the straight channel or it passes the bifurcation.

In the following two sections, we model the two types of plug motions separately and assume the switch between them is instantaneous. On one hand, the pressure–flow rate relation in (Ody *et al.*, 2007) is used to obtain quantitative variations of pressure drop and flow rate for the plug in the straight channels. The flow behavior is generally predicted. On the other hand, for a plug in a bifurcation, the deformation of its interfaces due to the geometry change introduces a strongly nonlinear evolution of the pressure with the plug's position. A threshold pressure associated with the bifurcation is calculated.

2.2 Plug in the straight channel

2.2.1 Nonlinear relation between pressure and flow rate

The presence of one liquid plug in a straight channel with rectangular cross-section introduces a resistance to flow through its viscosity and surface tension. The relation between the visco-capillary pressure P_{vc} and the plug's capillary number Ca$= \eta U/\gamma$ can be written as (Ody *et al.*, 2007):

$$P_{\mathrm{vc}} = F(w)L\mathrm{Ca} + G(w)\mathrm{Ca}^{2/3}, \tag{2.1}$$

in which η and γ are the viscosity and surface tension of the liquid, U is the plug velocity, L is the plug length, $F(w)$ and $G(w)$ are expressed as follows:

$$F(w) = \gamma \left[\frac{12}{h^2} \left(1 - 6\frac{2^5 h}{\pi^5 w} \right)^{-1} \right] \tag{2.2}$$

$$G(w) = 2\gamma\beta \left(\frac{1}{h} + \frac{1}{w} \right) \tag{2.3}$$

where h and w are the height and the width of the channel. β is a nondimensional coefficient obtained from Bretherton's and Tanner's laws (Hoffman, 1975; Bico & Quéré, 2001). For the same liquid, $F(w)$ and $G(w)$ are functions of the channel geometry. Equation (2.1) is valid for a long plug that moves in a rectangular channel with large aspect ratio w/h. The linear part represents viscous effects, which change with the channel geometry and plug length. Meanwhile, the capillary effects introduced by the air-liquid interfaces are expressed by the nonlinear part, which also changes with the channel geometry.

2.2.2 Flow rate evolution under constant pressure

When a single plug is pushed at a constant pressure, the velocity of its daughters in generation i, U_i, varies with the generation number, which results from the variation of $F(w)$ and $G(w)$ in (2.1) due to channel sizes and plug lengths. For every single daughter plug in a given generation i, (2.1) can be rewritten as:

$$P_{\mathrm{dr}} = F(w_i)L_i\mathrm{Ca}_i + G(w_i){\mathrm{Ca}_i}^{2/3}. \tag{2.4}$$

Here P_{dr} is the constant driving pressure, w_i is the channel width in the ith generation and L_i is the length of the daughter plug with the assumption of equal division at every bifurcation. Ca_i is thus calculated based on the velocity of a daughter plug U_i, which is shown in figure 2.6. All the parameters related to the calculation are given in table 2.1. The velocities in the first
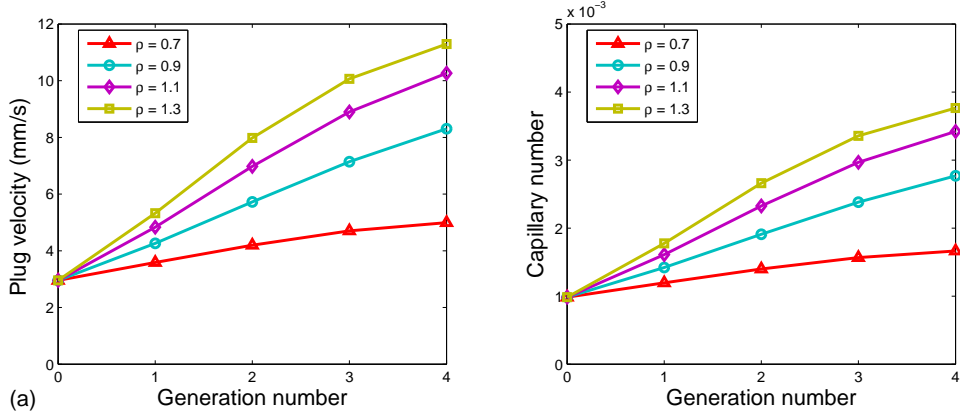
Figure 2.6: Evolution of plug velocity (a) and capillary number (b) in the first five generations of the network when $L_0 = 2$ mm and $P_{dr} = 250$ Pa. $w_0 = 720$ μm and the width ratio ρ varies from 0.7 to 1.3. The plug velocities are obtained at different generations and connected by a single line. The velocity increases with the generation number. The Capillary number is very small and has the same pattern of variation with velocity.

Table 2.1: Parameters for calculating the velocities in the network.

Liquid viscosity	Surface tension	Driving pressure	Length of the initial plug
η (Pa s)	γ (N/m)	P_{dr} (Pa)	L_0 (mm)
5×10^{-3}	15×10^{-3}	250	2
Channel height	Initial channel width	Width ratio	Nondimensional coefficient
h (μm)	w_0 (μm)	ρ	β
50	720	0.7 - 1.3	16

five generations are plotted according to the experimental realization, in which an initial plug of 2 mm long is pushed at 250 Pa into a network with $w_0 = 720$ μm (see Chapter 3 for more details), although (2.4) is valid for networks of any levels of generations.

When the pressure difference between the entrance and the exits of the network is constant, the velocity of the daughter plug varies at different generations. In figure 2.6, these values of plug velocities are calculated at different generations while taking geometry parameters of the branches and the isolated data points are connected by a single line to improve the visualization. The velocity of daughter plug increases with the generation number and all the Capillary numbers are very small. The plots of the Capillary number in figure 2.6(b) have the same pattern as in 2.6(a), which can be easily understood by the definition of Ca.

Although the relation between pressure and velocity is nonlinear and complicated, it is known from figures 2.4 and 2.6 that the velocity evolution is affected by the plug length and the channel width when L_0, w_0 and P_{dr} are fixed. Since the plug length is related to the network topology
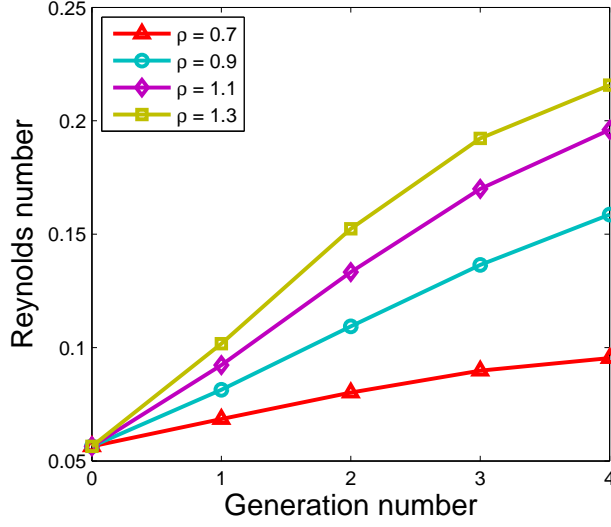
Figure 2.7: Reynolds number variation of the flow with $L_0 = 2$ mm and $P_{dr} = 250$ Pa.

within the assumption we made, the velocity evolution, in fact the global behavior of the flow, is determined by the geometry ratio ρ.

It is noted that the flow is within the region where gravity can be neglected since the length-scale is below 2 mm, the capillary length. The variation of Reynolds number is plotted in figure 2.7, in which calculation U represents the plug velocity and the characteristic length is taken as the channel height h while other related parameters can also be found in table 2.1. The Reynolds number is very small here, ranging from 0.05 to 0.25, which indicates the flow is much more viscous than inertial.

With all the above results, we start to know the global behavior in the network. Compared to the velocity of a single daughter, the total flow rate, the variable related to the motion of all the daughters in the network, is more concerned in the study about network dynamics. The network can be separated to several paths, each of which connects the network entrance and one exit. The flow rate in every path is obtained from the product of plug velocity in that path U_k and the cross-sectional area of the channel where the plug moves $(hw)_k$, where k denotes the numbering of the path. By adding the flow rate in all the paths, the total flow rate is known as a function of the generation number and the width ratio of the network, as shown in figure 2.8. The sum of the flow rates in all the paths is found to increase. When $0.5 < \rho < 1$, the plug velocity increases while the channel width decreases in the later generations. The increase of total flow rate at $\rho = 0.7$ and 0.9 implies that the increases of plug velocity (nonlinear with the generation number i) and the number of branches (exponential with i) are more rapid than the decrease of the channel width (linear with i). Recalling that the plug velocity increases when
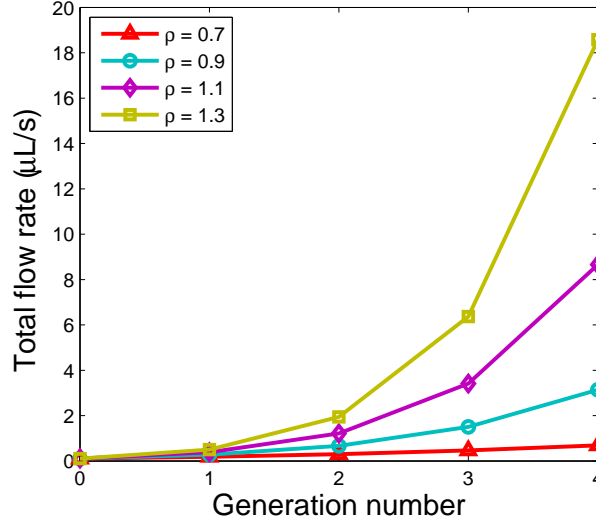
Figure 2.8: Variation of the total flow rate in the network with ρ varying from 0.7 to 1.3. The total flow rate increases with the generation number.

$\rho > 1$ in figure 2.6(a), the widening of channels leads to a straightforward increase of total flow rate as the plug advances, which is confirmed in figure 2.8.

2.2.3 Pressure evolution under constant flow rate

In this section, the flow is pushed at a constant flow rate instead of a constant pressure. Similar to the previous case, the plug is assumed to divide equally at the bifurcations. The difficulty comes when considering the symmetry of the flow. There may be different distributions of flow rate among different branches in the network as long as the total flow rate is conserved. The flow is not forced to develop symmetrically in the network. We thus assume two types of flow patterns here: a symmetrical development of the flow, which means that all the daughters move together in branches of the same generation, and an asymmetrical flow where only one daughter divides at one level of bifurcation leaving others stuck there.

When the flow develops symmetrically, the velocity of daughter plug varies with the generation number due to the conservation of total flow rate as well as the variation of channel geometry and the number of branches. This can be expressed by $Q_{\mathrm{dr}} = U_i s_i N_i$ where U_i is the daughter velocity, s_i is the cross-sectional area of the channel, N_i is the number of branches and i denotes the generation number. s_i is given as hw_i and $N_i = 2^i$. Then U_i can be calculated in different generations of different networks and plotted in figure 2.9 for $L_0 = 2$ mm and the driving flow rate $Q_{\mathrm{dr}} = 2$ μL/min. The same variables as in table 2.1 are used except the driving pressure. The velocity decreases with the generation number because of the exponential increase of the

Figure 2.9: Symmetrical flow with all the daughters moving, $L_0 = 2$ mm and $Q_{dr} = 2$ μL/min. (a)Plug velocities and (b) Capillary numbers in different generations of different networks with ρ changing from 0.7 to 1.3.

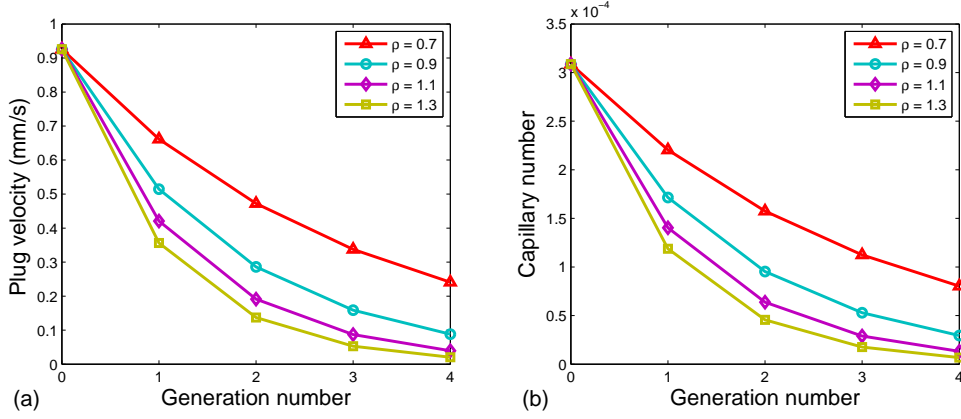branches, the number of moving plugs, in the later generations and the flow is within small capillary number regime (see figure 2.9(b)).

As the flow will possibly not develop symmetrically, another case is also discussed here. This time when the plugs arrive at the same level of bifurcation, only one of them passes, which leads to two new daughters moving in the next generation while others staying at the bifurcation they enter. There are always two daughter plugs flowing in the network beyond generation 0. The velocity is higher than in the symmetrical case as a result of reducing the number of moving plugs, as shown in figure 2.10(a). A turning point appears at generation 1 in all the four curves, where the initial plug divides into two daughters. After that, the number of moving plugs does not change and smooth curves are observed. The plug accelerates in the later generations when ρ is smaller than 1. This can be explained by the deduction of the asymmetrical assumption $Q_{dr} = 2s_i U_i$ which is $U_{i+1} = Q_{dr}/2s_{i+1} = Q_{dr}/2\rho s_i = U_i/\rho$. When $\rho < 1$, $U_{i+1} > U_i$, the plug accelerates. Otherwise $\rho > 1 \Rightarrow U_{i+1} < U_i$, and the plug velocity decreases.

Equation (2.4) can be used for calculating the viscocapillary pressure that pushes the plug since the velocity is known. In the case of constant flow rate driving, the pressure difference across the plug, the difference between the network inlet and exits, varies to preserve the plug velocity and thus conserve the total flow rate in the network. The pressure, as shown in figure 2.11, varies in a similar way with the velocity. Meanwhile, the Reynolds number also has the same pattern of variation with the plug velocity and pressure difference, as shown in figure 2.12.

2.2.4 Applications

With all the calculations in the previous two subsections, we have basic understandings of the flow evolution in the network. In the region of interest, the flow evolves within the regime of small
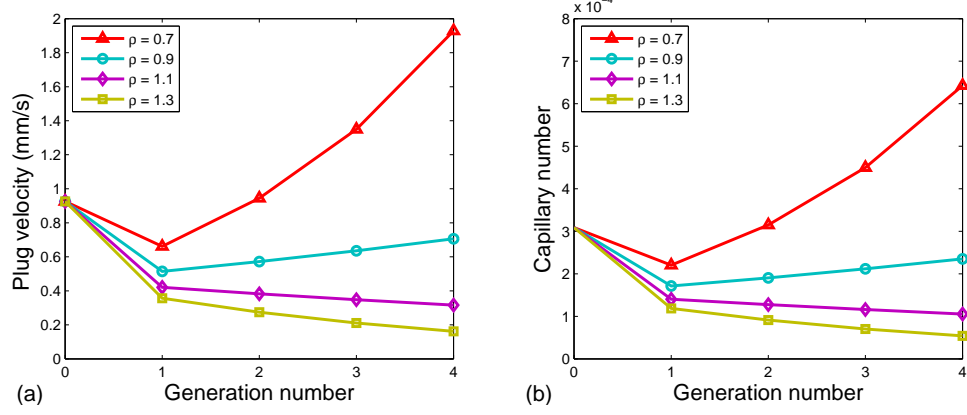
Figure 2.10: Asymmetrical flow with only two daughters moving after generation 0, $L_0 = 2$ mm and $Q_{\mathrm{dr}} = 2$ μL/min. (a)Plug velocities and (b) Capillary numbers in different generations of different networks with ρ changing from 0.7 to 1.3. The turning point at generation 1 is brought by doubling the plug number after the division of the initial plug.
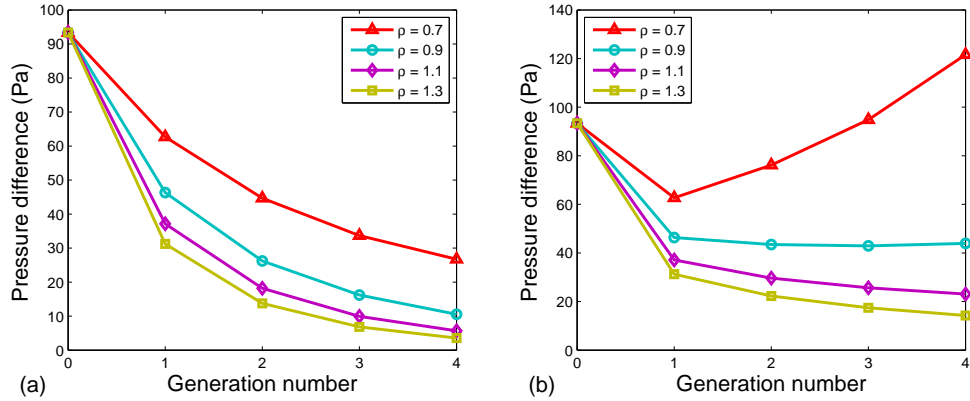
Figure 2.11: Pressure difference across the plug, between the network inlet and exits, varies as a function of the generation number and network geometry ($\rho = 0.7 - 1.3$). (a) The flow is symmetrical. (b) Only two daughters move after generation 0.
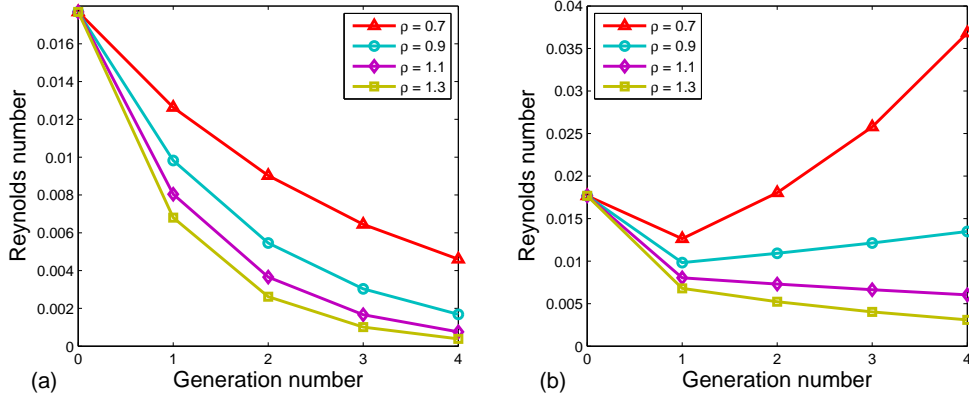
Figure 2.12: Reynolds number of the plug pushed at a constant flow rate in the network. (a) In the symmetrical flow, the Reynolds number decreases as the generation number increases. (b)In the asymmetrical flow, a turning point is observed at generation 1 and after that the Reynolds number increases with the generation number when $\rho < 1$.

Bond number (Bo $<< 1$), Reynolds number (figures 2.7 and 2.12) and Capillary number (figures 2.6(b), 2.9(b) and 2.10(b)). This makes microfluidics a suitable method in the experimental investigation.

As the primary motivation, we would like to study the plug transport in the pulmonary airway, where the mean diameters d of successive branches can be described as a function of the generation number i: $d_i = 2^{-1/3}d_{i-1}$ (Weibel, 1984). Supposing one section of the airway has the diameter 720 μm in the initial generation, the branch sizes in later generations can be known if we assume every branch in the binary airway is axisymmetric. This size variation is shown by the dash-dotted line in figure 2.13(a). Meanwhile, in networks of rectangular channels with our recursive rules, the sizes of branches vary with i and ρ. Given the width of the first generation to be 720 μm, the sizes of the branches in the network with different ρ are plotted by different symbols and compared to the airway. The dash-dotted line, corresponding to an equivalent ratio of 0.8, exists between those for networks with $\rho = 0.7$ and 0.9.

Since the flow behavior may be different depending on whether ρ is smaller or bigger than 1, see figure 2.10, two networks are studied in the following. One of them has a recursive ratio $\rho = 0.83$ to represent the variation of branch sizes in the airway, although our network is rectangular and the airway branch has circular cross-section. The channel length decreases with the generation number at the proportional constant ρ', which is chosen to preserve the ratio of plug length to channel length in each generation $L_i/L_{\text{channel},i}$, when the plugs divide symmetrically at the bifurcations. Since $L_i = L_0/(2\rho)^i$, $L_{\text{channel},i} = L_{\text{channel},0}/(2\rho)^i$ and thus $\rho' = 1/(2\rho) = 0.6$. The other network has widening channels with $\rho = 1/0.83 = 1.2 > 1$.
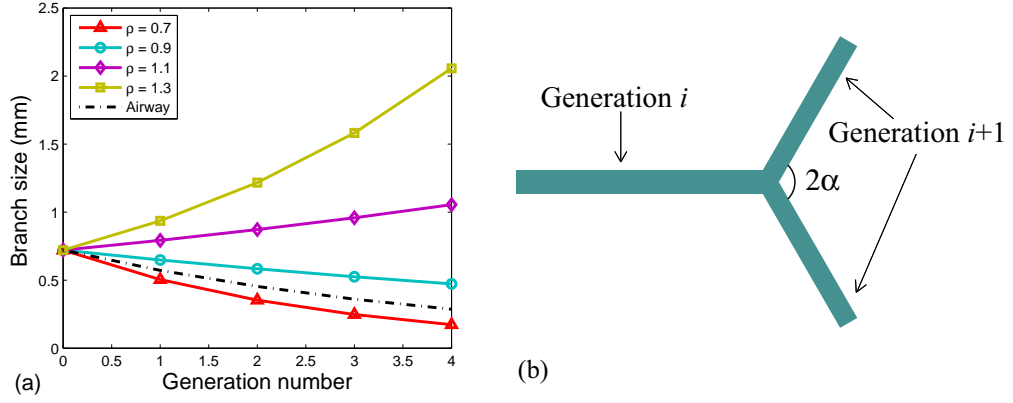
Figure 2.13: Criteria to choose the geometry ratio ρ and α in our network. (a) Comparison of the branch sizes in four networks to the airway. (b) The basic unit of three branches illustrating the bifurcation half-angle α

The bifurcation half-angle α is $60°$, which yields the same angle between any two of the three branches in the basic unit of the network shown in figure 2.13(b). In this way, all the branches are well separated from each other and the daughter branches can both be lengthened to the same extent without intersecting branches in other generations. This is particularly helpful when there are many generations, since the network with $\alpha = 60°$ achieves the optimal filling of space under our recursive rules.

2.3 Passage through a bifurcation

When the plug passes a bifurcation, its interfaces have to deform due to the geometry change in the bifurcation. These interface deformations can introduce a capillary pressure difference across the plug, since the radii of curvature at two interfaces are no longer the same. In this section, we begin by considering the details of the passage of a plug through a bifurcation, then define a threshold pressure associated with the bifurcation and in the end discuss how this pressure variation may influence the flow in our network.

2.3.1 Position-dependent capillary pressure difference

There are different stages during the passage through a bifurcation depending on the plug position in the bifurcation. The plug becomes affected by the bifurcation at the position shown in figure 2.14(a), where the front interface reaches the branching corner and its curvature starts to decrease until it touches the opposite tip, 2.14(b). After the touching, the front interface enters the next generation and the curvature increases very quickly as shown in figure 2.14(c). We here assume that the plug is long enough so that the rear interface remains in the straight channel before the front one touches the next generation, and that the rear interface advances very quickly

Figure 2.14: Different stages during the plug passage through a bifurcation. The front interface reaches the bifurcation corner (a), touches the opposite wall (b) and enters the next generation (c). (d) The entire plug passes the bifurcation and divides into two daughters.

through the bifurcation to the next generation due to the capillary pressure difference explained below. Therefore, the stage of two daughters in the next generation comes after 2.14(c).
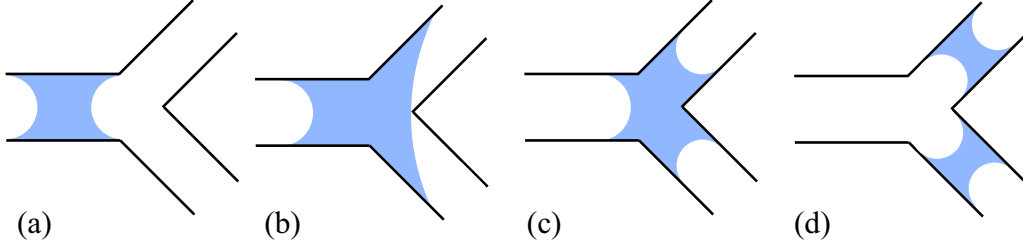
The interface deformations imply position-dependent capillary pressure variation. At a given plug position, there exists a capillary pressure difference, cross the plug, which may resist the driving force. This is a three-dimensional problem and the largest curvature of the interface exists in the direction perpendicular to the plane of the network, which does not change since the height of the channels is constant. Accordingly, the capillary pressure *difference* is mainly driven by curvature differences in the plane of the network. Therefore this difference P_{cap} between the rear and front interfaces can be expressed as:

$$P_{\mathrm{cap}} = P_{\mathrm{r}} - P_{\mathrm{a}} = \gamma/r_{\mathrm{r}} - \gamma/r_{\mathrm{a}}, \qquad (2.5)$$

where $P_{\mathrm{r}}, P_{\mathrm{a}}$ denote the capillary pressures at the receding and advancing (rear and front) interfaces and $r_{\mathrm{r}}, r_{\mathrm{a}}$ are the signed radii of curvature of the interfaces in the plane of the network. $r_{\mathrm{r}}, r_{\mathrm{a}}$ depend on the liquid contact angle θ on the wall and the bifurcation half-angle α. The determination of P_{cap} with respect to plug positions during the passage is provided in Appendix A.

For a plug passing a bifurcation, the curvature of the front interface decreases before the rear one is affected by the bifurcation, as sketched in figure 2.15(a). We have $|r_{\mathrm{a}}| > |r_{\mathrm{r}}|$ and $|r_{\mathrm{a}}|$ increases as the plug advances. So P_{cap} takes on increasing positive values until the front interface touches the opposite facing tip. Beyond this point, the plug starts to divide, as shown in figure 2.15(b), and P_{cap} decreases rapidly. At this stage, the sign of P_{cap} depends on whether $|r_{\mathrm{a}}|$ is smaller or larger than $|r_{\mathrm{r}}|$. In a network with narrowing channels $\rho < 1$, P_{cap} becomes negative ($|r_{\mathrm{a}}| < |r_{\mathrm{r}}|$) and pulls the daughter plug to pass through. Conversely, in a network with widening channels $\rho > 1$, the P_{cap} remains positive after the touching and still resists the plug
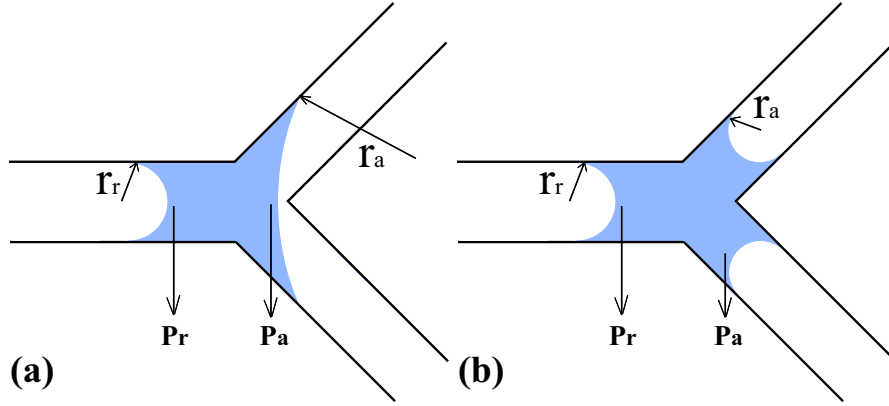
Figure 2.15: Passage through a bifurcation. (a) One plug arrives at the bifurcation. The radius of curvature $|r_a|$ is bigger than $|r_r|$ and increasing while the plug is advancing. (b) After the front interface touches the facing tip and enters the next generation, $|r_a|$ varies according to the channel width. (Notice that here $2\alpha = 90°$ for convenience.)
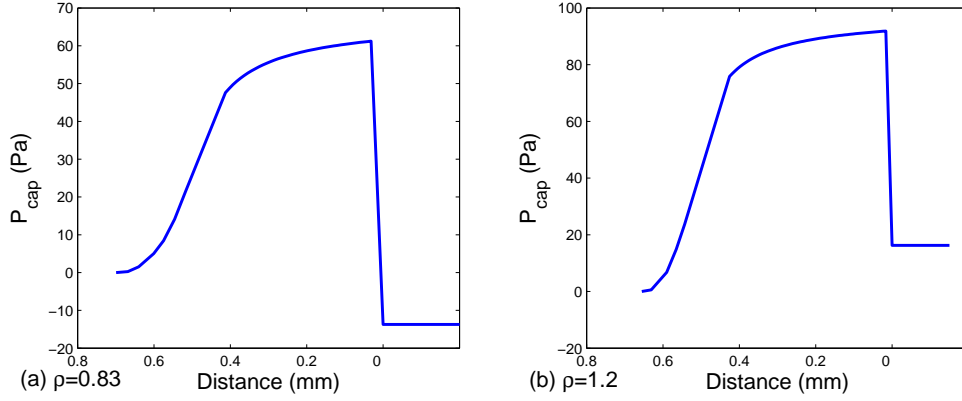
Figure 2.16: P_{cap} variation versus the distance of the front interface from the facing tip. (a) In the network with $\rho = 0.83$. (b) In the network with $\rho = 1.2$.

advancement. When the plug has fully passed the bifurcation (figure 2.14(d)), P_{cap} cancels, since $|r_a| \cong |r_r|$.

The variations of P_{cap} during the plug passage in our networks are plotted in figure 2.16. For the network with $\rho = 0.83$ and $w_0 = 720$ μm, the calculation is done by using (2.5) for a PFD plug (see Chapter 3 for physical properties) and taking the parameters of the second bifurcation, where the parent channel has a width $w_1 = 598$ μm and the daughter channels have $w_2 = 496$ μm. In the network with $\rho = 1.2$, w_0 equals 342 μm, which is the channel width in the last generation of the other network. Figure 2.16(b) also shows the pressure variation for a plug passes the second bifurcation.

P_{cap} begins to increase from 0, when both interfaces are in the straight channel and there is no capillary pressure difference. As the front interface advances in the bifurcation, P_{cap} increases
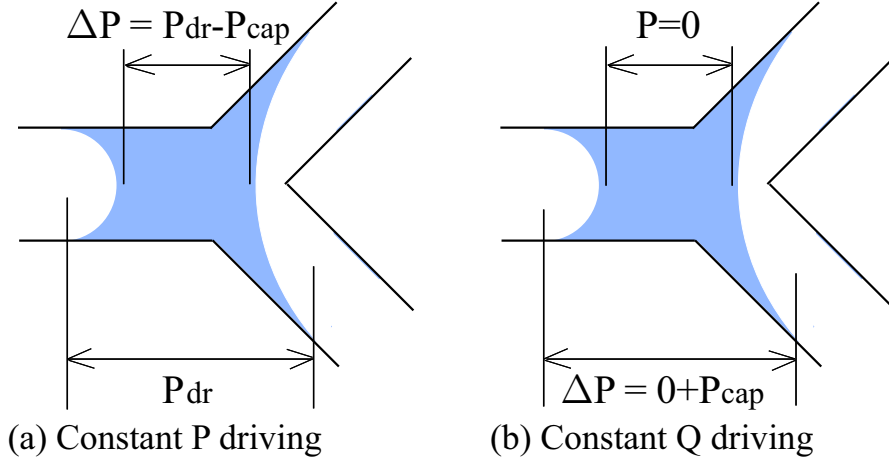
Figure 2.17: Pressure condition across the plug in a bifurcation. The noted pressure indicates the pressure difference between the two points. (a) Constant pressure driving. (b) Constant flow rate driving.

until it reaches a maximum value, when the front interface just touches the facing tip. After that, a rapid decrease of P_{cap} is observed and its value remains constant afterward. Similar curves are found in both networks although the sign of P_{cap} after the touching depends on the width of two successive channels.

The plug is always pushed by a driving force from the first generation to the last one. When it is pushed at a constant pressure P_{dr}, the pressure difference across the plug can be expressed as $\Delta P = P_{\mathrm{dr}} - P_{\mathrm{cap}}$, as illustrated in figure 2.17(a). The variation in P_{cap} will modify the value of effective driving pressure and thus lead to the variation of ΔP, which is given in figure 2.18 for the two networks when $P_{\mathrm{dr}} = 250$ Pa. Opposite to the variation of P_{cap}, ΔP decreases before later increasing as the plug advances in the bifurcation. ΔP must remain positive during the passage in order to push a plug through a bifurcation.

When the plug is forced at a constant flow rate, the passage is treated as a quasistatic process, which implies there is no pressure difference inside the plug, as shown in figure 2.17(b). In this case, P_{cap} will induce variations in the pressure upstream of the plug position since the downstream pressure is fixed to atmospheric pressure. The pressure difference across the plug, $\Delta P = 0 + P_{\mathrm{cap}}$, increases until the plug touches the opposite wall, where it decreases rapidly as shown in figure 2.19. However, the pressure condition after touching is not very clear in the flow rate driving case, since the plug is experiencing the switch between two types of motions, where the pressure differences are estimated differently.

Figure 2.18: ΔP variation versus the distance of the front interface from the facing tip under a constant pressure driving. The dotted line represents the driving pressure $P_{\mathrm{dr}} = 250$ Pa. (a) In the network with $\rho = 0.83$. (b) In the network with $\rho = 1.2$.

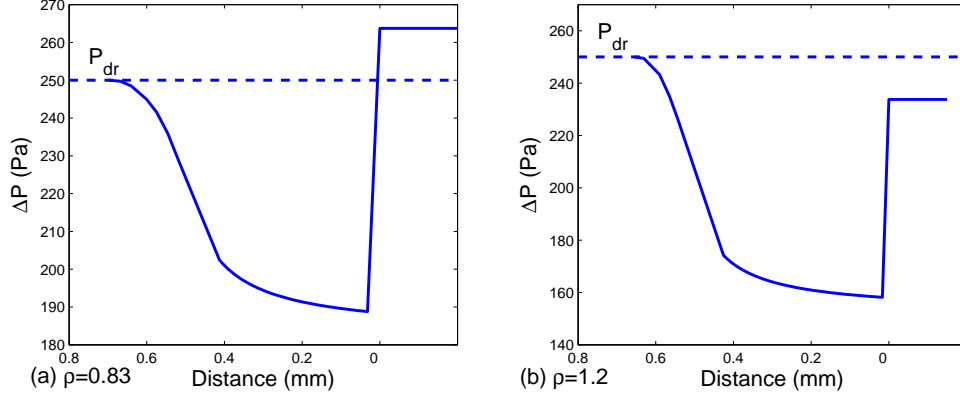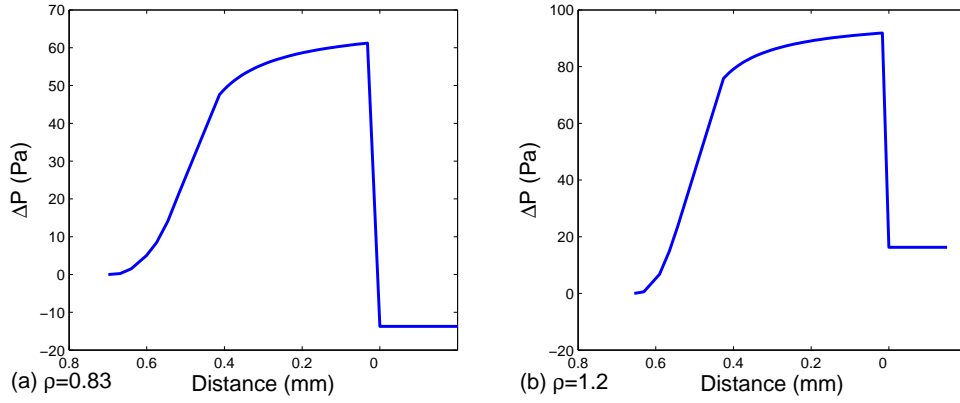Figure 2.19: ΔP variation versus the distance of the front interface from the facing tip under a constant flow rate driving. (a) In the network with $\rho = 0.83$. (b) In the network with $\rho = 1.2$.
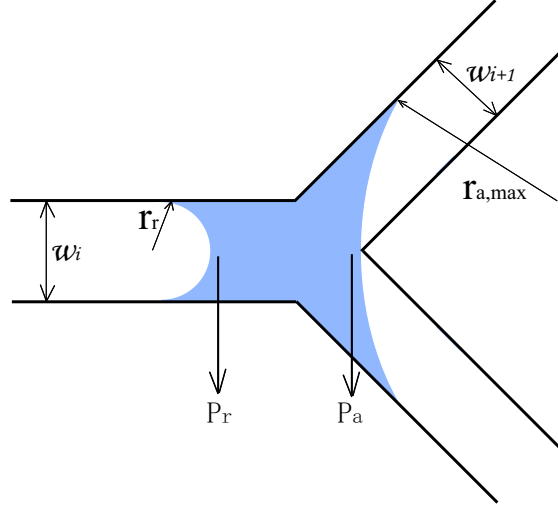
Figure 2.20: r_a and P_{cap} reach their maximum values when the front interface touches the facing tip. w_i and w_{i+1} are the channel widths in two successive generations.

2.3.2 Variation of threshold pressures in the network

There exists a maximum value of P_{cap} in the variation of capillary pressure difference both in figures 2.16(a) and (b). This maximum value is then defined as a threshold pressure P_{thr} associated with the bifurcation geometry and must be overcome for pushing a plug through a given bifurcation. P_{thr} can be estimated as: $P_{thr} = P_{cap,max} = \gamma/r_r - \gamma/r_{a,max}$ where $r_{a,max}$ is the maximum possible value of r_a. $r_{a,max}$ is reached just before the front interface touches the facing tip, as shown in figure 2.20, where w_i and w_{i+1} denote the channel widths in two successive generations. P_{thr} is computed from the network geometry as:

$$P_{thr} = \frac{2\gamma\cos\theta}{w_i} - \frac{\gamma(\cos\theta - \sin\alpha)}{w_{i+1}} \tag{2.6}$$

where θ is the static contact angle of the liquid (PFD) on the channel wall (PDMS) (around 23°) although variations in the contact angle is however observed in experiments when the plug is moving. For the same liquid (fixed γ and θ) and bifurcation geometry (fixed w_i and w_{i+1}), the threshold pressure is a function of the angle α and a bigger α results in a higher threshold in the bifurcation.

P_{thr} varies as $P_{thr,i+1} = (1/\rho)P_{thr,i}$, which is similar to the variation of w_i in the network. In a network with $\rho < 1$, which means $w_i > w_{i+1}$, $P_{thr,i+1} > P_{thr,i}$ indicates the threshold pressure increases with the generation number. Conversely, in the widening network where $\rho > 1$, P_{thr} decreases when the generation number increases. The threshold pressures in our two networks are plotted in figures 2.21. P_{thr} increases from 51 Pa at the first bifurcation in the narrowing network with w_0=720 μm and $\rho = 0.83$. At the ninth bifurcation P_{thr} goes up to 227 Pa, which
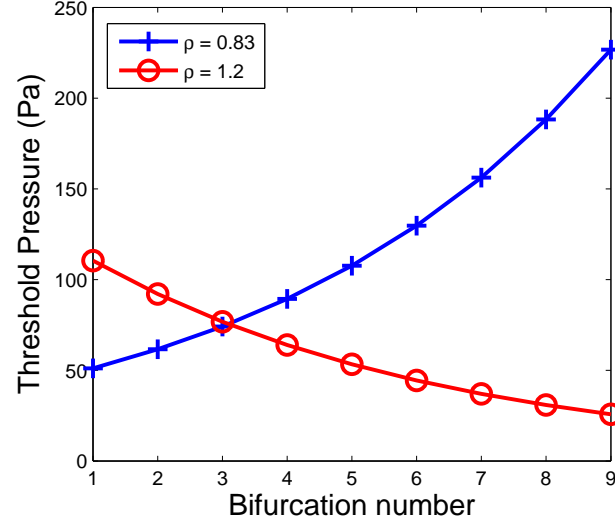
Figure 2.21: Threshold pressure variations in both narrowing and widening networks of 10 generations. The narrowing network has w_0=720 μm and $\rho = 0.83$ while the widening network with w_0=342 μm and $\rho = 1.2$.

quadruples the value at the first bifurcation. In the widening network, the threshold decreases slowly from 110 Pa at the first bifurcation to 26 Pa at the ninth bifurcation.

Chapter 3

Experimental setups

3.1 Network concerned

3.1.1 Microfabrication

Soft lithography techniques, which are widely used in micro- and nano-fabrication (Quake & Scherer, 2000), are employed to make the network of branching microchannels with the usage of dry film photoresist (Stephan *et al.*, 2007). There are three steps in the fabrication: drawing the mask, creating the master and replicating the micro structures, all of which are illustrated in figure 3.1.

First of all, the geometry of the microchannels is designed with the help of the computer software Adobe Illustrator and printed on a transparency with high resolution. This transparency as shown in figure 3.1(a) is called the mask, here for a network with narrowing channels.

Secondly, in order to create a master, a layer of photoresist, a dry film photopolymer (Etertec XP-800), is deposited on the glass slide, as shown in 3.1(b), where the height of the photoresist is noted as h. The mask obtained previously is now put on top of the photoresist and the whole package is exposed to UV light source for 5 minutes. In this way, the black portion in the mask protects the photoresist underneath from exposure while the rest is patterned through chemical reactions. The patterned photoresist is then developed by immersing it in an aqueous solution of potassium carbonate (K_2CO_3) at a concentration of 1% by weight. The developing process takes around 10 minutes, after which the etched photoresist becomes a master that can be used to replicate micro structures, as shown in 3.1(c).

In the last step, the liquid prepolymer of polydimethylsiloxane (PDMS) is poured onto the master and cured for a few hours, 3.1(d). Once PMDS switches to solid state, the block can be peeled off the master and microchannels are cast on the surface with the depth of h, 3.1(e). The micro structures are successfully fabricated through soft lithography and the remaining work is to bond them on a substrate. The prepolymer of PDMS is spread all over a glass slide in a spin
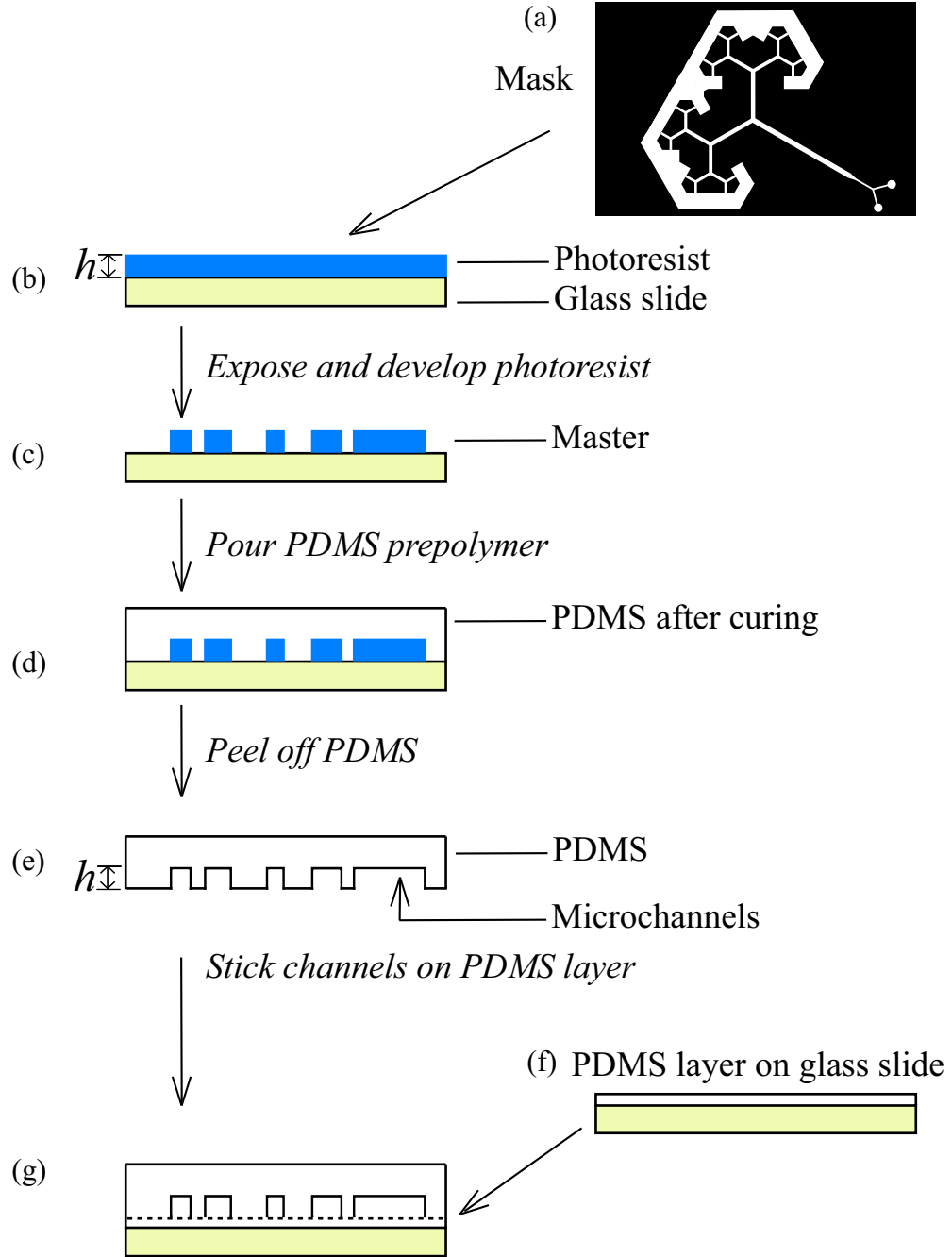
Figure 3.1: Procedure of microfabrication. (a) Mask to be printed on a transparency. (b) and (c) Creation of the master. (d) and (e) Replication of microchannels on PDMS. (f) and (g) Sticking microchannels on a substrate.
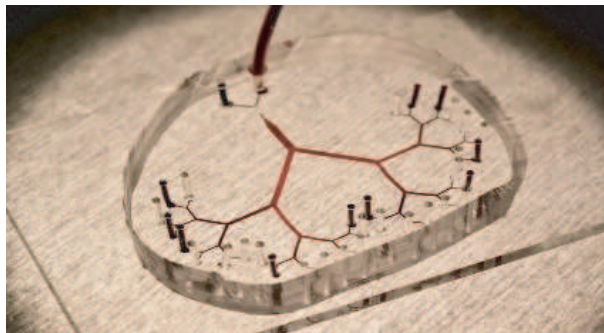
Figure 3.2: Image of a real network of branching channels. Red ink is injected through one inlet so that the whole network can be seen.

coater. After curing, a film of PDMS is deposited on the slide, 3.1(f). Finally, the microchannels are bonded to the substrate with PDMS film through oxygen plasma treatment (Bhattacharya *et al.*, 2005; Eddings *et al.*, 2008), to guarantee identical boundary conditions at all the channel walls, as shown in figure 3.1(g), where the channels are found between PDMS block and the substrate separated by the dotted line while other portion of the two is stuck together.

One example of the network of branching microchannels is shown in figure 3.2, where holes are punched through the PDMS block at the entrance and exits. One tube is plunged into the entrance hole to flow red ink into the network, which provides good visualization. In experiments, tubes are plunged at the entrance holes, through which fluid flows into the network. The holes at the exits are open to let fluid go out.

3.1.2 Network geometry

Top views of our networks through a microscope are given in figure 3.3, where there are five generations of branching channels and four levels of bifurcations in both. Generation numbers are labeled with Arabic numerals while Roman numerals are used for bifurcations. The height (in the direction perpendicular to the image of figure 3.3) of all the branches in the network is $50\,\mu$m, which equals the thickness h of the photoresist used in the microfabrication. The channel width w_i changes at the constant ratio ρ. At the end of the last generation, sixteen exit holes (black in figure 3.3) are punched to fix the exit condition at atmospheric pressure P_{atm}.

Two networks, with $\rho = 0.83$ (figure 3.3(a), referred to later as the $\mathcal{N}$ network) and $\rho = 1.2$ (figure 3.3(b), the $\mathcal{W}$ network) are fabricated. In both of them, the channel width varies between $342\,\mu$m and $720\,\mu$m. This gives a width of the first generation to be $720\,\mu$m and the last generation to be $342\,\mu$m in the $\mathcal{N}$ network. Conversely, in the $\mathcal{W}$ network, the first generation has a width of $342\,\mu$m and the last generation is $720\,\mu$m wide.
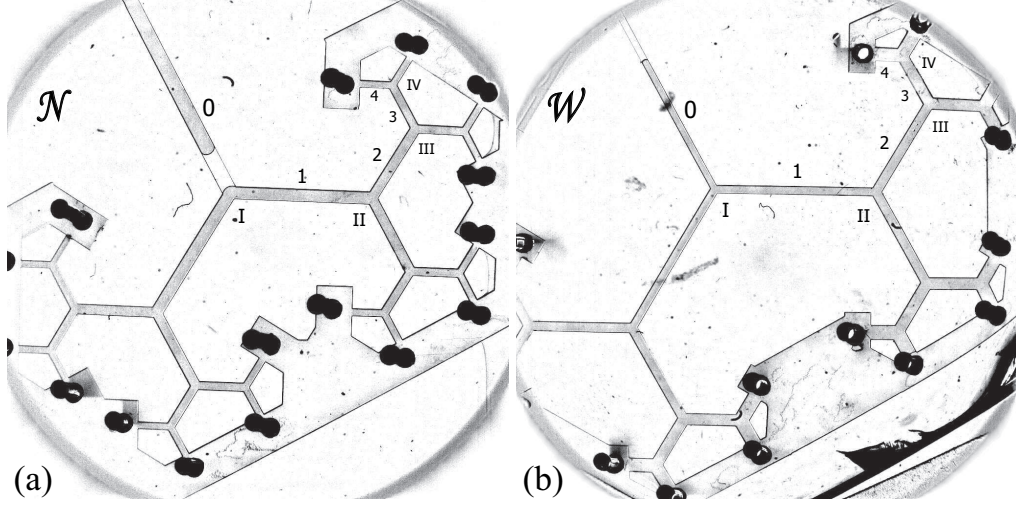
Figure 3.3: Microscope images of the microfluidic networks with five generations. Generation numbers are labeled with Arabic numerals while Roman numerals are used for bifurcations. Sixteen holes are made at the exits to fix the boundary condition at atmospheric pressure. (a) $\mathcal{N}$ network and (b) $\mathcal{W}$ network.

3.2   Setups

The network inlet consists of a Y-junction connected to the first generation for creating and injecting liquid plugs (Ody, 2007). A picture of the Y-junction is shown in figure 3.4, where the liquid plug is represented by bright column surrounded by gray which corresponds to the air. One inlet of the Y-junction provides the passage for the liquid perfluorodecalin (PFD) entering the network. PFD is a fluorocarbon whose viscosity and surface tension are $\eta = 5 \times 10^{-3}$ Pa s and $\gamma = 20 \times 10^{-3}$ N/m, respectively. It has good wetting properties on PDMS and does not swell the channels (Lee *et al.*, 2003). Through the second inlet of the Y-junction, the air goes into the network and a driving force is applied between the first and the last generations.

A sketch of the experimental setup is shown in figure 3.5. The liquid inlet of the network is connected to a syringe which is filled with PFD and can be pushed by a pump, so that the liquid can enter the network. Through the air inlet, either constant pressure P or constant flow rate Q can be applied. When providing a constant pressure, the air inlet is connected to a computer-controlled (Computer 2) pressure source (FLUIGENT, MFCS-8C) by a flexible microtube. The precision of the pressure source is experimentally testified since the output value can be measured and recorded by FLUIGENT during operation. For the input values of $P = 200$ Pa and $P = 900$ Pa, the output pressure is plotted in figure 3.6, when there is a constant resistance between the network entrance and exits. Pressure values are chosen here to cover the need in the experiments and the machine gives satisfactory control of pressure at the given parameters.
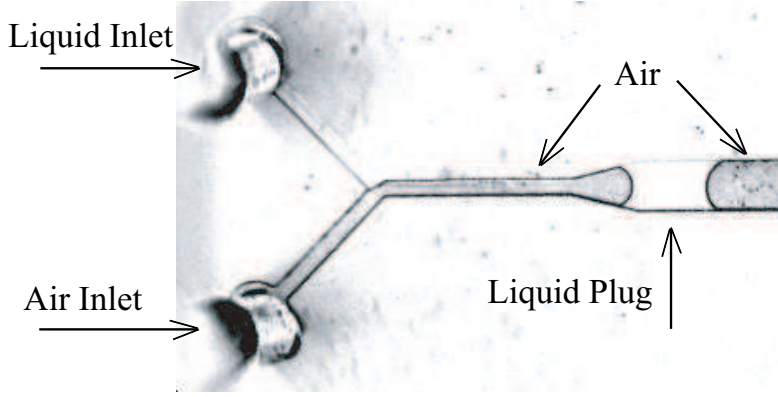
Figure 3.4: Y-junction in the inlets of the network. A liquid plug of PFD (bright part) surrounded by air (gray part) is created and ready to be pushed into the first generation of the network.

For flow rate driving, the syringe for air is connected to the inlet by a microtube and pushed by a pump, which ensures a constant flow rate. Supposing the air cannot be compressed, the total flow rate in the network does not change during the experimental process. However, the air pressure has to vary in order to keep the flow rate constant and this makes the air compressed (or expanded), which results in asynchrony between the pump pushing and the plug moving. The asynchrony become visible when a pressure variation is required to resume the flow, e.g. during the passage of a bifurcation. In this case, a rapid change of pressure is desired to improve the pushing condition and better provide the constant flow rate. More discussion about this can be found in Appendix B.

In the setup, the syringe contains 50 μL of air and the microtube is 20 cm long (PTFE Tube 0.56 $\times$ 1.07 mm). The volume of the $\mathcal{N}$ network is $V_N = 2.2$ μL, so the air inside the syringe and the tube is 50 times of V_N. The air pushing the plug needs a long time, compared to the time of a single experimental run, to be compressed when the pressure increases. For this reason, the syringe and the microtube are filled with water and only 1 cm of air near the network entrance is left in the tube. The syringe pump pushes the water which then pushes the air into the network. The air between the water and PFD plug has the same volume as the network and its compression time is reduced by up to 98% in this way. .

The improvement is demonstrated by the experimental measurements shown in figure 3.7, where evolutions of total flow rate in the network are compared when the driving flow rate 4 μL/min is applied by two different configurations. When a single plug is injected into the $\mathcal{N}$ network and pushed through successive generations, the flow rate in each branch is obtained from the plug motion and the total flow rate is calculated by summing up those in each branch. The measurements of plug motion will be discussed in detail in the next section. When the syringe and the connecting tube are filled with air, big fluctuations in flow rate is found in figure 3.7(a).
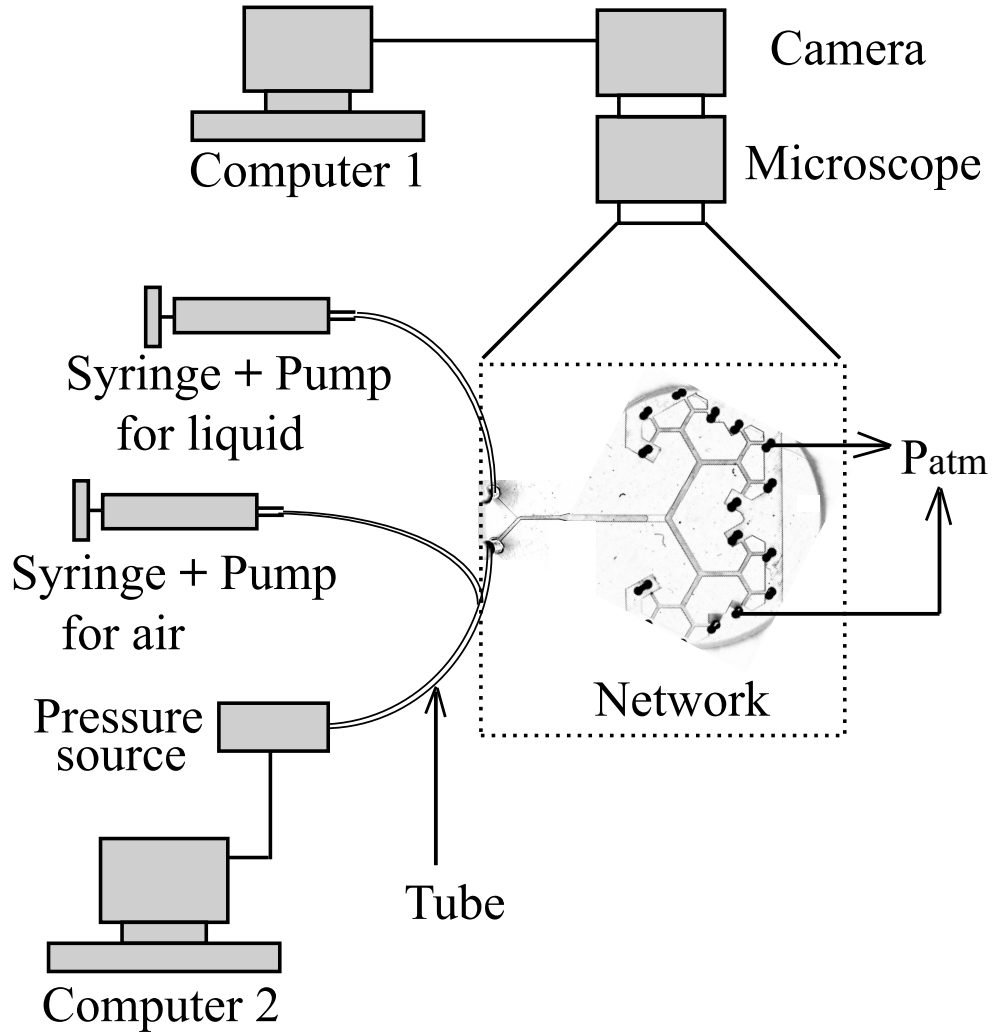
Figure 3.5: Experimental setup for the investigation about transport of liquid plug in the network. A syringe is filled with liquid and connected to one inlet of the network. The syringe can be pushed by a pump so that the liquid inside goes into the network. The other inlet of the network is connected either to a pressure source controlled by computer 2 or to a syringe through a microtube, in the way that constant pressure or flow rate driving can be realized respectively. The flow in the network is recorded with a high speed camera through a microscope and the acquired image sequences are stored in computer 1.
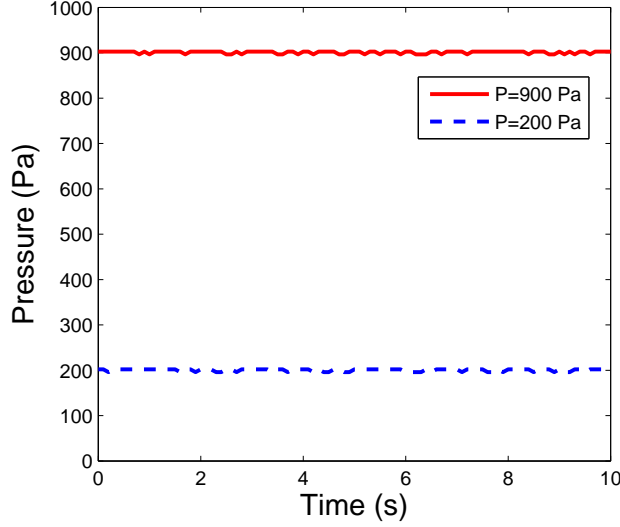
Figure 3.6: The pressure output of the computer-controlled pressure source when the inputs are $P = 200$ Pa (Dashed line) and $P = 900$ Pa (Solid line) with a duration of $t = 10$ s when stationary resistance exists between the network entrance and exits. Satisfactory constancy of pressure is observed.

There is little flow between $t = 8$ and $t = 11$ during which the air is being compressed instead of pushing the plug forward. In the other case, when the syringe and connecting tube are filled with water, the control over flow rate is much improved as shown in figure 3.7(b). The plotted flow rate however varies in the latter case due to difficulties in measuring and calculating the flow rate in bifurcation areas.

Experiments are recorded with a high speed camera (Photron Fastcam, 1024 PCI) through a stereomicroscope (Leica, MZ 16) at 0.7× magnification. The resolution of the camera is 1024×1024 pixels, which yields 1 pixel for 24.8 μm. For the single plug experiments, images are taken at a rate of 60 frames per second for the constant pressure driving. For the flow rate driving, the frame rate varies from 30 to 500 images per second and the specific choice is taken in order to have image sequence of the flow at a satisfactory resolution. For two or three successive plugs under constant pressure driving, 125 images per second are recorded. The frame rates for different experiments are summarized in table 3.1 for reference. The image sequences are stored in Computer 1 and analyzed afterward.

3.3 Preliminary studies

3.3.1 Measurements

The positions of the front and the rear interfaces of the plug and its daughters, x_a and x_r, can be manually recorded from the image sequence obtained while the plug is traveling in the straight
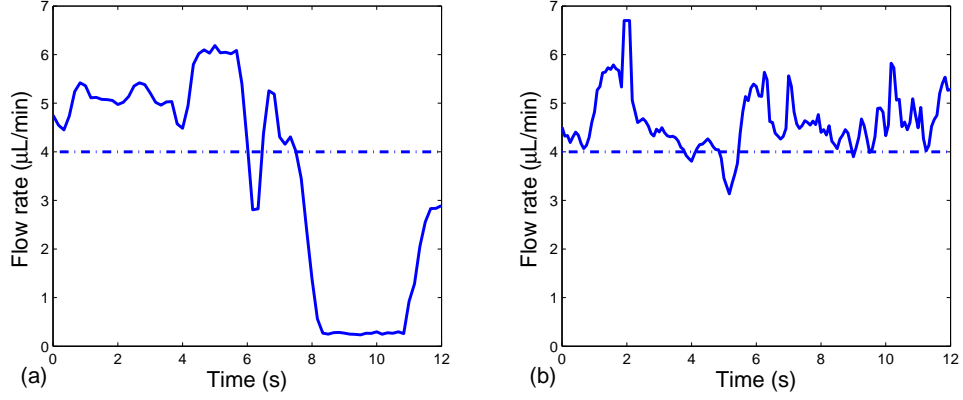
Figure 3.7: Total flow rate variation in the network under two configurations for flow rate driving. A single plug is pushed through successive generations and the flow rate in each branch is obtained by measuring the variation of plug position versus time. The total flow rate is plotted by summing up the flow rate in each branch. For both cases, the input value of flow rate, indicated by the dash-dotted line, is 4 μL/min and ensured by the pump. (a) The air fills the syringe and the connecting tube to the inlet. (b) The connecting tube is filled with water and only 1 cm of air near the network entrance is left in the tube.

Table 3.1: Frame rates taken when recording the experiments.

Number of plugs	Network	Driving Condition	P or Q	Frame Rate (images/sec)
1	$\mathcal{N}$	Pressure	$P = 250$ Pa	60
1	$\mathcal{N}$	Flow rate	$Q = 2\ \mu$L/min	30
1	$\mathcal{N}$	Flow rate	$Q = 5\ \mu$L/min	60
1	$\mathcal{N}$	Flow rate	$Q = 20\ \mu$L/min	250
1	$\mathcal{W}$	Flow rate	$Q = 2\ \mu$L/min	30
1	$\mathcal{W}$	Flow rate	$Q = 4\ \mu$L/min	30
1	$\mathcal{W}$	Flow rate	$Q = 20\ \mu$L/min	500
2 or 3	$\mathcal{N}$	Pressure	$P = 500$ Pa	125
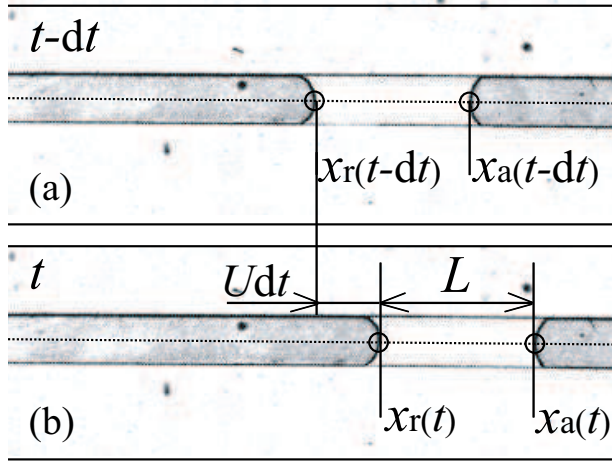
Figure 3.8: Measurement of the interface positions in the straight channel. The dotted line shows the center of the channel and the position vector x is the coordinate of the point where the interface intersects the dotted line. x_a and x_r are recorded at every time step with a interval dt so that the plug length L and velocity U can be calculated as illustrated.

channel. The interface positions are measured at the center of the channel width, as shown in figure 3.8. x is the coordinate of the point, marked by the circle, where the liquid interface intersects the central line of the channel (the dotted line). The length of the plug can be thus known as: $L = |x_a(t) - x_r(t)|$. More importantly, by tracking the position of the rear interface, the velocity of the plug U can be calculated as: $U = [x_r(t) - x_r(t - dt)]/dt$, where dt is the time step between two images. Therefore, the flow rate in this branch can be known from the relation $Q = Uwh$, where w is the width of the channel.

Since the bifurcation connects straight channels in the network, the axes of these three channels intersect at one point T, as shown in figure 3.9. When a plug passes a bifurcation, the position of the rear interface is measured in the previous generation (the horizontal channel in the figure) before it passes point T, see figure 3.9(a). After the interface passes point T, the position is measured in the daughter branch of the next generation, figures 3.9(b) and (c). In this way, the interface position is continuously recorded and the main characters of the passage can be captured. The switch of generation in measurements may introduce less precise tracking of the interface at the bifurcation but the error is tolerated, since the focus is on the global behavior of the flow rather than the detailed evolution at the bifurcation.

Combining figures 3.8 and 3.9, the motion of the daughter plugs can be tracked along different branches. Four paths, as labeled in figure 3.10, for the $\mathcal{N}$ and $\mathcal{W}$ networks are selected for experimental measurements. The distance, from the network entrance, traveled by the daughter along one path is calculated as $Dis = \sum[x_r(t) - x_r(t - dt)]$. The last generation is not tracked because it is close to the network exits and the flow there is affected by the boundary conditions.
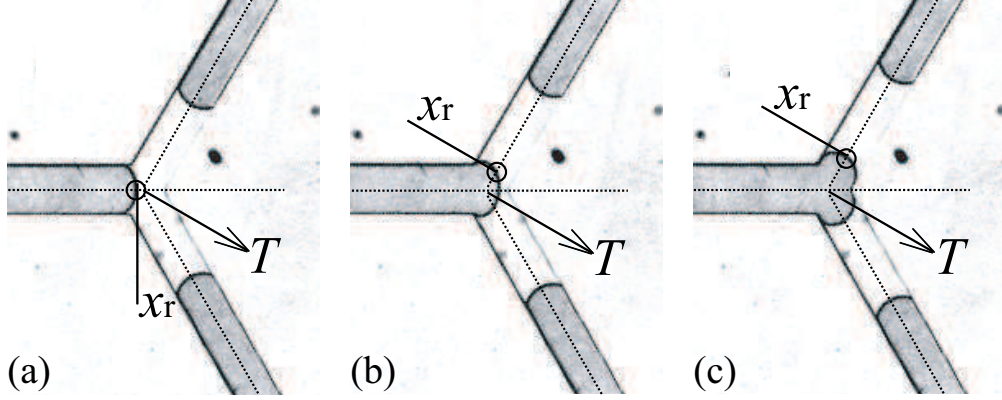
Figure 3.9: Interface tracking at the bifurcation. The axes of three connected channels intersect at point T. Before passing point T, the interface position is measured in the horizontal channel (a) and after that, the positions are recorded in the branched channel (b) (c).
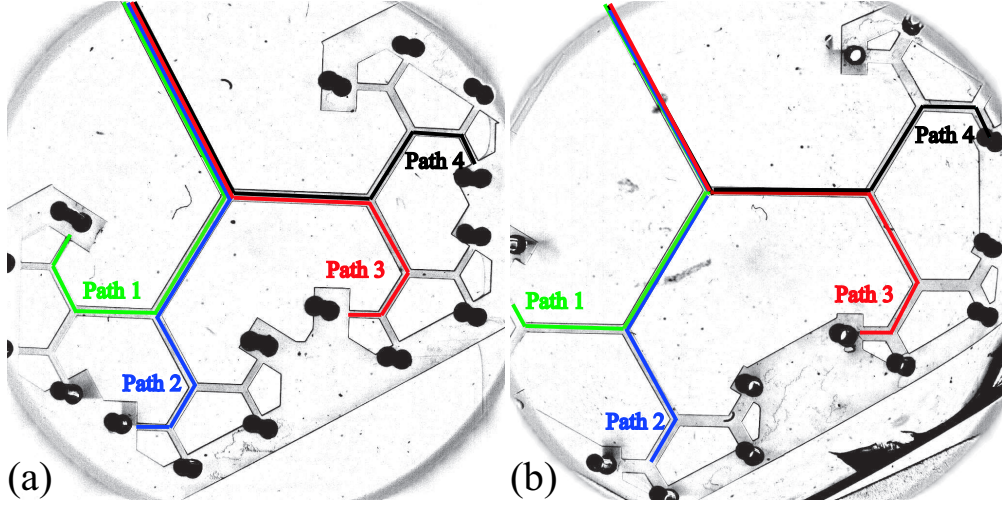
Figure 3.10: Paths along which plug positions are measured in the $\mathcal{N}$ (a) and $\mathcal{W}$ (b) networks.

The motion of daughters in these four representative paths provides a good global description of the flow, since two daughters of one origin move symmetrically at least until one of them divides at the next bifurcation; see experimental results in Chapter 4.

3.3.2   Interface tracking

The position of the plug is tracked as the position of its rear interface. For a plug pushed at $P = 250$ Pa, a sequence of images are obtained and shown in figure 3.11. The vertical dashed line marks out the position of the rear interface along the axis, which is normalized by the channel length. This yields a range of the normalized plug position Pos to be $0 < Pos < 1$. As the plug moves from left to right, its length L is recorded, as illustrated by the two sloping lines.
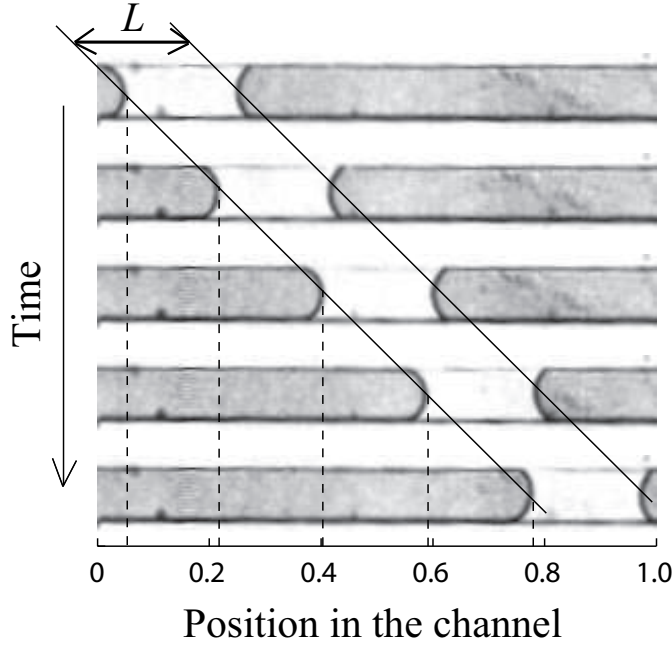
Figure 3.11: Image sequence tracking the normalized position of the plug in a straight channel. The dashed lines denote positions of the plug by its rear interface and the length of the plug L is recorded as time varies.

Variations of plug length versus the normalized position are plotted in figure 3.12 when the plug advances through generation 0 and one branch in generation 1 in the same experiment shown in figure 3.11. The plug length remains constant inside the generation and varies as $L_1 = (0.5/0.83)L_0$ between two generations, as expected theoretically.

When a plug passes a bifurcation, both interfaces are deformed due to geometry, as shown in figure 3.13 by the images from the same experiment as in figure 3.11. The front interface first enters the bifurcation and its curvature decreases until the interface touches the opposite wall, 3.13(c). After the splitting of the front interface in 3.13(d), the rear interface arrives at the bifurcation, deforms (3.13(d)) and reaches the next generation, when the plug passes completely as shown in figure 3.13(f).

During the passage, the plug length varies with its position since the cross-sectional area is no longer constant as in the straight channels. Moreover, the shape of the plug can be complex, for example in figures 3.13(d) and (e), which makes it difficult to measure or calculate the length. However, the measurement of the plug position reveals the flow evolution and can be performed as illustrated in figure 3.9. The dashed lines locate the measurements in the horizontal channel in figures 3.13(a)-(e) but the measurement that should be done in the branched channel is not located in figure 3.13(f).
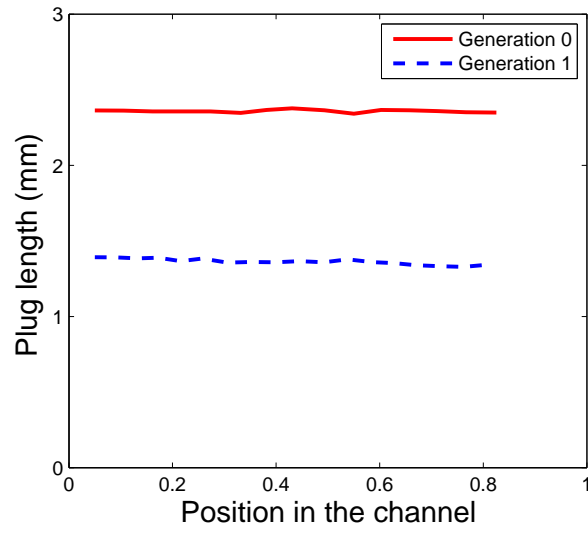
Figure 3.12: Plug length versus its position in the straight channel at driving pressure $P = 250\,\text{Pa}$. The lengths of one plug and its daughter are recorded in generations 0 and 1. The position of the plug is measured along the channel direction and normalized by the channel length.
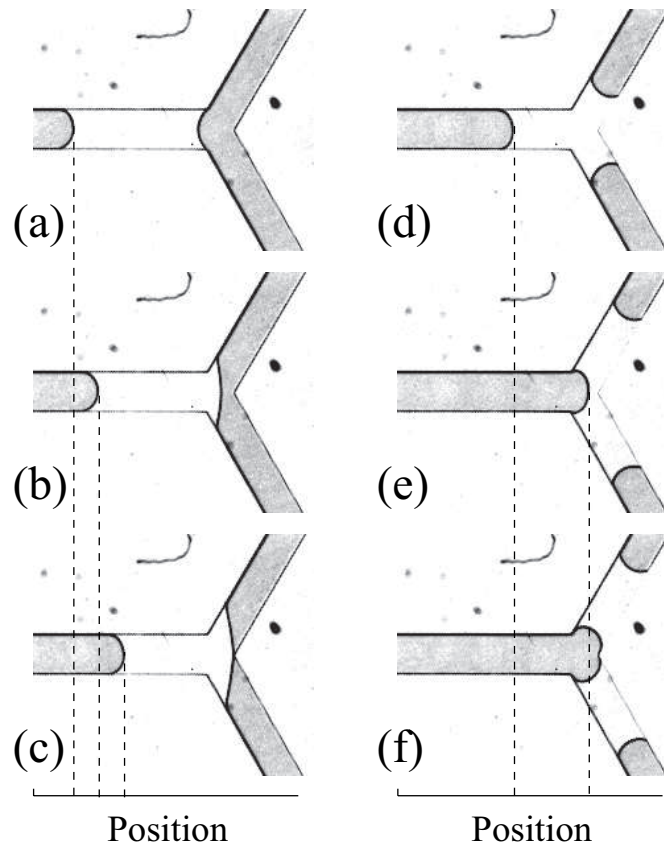
Figure 3.13: Image sequence tracking the plug motion at the bifurcation. The front interface reaches the bifurcation corner (a), deforms afterward (b), touches the opposite wall (c) and finally splits (d). The rear interface becomes affected by the bifurcation after the front one (e) and the plug passes through when the rear interface arrives at the branch in the next generation (f).

Chapter 4

One plug injected into the network

4.1 Experimental observations

We begin our experiments by creating a single liquid plug at the root of the network and push it at a constant pressure or flow rate. The motion of the plug is recorded by the camera connected to the computer. At each bifurcation, the plug divides into two daughters of nearly equal size and these daughters are transported in their respective branches. Different flow patterns are found at different driving conditions.

Constant pressure pushes all the daughters of one plug synchronously in both networks. In these cases, the initial plug slows down and next speeds up while passing the first bifurcation. It then divides into two daughters which move in the second generation. This behavior is repeated by both daughters at later bifurcations, which increases the number of daughter plugs in the network. Those daughters move in synchrony through bifurcations and across generations and the flow is globally symmetric.

In the $\mathcal{N}$ network, at a driving pressure P_{dr}, all the daughters can advance simultaneously to a bifurcation where $P_{\mathrm{dr}} < P_{\mathrm{thr}}$. When the driving pressure is higher than the threshold at the last bifurcation, all the daughters reach the exits of the network. In the $\mathcal{W}$ network, all the daughters can reach the network exits simultaneously as long as the driving pressure P_{dr} is higher than the threshold at the first bifurcation. A typical experiment in the $\mathcal{N}$ network is shown in figure 4.1, where the driving pressure is $P_{\mathrm{dr}} = 250$ Pa. The daughter plugs are labeled with a letter or a letter plus number(s) and their positions are circled for clarity. The plug positions

may vary slightly across the different generations, but they mostly advance in synchrony to the network exits.

However, the flow can be strongly modified when pushed at constant flow rate, for example in the experiment shown in figure 4.2, where the plug is pushed at driving flow rate $Q_{dr} = 2$ μL/min in the $\mathcal{N}$ network. Two daughters, A and B, of the initial plug advance in the same generation simultaneously in image (a) but this synchrony is broken if one of the daughters divides further, as shown in figure 4.2(b) where daughter B passes bifurcation II and its daughters, B1 and B2, advance toward bifurcation III while plug A stops at bifurcation II. After B1 and B2 reach bifurcation III and stop, plug A divides into A1 and A2, both of which then catch up with the early ones. When all the daughters arrive at bifurcation III, plug B2 divides and advances until stopping at bifurcation IV, image (c). After that another plug follows the foregoer, in which way all plugs move forward one by one. The daughters wait for each other at every level of bifurcation, as shown in figure 4.2(d) when they are waiting at bifurcation IV for A2 that is about to pass bifurcation III. The whole network is penetrated by daughters of the initial plug although there are only two daughters of one origin moving at one time.

When the driving flow rate increases to 5 μL/min, the flow symmetry can also be broken by the division of plugs. Nevertheless, the plugs wait for each other at bifurcations and the latecomers can catch up with others. Difference from the experiment shown in figure 4.2 exists since there may be several daughters moving at the same time when $Q_{dr} = 5$ μL/min. All the daughters advance in synchrony when $Q_{dr} = 20$ μL/min and flow looks qualitatively the same as that in figure 4.1. Therefore, the liquid penetrates into all the regions of the $\mathcal{N}$ network regardless of the driving flow rate.

Conversely, in the $\mathcal{W}$ network, the daughter plug blocked at a given upstream bifurcation cannot advance when the driving flow rate is low, as shown in figure 4.3 when $Q_{dr} = 2$ μL/min. Plug B passes bifurcation II in image (b) but plug A gets blocked and remains at bifurcation II until the end of the experiment. Similarly, plug B1 passes bifurcation III in image (c) but plug B2 stops at bifurcation III and stays there. This results in large section of the network with no flow while only a quarter of the network is penetrated by plugs B11 and B12. Asymmetric divisions of the plug, attributed to the imperfection in the fabrication, are found in this case.

An increase in the driving flow rate improves the liquid penetration. When $Q_{dr} = 4$ μL/min, daughters of the initial plug can pass the second bifurcation successively but at bifurcation III half daughters get blocked. At the end, half of the network is penetrated by liquid. When the flow is pushed at $Q_{dr} = 20$ μL/min, the daughters pass bifurcation II together but the crossings of bifurcation III are not simultaneous, resulting in separate advancement of the daughters afterward. No branch is blocked and the whole network is penetrated.

(a) $t = 3$ s

(b) $t = 5$ s

(c) $t = 6$ s

(d) $t = 7$ s
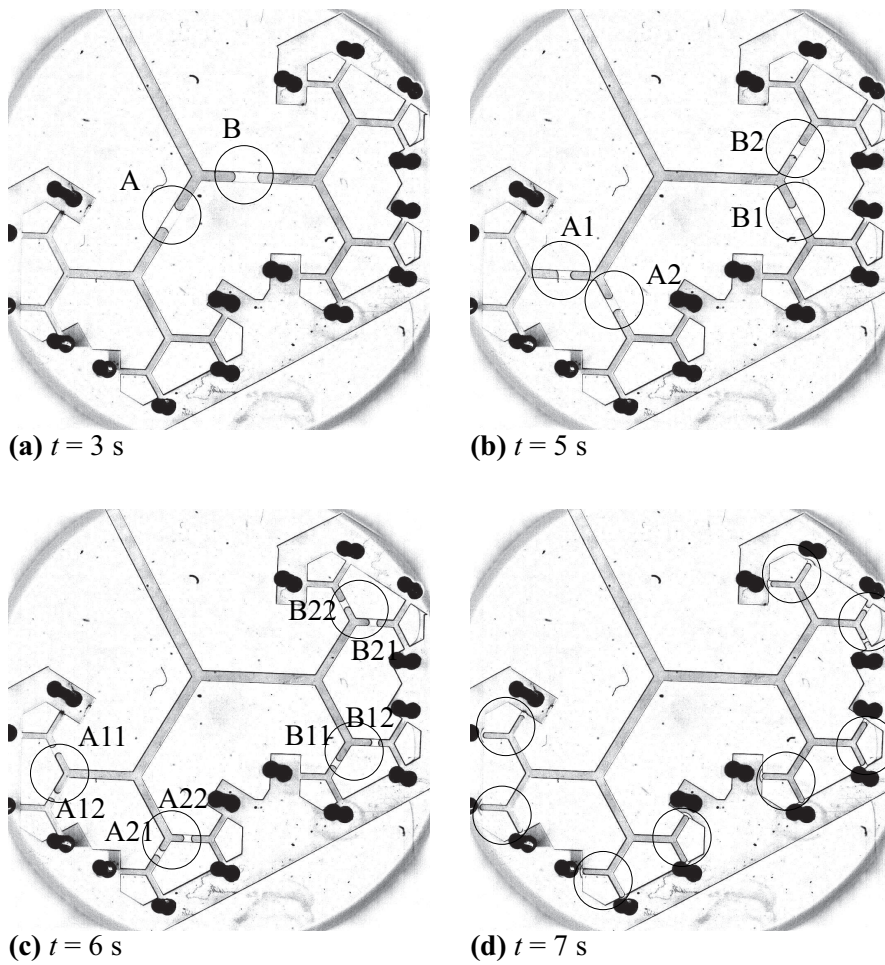
Figure 4.1: Image sequence in the $\mathcal{N}$ network, obtained from experiment under constant pressure driving $P_{\mathrm{dr}} = 250$ Pa. The daughters advance in synchrony through bifurcations and across generations. Each of the daughter plugs is labeled with a letter or a letter plus number(s) and their positions are circled for clarity.

(a) $t = 10$ s

(b) $t = 17$ s

(c) $t = 27.3$ s

(d) $t = 33.3$ s
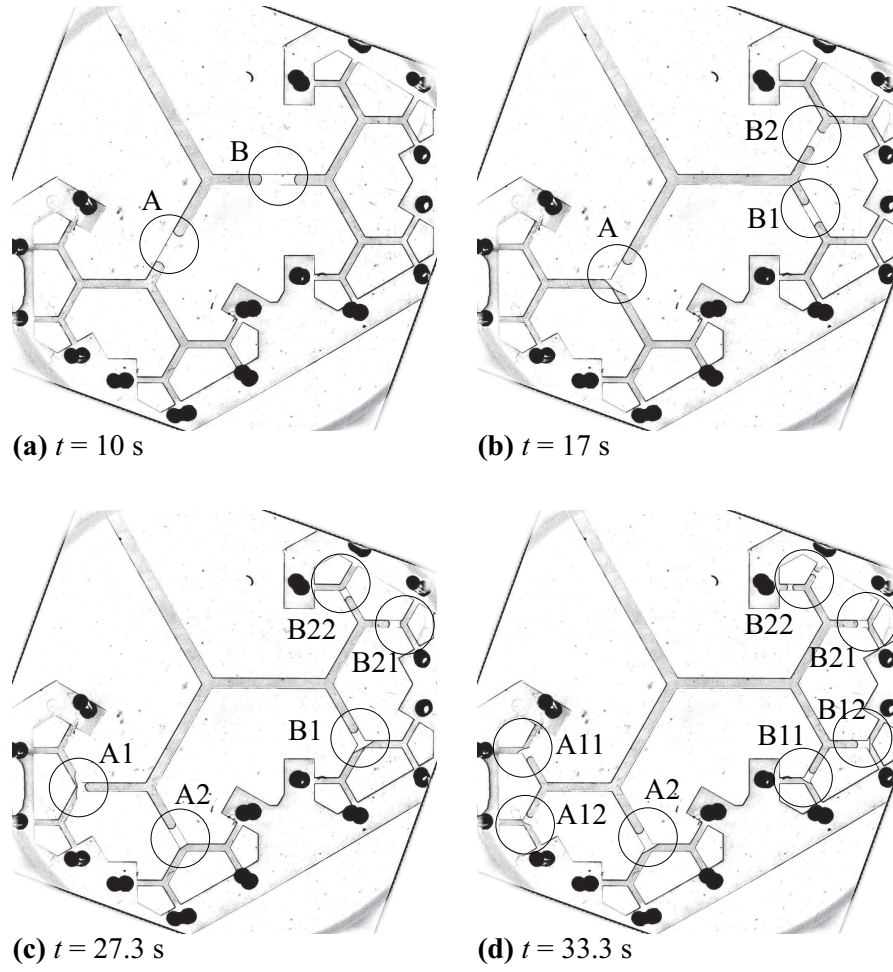
Figure 4.2: Image sequence in the $\mathcal{N}$ network, obtained from experiment under constant flow rate driving $Q_{\mathrm{dr}} = 2$ μL/min. The daughter plugs are labeled and circled for clarity. Two daughters of the same origin advance in the same generation simultaneously but this synchrony is broken when one of the daughters divides further. The latecomers catch up with their sister in downstream bifurcations.

(a) $t = 7.7$ s

(b) $t = 14$ s

(c) $t = 19.7$ s

(d) $t = 22.8$ s
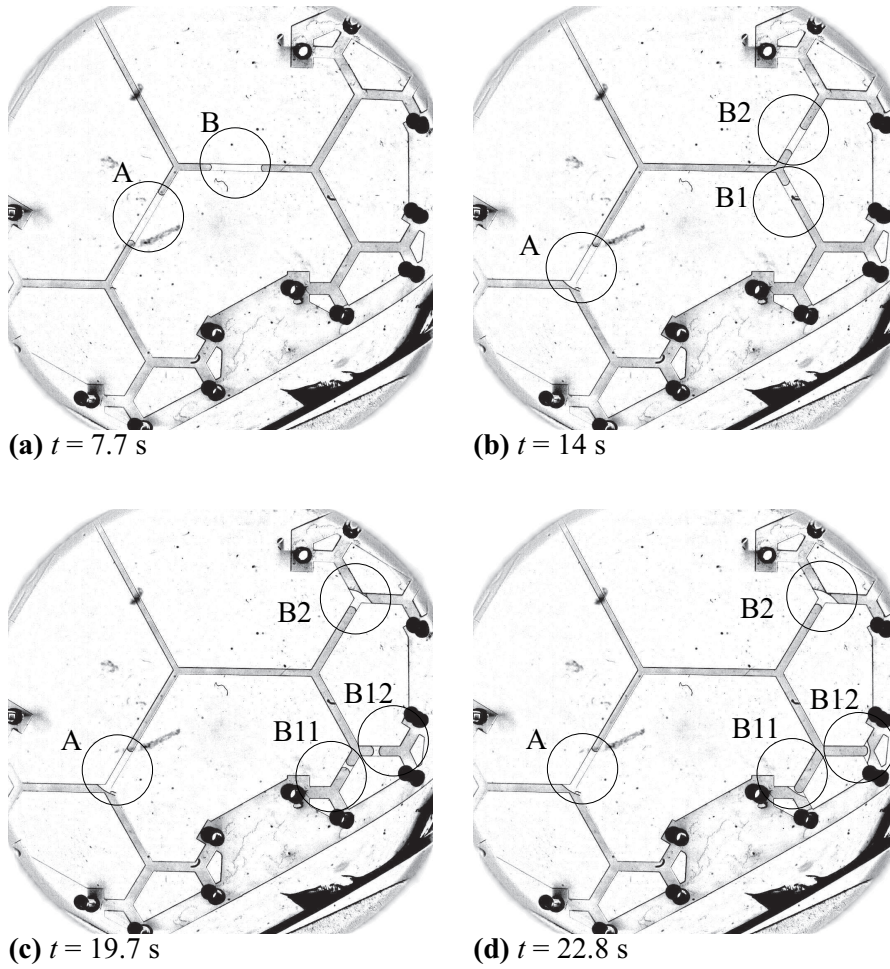
Figure 4.3: Image sequence in the $\mathcal{W}$ network, obtained from experiment under constant flow rate driving $Q_{dr} = 2$ μL/min. The plug cannot move once it gets suck and it blocks the flow in the downstream subregions.
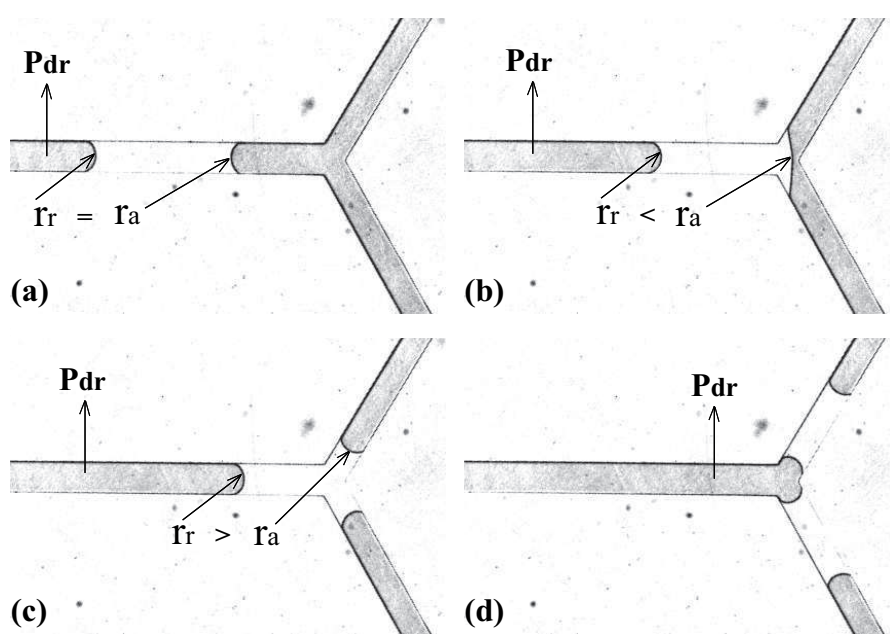
Figure 4.4: Micrographs showing the typical positions in the plug motion: it advances in the straight channel (a), the front interface enters the bifurcation (b), touches the opposite wall and then splits into two (c). After the rear interface touches the opposite wall, the plug divides into two daughters that will advance in their respective straight channels (d).

In the following sections, the flow behavior is studied in detail. Flows under constant pressure and constant flow rate in the $\mathcal{N}$ network are compared and explored in section 4.2. In section 4.3, a model is built to predict the organization of flows containing liquid plugs pushed at constant flow rate in networks with different recursive rules.

4.2   Flow evolutions under different driving conditions

4.2.1   Constant pressure driving

Images showing the typical positions of the plug are summarized in figure 4.4, when the plug is pushed at a constant driving pressure $P_{\mathrm{dr}} = 250$ Pa in the $\mathcal{N}$ network. When the plug moves in the straight channel, it is driven at P_{dr} as shown in figure 4.4(a) where the radii of curvature are $r_{\mathrm{r}} = r_{\mathrm{a}}$. After the plug enters the bifurcation, the deformation of the front interface introduces a capillary complement P_{cap} by varying r_{a} as noted in images (b) and (c), and P_{cap} modifies the pressure across the plug. When the plug fully passes the bifurcation and divides, the resulting two daughters continue to move in their respective channels, image (d). These steps exist in all the passages through bifurcations. Although $2\alpha = 120°$ in our network, unlike the one illustrated in figure 2.15, the equations and analysis in section 2.3 is also applicable by modifying the value of α.
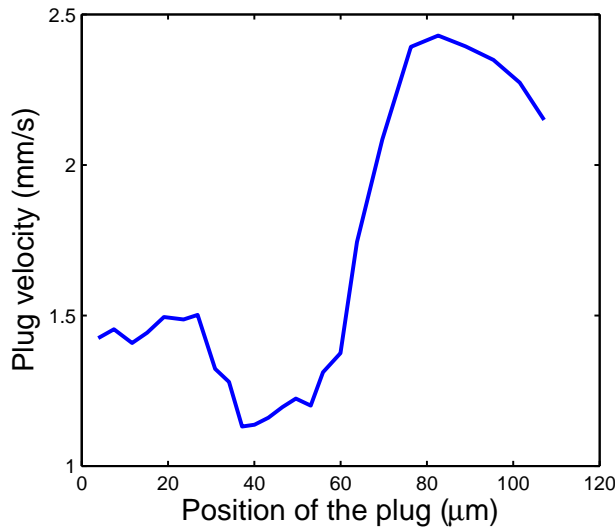
Figure 4.5: Experimental measurements of velocity during the passage of a plug through a bifurcation. The position of the plug is defined as that of its rear interface.

The velocity of one plug, when it is passing the second bifurcation, is measured and plotted in figure 4.5. The evolution indeed accounts for the variation of ΔP during the passage. The plug first slows down in the bifurcation (figure 4.4(b)), followed by a quick acceleration after the front interface reaches the next generation, as shown in figure 4.4(c), since $P_{\text{cap}} < 0$ and $\Delta P = P_{\text{dr}} - P_{\text{cap}}$ increases. Accordingly, the passage of a plug through a bifurcation is always associated with a large spike in the velocity evolution.

A quantitative measure of the overall synchrony of the motion at the pressure driving is given in figure 4.6, which displays the plug velocity as a function of time along four paths, as labeled in figure 3.10(a). As the daughter plugs advance in the network, their number increases and their velocities vary as a result. The spikes that appear in the velocity time series are the signatures of passages through bifurcations, as explained above. By tracking the moment at which the spikes occur along each of the different paths, we see that the plugs reach the bifurcations and divide at roughly the same time. This is in spite of imperfections in the network which lead to slight asymmetry in the divisions and thus yield plugs of variable sizes. Moreover, a careful examination of the time series reveals small differences in the passage times through the second bifurcation. However, this difference is not amplified in later generations and the plugs all continue in a steady fashion. The flow remains globally symmetric during its evolution. Here (and also in the following chapters) the flow evolution after generation 3 is not taken into account, since the plug motion in the last generation can be affected by the boundary condition, which is suggested by large velocity fluctuations in all the paths after generation 3, shown in figure 4.6. Therefore,
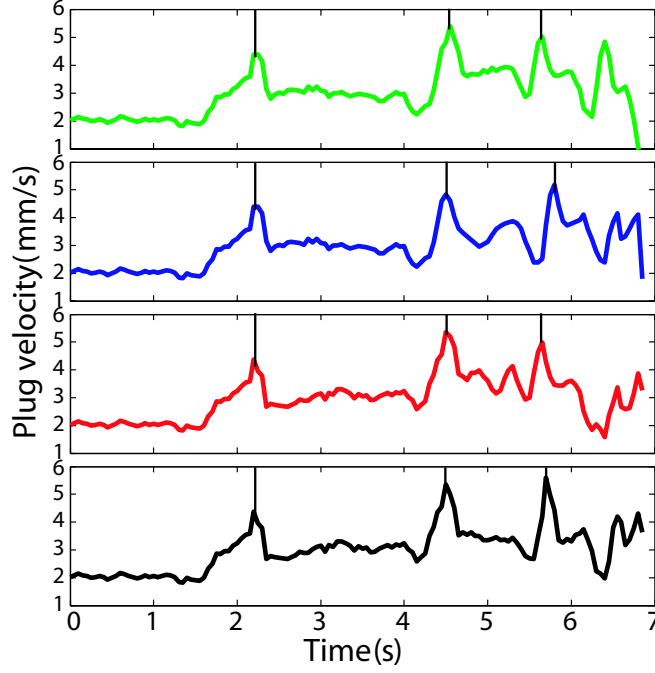
Figure 4.6: Velocity variations along four paths under a constant pressure driving $P_{dr} = 250$ Pa. The vertical line indicates the time when the plug passes a bifurcation. Line colors are coded as in figure 3.10(a).

vertical lines in figure 4.6 locate the passages until bifurcation III although velocity spikes are also observed after that.

The flow behavior under constant pressure can be understood by knowing the thresholds in the network. The driving pressure has to be higher than the threshold when pushing a plug through a given bifurcation. Since the threshold increases in the $\mathcal{N}$ network, the plug can pass the bifurcation when $P_{dr} > P_{thr}$ and stays blocked if P_{dr} becomes smaller than P_{thr}. When P_{dr} is higher than the threshold at the last bifurcation, for example $P_{dr} = 250$ Pa, the plugs can pass all the bifurcations and reach the exits. Meanwhile, since the daughters in every branch are subjected to the same driving pressure, their behavior is the same: All of them either move or stop. The flow thus develops symmetrically.

This also holds in the $\mathcal{W}$ network except that the largest value of P_{thr} corresponds to the first bifurcation: As long as $P_{dr} > P_{thr,1}$, the plug can pass all the bifurcations in the network and the flow evolves symmetrically.

4.2.2 Constant flow rate driving

When the experiments are rerun by pushing the plug at a constant flow rate, the behavior is strongly modified, since long-range interactions develop between plugs at different regions of
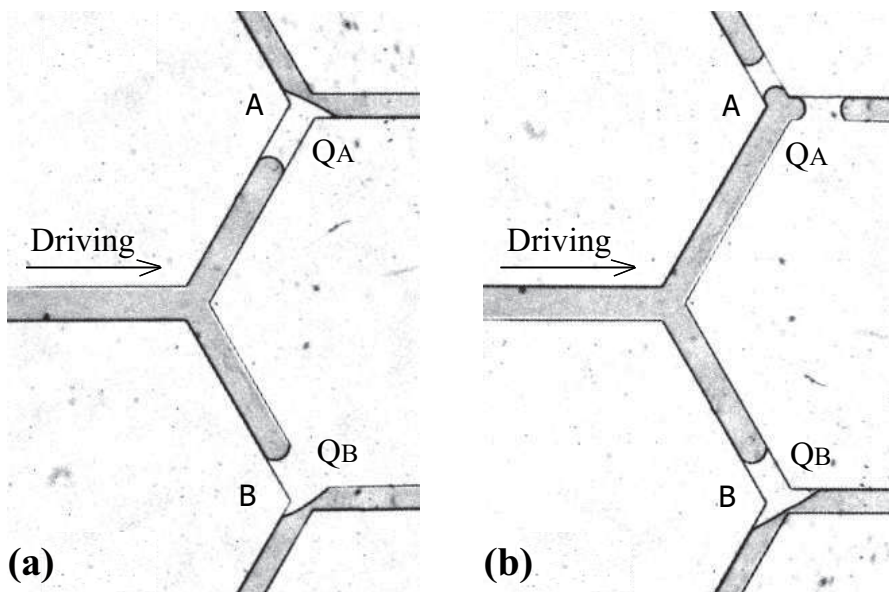
Figure 4.7: The fundamental unit of three connected channels to understand long-range interactions between two plugs under different driving conditions. (a) They both arrive at the bifurcations. (b) Daughter A passes the bifurcation earlier than B.

the network. The fundamental unit to understand these interactions is shown in figure 4.7. Two daughters (A and B) of the same plug arrive at two bifurcations simultaneously in image (a). Slight variations in geometry, which are always present in the experiments, lead to one of the plugs dividing before its sister, as shown in image (b). The velocity of A as well as the flow rate Q_A increase. In case of *constant pressure forcing*, the driving conditions for plug B are not modified; this plug also slows down and then speeds up as it crosses the bifurcation, independently of plug A. This is no longer the case if the plugs are pushed at *constant flow rate*. When the flow rate Q_A increases, Q_B has to decrease due to the conservation $Q_{dr} = Q_A + Q_B$. In fact, Q_B may become zero or even negative, which means that plug B may stop or even move backward, depending on the value of Q_{dr}.

For the experiment shown in figure 4.2 when $Q_{dr} = 2 \ \mu L/min$, the velocities of the plugs are displayed in figure 4.8 along the same paths as above. Due to flow rate conservation in the network, the plugs adjust their velocities while advancing and acceleration in one path leads to deceleration in the others. An uneven division, which introduces daughters of different lengths, leads to significant velocity variations since a shorter daughter is easier to push forward than a longer one. Velocity differences are visible, for instance, in the case of the two daughters of the initial plug as they flow in generation 1: While the one in the black path speeds up, the one in the blue path must slow down.
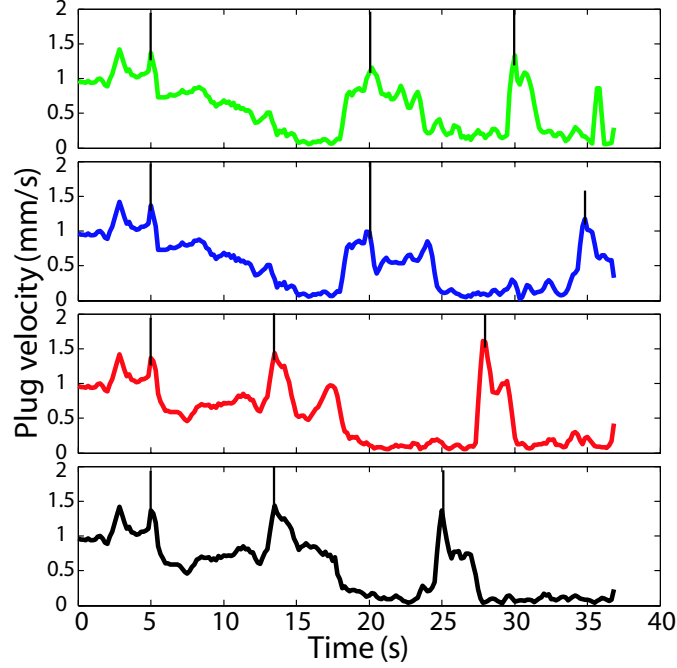
Figure 4.8: Velocity evolutions along four paths under the constant flow rate $Q_{dr} = 2$ μL/min. The vertical line indicates the time when the plug passes a bifurcation. Line colors are coded as in figure 3.10(a).

After one daughter passes a bifurcation and divides, a flow rate increase in the corresponding branches results in a slowing down of other daughters which may get stuck at the bifurcations. Once the early plug that has divided reaches the next bifurcation, the threshold pressures at two successive bifurcations have to be compared and the plug with the lowest threshold will advance first. In the $\mathcal{N}$ network, the threshold increases with the generation number, which implies that the upstream plugs can catch up with the early ones. The most downstream plug must therefore wait at the bifurcation for all other plugs to reach the same bifurcation level before it can continue its journey. This is shown in the velocity evolution in figure 4.8, by the segments with zero velocities before the passage of a bifurcation.

All the daughters eventually reach the network exits, although they do not always advance together. Therefore the flow at $Q_{dr} = 2$ μL/min remains symmetric but evolves through discrete steps. Plugs are never more than one generation apart due to the increasing threshold pressure, but they spend long periods of time stationary at bifurcations, waiting for plugs in the other branches.

4.2.3   Flow patterns in the narrowing network

Results of experiments performed at different driving conditions are summarized in this subsection. As shown earlier, the flow is synchronous at $P_{dr} = 250$ Pa, but turns out to be asynchronous
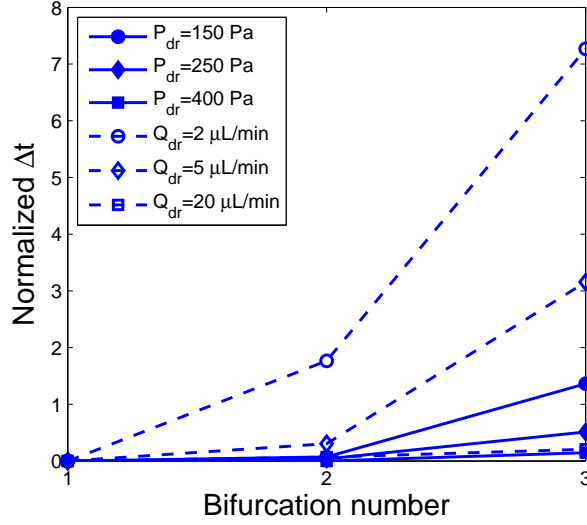
Figure 4.9: Time difference of daughters' passage through bifurcations of the same level, data normalized to the average traveling time in the next generation.

at $Q_{dr} = 2$ μL/min. However, the flow pattern depends not only on the type of the driving condition but also the value of the driving force, as shown below.

The synchrony of flow can be evaluated by measuring the time separating the first and last plug divisions at the same bifurcation level, Δt. This time difference is normalized by the mean time taken to travel through the next generation (T_{i+1}) and is noted here as $\overline{\Delta t}$. $\overline{\Delta t} = 0$ represents a very symmetric flow, where all the daughters pass the bifurcation at exactly the same time. $\overline{\Delta t} < 1$ indicates that the plugs travel nearly simultaneously through the generation, while $\overline{\Delta t} > 1$ implies that divisions are separated by long times and that some plugs spend some time stuck at the bifurcations. In the extreme case of $\overline{\Delta t} = \infty$, there is at least one plug remaining blocked at the bifurcation. $\overline{\Delta t}$ for different experiments are shown in figure 4.9, where each data point corresponds to an average over several experimental realizations.

Two distinct behaviors are observed. Constant pressure driving yields values of $\overline{\Delta t}$ that are below 1, indicating that plug divisions are nearly synchronous. Note that for pressure drivings, the uncertainty in the channel height ± 2 μm will lead to plugs advancing at different velocities due to the variations of the radii of curvature at plug interfaces. This effect is more significant when the plugs pass the bifurcations where ΔP is modified as $P_{dr} - P_{cap}$. ΔP is of the same order of the pressure variation as that brought by the uncertainty in the channel height; $\overline{\Delta t}$ can also display some fluctuations due to imperfections in the channel fabrication, as shown by the points corresponding to $P_{dr} = 150$ Pa in figure 4.9. However, these small fluctuations are introduced by the network itself but not by long-range interactions between daughter plugs. In contrast, the
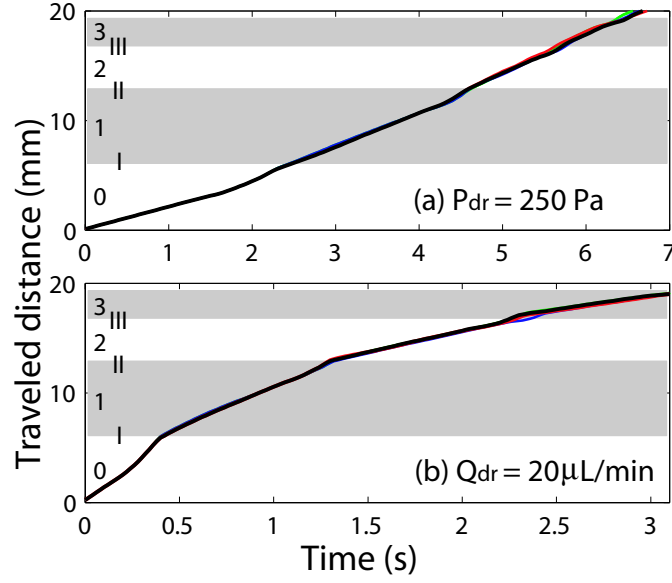
Figure 4.10: Distance traveled by daughter plugs along four paths in the $\mathcal{N}$ network. The shaded and nonshaded areas represent successive generations as labeled on the right of the y-axis by Arabic numerals and the line color is used to indicate the corresponding path shown in figure 3.10. (a) Driving condition $P_{\mathrm{dr}} = 250$ Pa. (b) Driving condition $Q_{\mathrm{dr}} = 20$ $\mu\mathrm{L/min}$.

division times for constant flow rate drivings are above 1 for the second and third bifurcations ($Q_{\mathrm{dr}} = 2$ $\mu\mathrm{L/min}$) and for the third bifurcation ($Q_{\mathrm{dr}} = 5$ $\mu\mathrm{L/min}$). The transition to $\overline{\Delta t} > 1$ occurs when the pressure necessary to ensure the constant flow rate decreases below the local threshold, as will be described in section 4.3. The values of $\overline{\Delta t}$ increase with the generation number here since the number of daughter plugs increases and they must pass separately.

For high driving pressures ($P_{\mathrm{dr}} > 150$ Pa) and flow rate (e.g. $Q_{\mathrm{dr}} = 20$ $\mu\mathrm{L/min}$), the plug movement is synchronous in both methods, as seen by the small values of $\overline{\Delta t}$. This can also be observed by plotting the plug positions as a function of time, as shown in figure 4.10. In this figure, the plug positions along four representative paths, i.e. the distance from the network entrance traveled by the rear interface of the plug, are plotted using four colors. The superposition of distance plots agrees with the fact that all four divide simultaneously both in constant pressure and constant flow rate drivings. However, the plots display different flow evolutions, which allows us to distinguish the driving conditions nevertheless. While the plugs slightly accelerate in the first four generations in case of pressure forcing in agreement with data in figure 4.6, they experience a clearly deceleration as advancing under flow rate driving, since the number of daughters increases and the flow is distributed over a larger total area.

This information is confirmed by measuring the time spent traveling in the straight sections in each generation (T_i), as shown in figure 4.11. Here, each data point represents the average over all the daughters in a given generation and is shown with error bars for several experimental
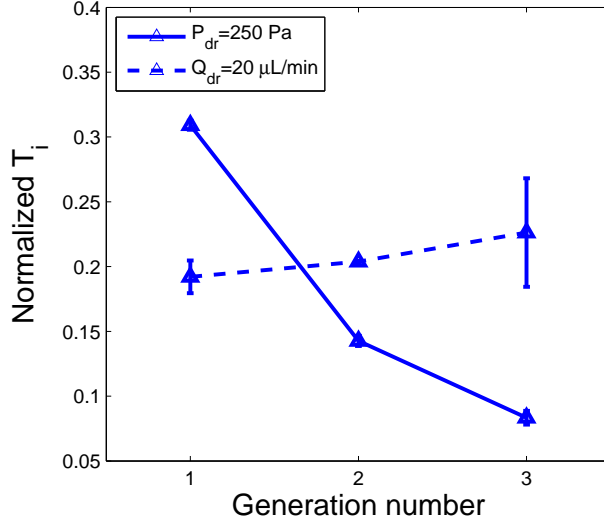
Figure 4.11: Comparison of traveling time in each generation for pressure and high flow rate drivings, which yield symmetric flow patterns.

realizations. T_i is normalized by the total time for an experiment, i.e. the time from the initial plug entering the first bifurcation to the last daughter passing the last bifurcation before exits. For our network, we observe that the plugs spend a shorter time in the straight channel as they advance when pushed at constant pressure. It is known from figure 4.6 that the plug velocity increases from generation 0 to 2 and varies slightly from generation 2 to 3 under $P_{\mathrm{dr}} = 250$ Pa. Since the channel length decreases at the ratio 0.6, it takes a shorter time to pass the branch for plugs in later generations. When the plug is pushed at a high flow rate, the travel time remains constant with the generation number. This is because the plug velocity in successive generations evolves as:

$$
\begin{aligned}
U_{i+1} &= \frac{Q_{\mathrm{dr}}}{N_{i+1} h w_{i+1}} = \frac{Q_{\mathrm{dr}}}{2 N_i h \rho w_i} \\
&= \frac{1}{2\rho} U_i = 0.6 U_i,
\end{aligned}
\tag{4.1}
$$

which is in the same way as the decrease of the channel length.

4.3 Flow organization in different networks

4.3.1 Network with narrowing channels

In the previous section, we have seen that the flow evolution in the $\mathcal{N}$ network under flow rate driving was more complicated than plug dynamics under pressure driving and that the flow

Figure 4.12: Traveled distance (left column) and velocity evolution (right column) of daughter plugs along four paths as a function of time in the $\mathcal{N}$ network. Driving flow rates vary as: (a) 2 μL/min (b) 5 μL/min (c) 20 μL/min. Line color is coded as in figure 3.10. In the left column, the shaded and nonshaded areas represent successive generations as labeled to the right of the y-axis by Arabic numerals. In the right column, a large velocity spike denotes the passage through a bifurcation that is located by a vertical line.

organization was strongly affected by the evolution of threshold pressures in the network. We now focus on the constant flow rate driving in two different networks ($\mathcal{N}$ and $\mathcal{W}$).

A single plug pushed at a constant flow rate in the $\mathcal{N}$ network is first considered. The distances traveled by the rear interfaces of the daughter plugs from the network entrance are measured and shown in figure 4.12 in the left column. Three typical experiments are recorded in this figure and the results are observed in many experiments under the same condition. The color of the line denotes the path along which the daughter plug moves and the shaded and nonshaded areas represent successive generations as labeled to the right of the y-axis by Arabic numerals. The velocity measurements are given in figure 4.12 in the right column, where the passage through a bifurcation can be distinguished by a large velocity spike.

In the experiment at a low flow rate ($Q_{\mathrm{dr}} = 2$ μL/min), the plug initially flows in generation 0 until it reaches the first bifurcation at which it divides into two daughters. During this period, the single black line, in figures 4.12(a1) and (a2), leads to two lines (black and blue) for the two daughters. For simplicity, the color will be used to identify the plug in that branch in the following descriptions. The blue plug accelerates, decelerates and then stops at bifurcation II. From this point, a horizontal segment in blue below the border of generations 1 and 2 is observed in figure 4.12(a1) and the velocity goes down to zero in (a2). Whereas, the velocity of the black

plug decreases before increases again, which is just the opposite behavior of its blue sister. The black one however passes bifurcation II before the blue and its daughters (black and red) advance to bifurcation III, where they stop. At this point, the blue plug divides through bifurcation II and catches up with the black and red daughter plugs. The difference in traveled distance between the blue and black, or green and red, which has increased up to one generation, decreases again. When all of the four daughters have arrived at bifurcation III, the black one starts to advance to the next bifurcation. After that the red, green and blue plugs divide one by one and travel to the next bifurcation. It is clearly seen in figure 4.12 (a2) that the passages of bifurcation III are well separated in time.

The evolution of distance plots for $Q_{\mathrm{dr}} = 5$ μL/min, figure 4.12(b1), is similar except that the blue plug divides at bifurcation II while the daughters of the black are still moving in generation 2. This corresponds to a period when flow exists in both branches and the difference in traveled distance between the blue and black has not increased much. Also, two close spikes for bifurcation II are seen in figure 4.12(b2). At the next bifurcation, three daughters also pass through simultaneously and travel in generation 3 thereafter. Only the blue daughter that passes bifurcation III later than its sisters advances on its own in generation 3. Nevertheless, all of them reach the next bifurcation.

Finally, when the driving flow rate increases to $Q_{\mathrm{dr}} = 20$ μL/min, the daughter plugs can advance simultaneously all along their journeys in the network. Therefore, the distance plots are all superposed in figure 4.12(c1) and the velocity spikes for the same level of bifurcation are all close to each other in 4.12(c2). With different evolutions, the liquid plug penetrates everywhere in the $\mathcal{N}$ network in all the three cases regardless of the driving flow rate.

4.3.2 Network with widening channels

The flows in the $\mathcal{W}$ network are quite different from those in the $\mathcal{N}$ network. In comparison, the single plug is also pushed at low, medium and high flow rates in experiments. The traveled distance is plotted in figure 4.13 in the left column and the velocity evolution in the right column.

The initial behavior of the plug at $Q_{\mathrm{dr}} = 2$ μL/min is similar to that in the $\mathcal{N}$ network but a difference arises at bifurcation II. At this stage, the blue daughter of the initial plug is blocked and remains stationary until the end of the experiment, which is shown by the horizontal blue line in figure 4.13(a1) and the blue velocity curve of value zero in figure 4.13(a2). The other plug, the black one, divides at bifurcation II and its daughters reach the next bifurcation together. Similar to the behavior of the blue plug, the black daughter stops at bifurcation III and remains there, which leaves only the red daughter continuing advancing. In the end, only the red daughter passes generation 3. On the velocity plots, only a red spike exists while all the other curves
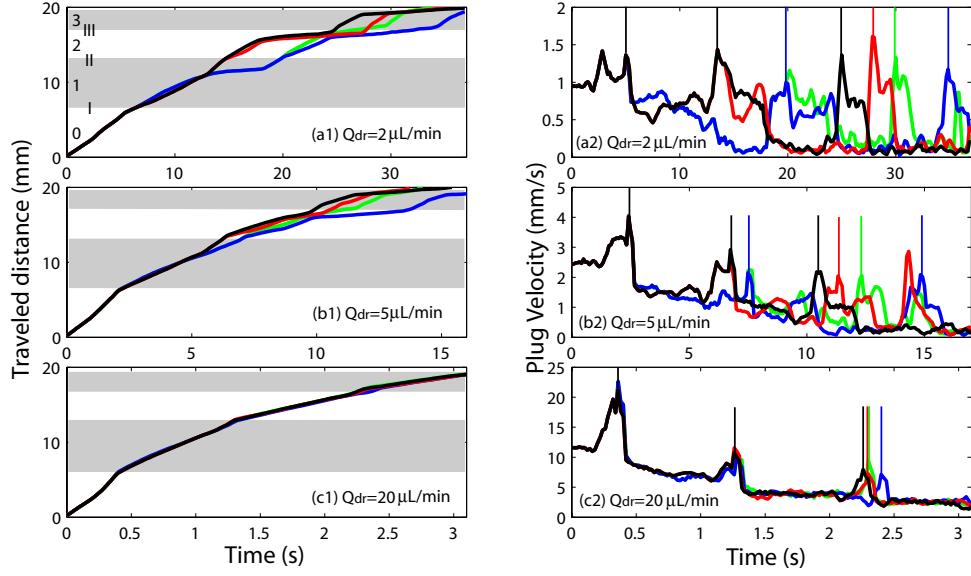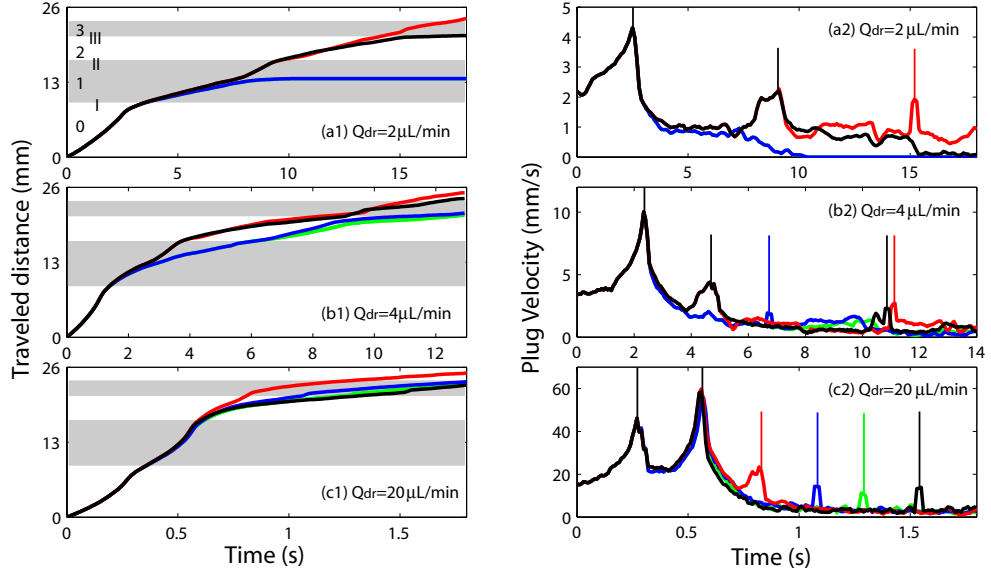
Figure 4.13: Traveled distance (left column) and velocity evolution (right column) of daughter plugs along four paths as a function of time in the $\mathcal{W}$ network. Driving flow rates vary as: (a) 2 μL/min (b) 4 μL/min (c) 20 μL/min. Line color is coded as in figure 3.10. In the left column, the shaded and nonshaded areas represent successive generations as labeled to the right of the y-axis by Arabic numerals. In the right column, a large velocity spike denotes the passage through a bifurcation that is located by a vertical line.

have value zero. Since there is no flow in branches downstream of a bifurcation where a plug is blocked, the flux is limited to only a quarter of the network on the level of generation 3 when the driving flow rate is low, i.e. $Q_{\mathrm{dr}} = 2$ μL/min.

For $Q_{\mathrm{dr}} = 4$ μL/min, daughters of the initial plug pass bifurcation II successively but only two daughters (black and red) pass through bifurcation III, while the other two get blocked. At the end, flow develops in half of the network. Accordingly, two spikes (black and red) are observed for the passage through bifurcation III in figure 4.13(b2), although they look small compared to the biggest one at the first bifurcation due the strong decrease of daughter velocities.

When the flow is pushed at $Q_{\mathrm{dr}} = 20$ μL/min, the daughters pass bifurcation II together but the crossings of bifurcation III are not simultaneous, resulting in asynchronous advance of the daughters afterward as shown in figure 4.13(c1). As a result, four separated spikes are found in figure 4.13(c2). Nevertheless, the whole network is penetrated at this high flow rate.

According to its definition, $\overline{\Delta t}$ goes to infinity for flows pushed at low and medium flow rates in the $\mathcal{W}$ network since daughters are blocked at intermediate bifurcations before reaching the exits. When $Q_{\mathrm{dr}} = 20$ μL/min, $\overline{\Delta t}$ decreases strongly but the daughters still do not advance synchronously.
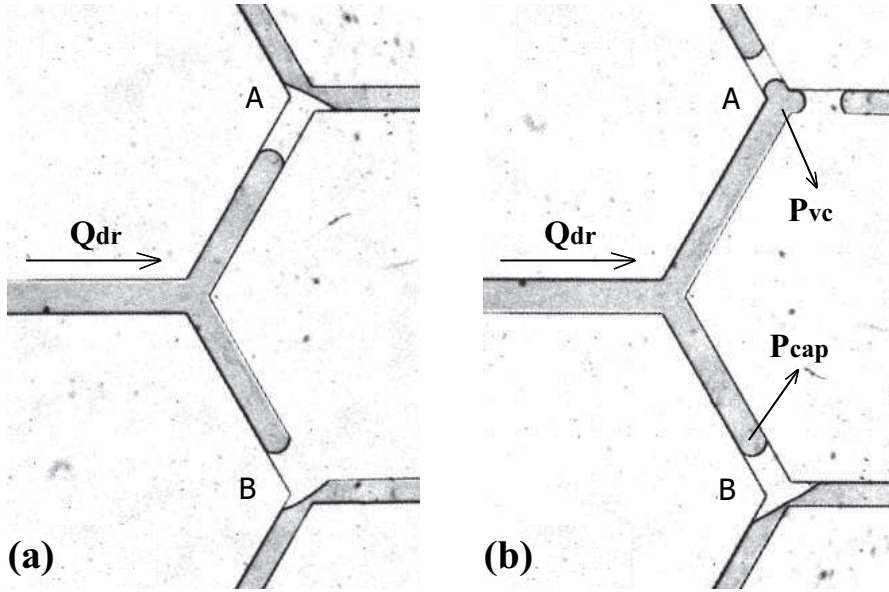
Figure 4.14: Basic building block consisting of three connected bifurcations for exploring the long-range interactions between different plugs and the global behavior in the binary branching network under constant flow rate driving.

4.3.3 Global organization of the flow

The different flow behaviors in two networks can also be understood from the long-range interactions across distinct subregions of the network introduced by the nonlinear pressure–position relation when several plugs are present.

We again use the unit consisting of three connected bifurcations, as shown in figure 4.14. Unlike in figure 4.7 where the plugs are pushed either at pressure or flow rate, here figure 4.14 represents the building block to understand plug interactions under constant flow rate driving and explain the global behavior in the binary branching network. In image (a), the front interfaces of plugs A and B are both deformed and the common pressure ΔP driving the two plugs is given by P_{cap}. After plug A divides, as shown in figure 4.14(b), the behavior of plug B will be affected, since the flow is pushed by a constant flow rate. Given that the flux in the system is fixed and imposed by the syringe pump, ΔP will adjust to satisfy relation (2.1), evaluated for the two daughters of A moving at the velocity $U = Q_{\mathrm{dr}}/2wh$, where w is the width of the channel in which the two daughters move. The behavior of plug B can then be deduced by comparing P_{vc} for the moving daughters of plug A and P_{thr} at the bifurcation. If $P_{\mathrm{vc}} < P_{\mathrm{thr}}$, plug B cannot pass the bifurcation. It adjusts its position to equilibrate $P_{\mathrm{cap}} = \Delta P$ and stays there. If $P_{\mathrm{vc}} > P_{\mathrm{thr}}$, plug B passes the bifurcation and introduces two new daughters into the system. This leads to a new value of ΔP that has to be calculated using (2.1) for four daughter plugs moving in the next generation.

Considering the network, this process has to be generalized to the case from 1 to 2^{i-1} plugs that are dividing at the ith bifurcation, which gives a range of possible values for $\Delta P = P_{\mathrm{vc}}$ in generation i, as shown by the shaded areas of figure 4.15. When the first plug passes the bifurcation, the motion of its two daughters conserves the total flow rate in the network, which requires a high P_{vc}. At this moment, there exists the maximum possible value of P_{vc} in generation i. All these maximum values in different generations are connected to form the top line of each shaded area in figure 4.15. As more plugs pass the bifurcation they have entered, the number N of the moving plugs increases and $\Delta P = P_{\mathrm{vc}}$ decreases as a result. As long as $P_{\mathrm{vc}} > P_{\mathrm{thr}}$, the late plugs continue to pass the bifurcation and introduce more daughters, which lowers ΔP even more. When ΔP becomes lower than P_{thr}, some plugs in the ith bifurcation remain blocked at a position where $P_{\mathrm{cap}} = \Delta P$ is achieved. If all the plugs pass the bifurcation, N reaches its maximum value 2^i in generation i, and P_{vc} is expected to take on the minimum value in that generation. The bottom lines in figure 4.15 displays these minimum P_{vc} values as functions of the generation number and network.

Given the relative values of P_{vc} and P_{thr} for each generation in figure 4.15, the flow behavior under different flow rate drivings can be predicted up to 10 generations in the narrowing ($\mathcal{N}$) and widening ($\mathcal{W}$) networks. When the driving flow rate is low, $Q_{\mathrm{dr}} = 2$ μL/min, we have $P_{\mathrm{vc}} < P_{\mathrm{thr}}$ and only one plug can pass the bifurcation at one time. Since $P_{\mathrm{vc}} > P_{\mathrm{thr}}$ in the first four generations when $Q_{\mathrm{dr}} = 20$ μL/min, all the daughters can move and divide together. However, for a network with more generations, in the later region where P_{thr} overlaps P_{vc}, some of the daughters can advance simultaneously but some others have to stop at the bifurcations they have entered. When the plug is pushed at a medium flow rate, e.g. $Q_{\mathrm{dr}} = 4$ μL/min or 5 μL/min, the threshold pressure curve overlaps the range of P_{vc} that is placed between the two shaded areas in the figure. Therefore, some daughters move together through the bifurcation while others stop there.

The main difference between the two networks appears once the plug that has divided earlier reaches the next bifurcation. The threshold pressures associated with two successive bifurcations must be compared at this stage and the plug with the lower threshold will divide. For convenience, the definition of P_{thr}, which is given in (2.6), is repeated below:

$$P_{\mathrm{thr}} = \frac{2\gamma \cos\theta}{w_i} - \frac{\gamma(\cos\theta - \sin\alpha)}{w_{i+1}}. \tag{4.2}$$

Taking into account the variation of w_i in successive generations, P_{thr} can be also expressed as:
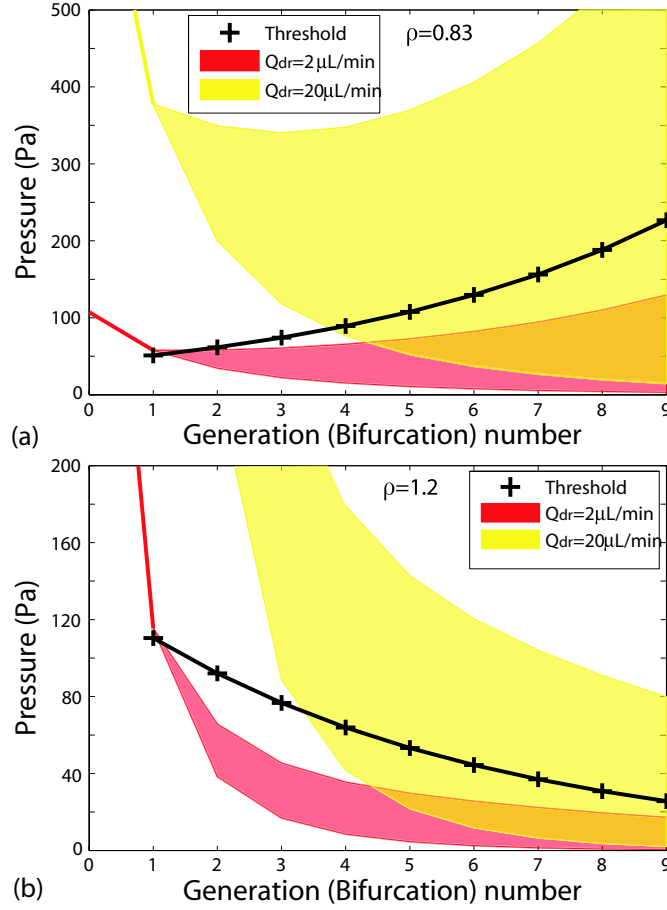
Figure 4.15: Comparison of threshold pressures at every bifurcation to the pressures imposed in the straight channels by the driving flow rates $Q_{\mathrm{dr}} = 2$ μL/min and 20 μL/min. Labels on the x-axis denote the bifurcation numbers for the thresholds and the generation numbers for the viscocapillary pressures. (a) $\mathcal{N}$ network (b) $\mathcal{W}$ network.

$$P_{\mathrm{thr},i+1} = \frac{2\gamma\cos\theta}{w_{i+1}} - \frac{\gamma(\cos\theta - \sin\alpha)}{w_{i+2}}$$
$$= \frac{1}{\rho}\left(\frac{2\gamma\cos\theta}{w_i} - \frac{\gamma(\cos\theta - \sin\alpha)}{w_{i+1}}\right) \tag{4.3}$$
$$= \frac{1}{\rho}P_{\mathrm{thr},i},$$

which means that P_{thr} varies with the generation number as $P_{\mathrm{thr},i+1} = (1/\rho)P_{\mathrm{thr},i}$. This leads to $P_{\mathrm{thr},i+1} > P_{\mathrm{thr},i}$ in the $\mathcal{N}$ network and $P_{\mathrm{thr},i+1} < P_{\mathrm{thr},i}$ in the $\mathcal{W}$ network.

For a plug injected from the entrance of the $\mathcal{N}$ network, it gets harder to push it through bifurcations as it advances. It is also harder for the plug located at a downstream bifurcation $(i+1)$ to pass than the plug in a upstream bifurcation (i) for the same reason. In other words, the upstream plugs always divide before plugs in the downstream bifurcations. This implies that the advance of a downstream plug to an upstream plug cannot exceed one generation in a narrowing network. In contrast, $P_{\mathrm{thr},i}$ continuously decreases in the $\mathcal{W}$ network. The downstream plug always divides first and the upstream plug can no longer advance once it is stuck at the bifurcation. The distance between plugs can grow indefinitely.

The above analysis indicates that all the daughter plugs can advance to the same level of generation in the $\mathcal{N}$ network regardless of the driving flow rates, which is in agreement with the experimental observation in figure 4.12. However, the flow may evolve in different ways depending on the value of P_{vc}. When $Q_{\mathrm{dr}} = 2 \ \mu\mathrm{L/min}$, $P_{\mathrm{vc}} < P_{\mathrm{thr}}$, plugs advance one after another, in agreement with the experimental observation in figure 4.12(a). Since $P_{\mathrm{vc}} > P_{\mathrm{thr}}$ in the first four generations when $Q_{\mathrm{dr}} = 20 \ \mu\mathrm{L/min}$, the plugs move together, as confirmed by the experiment results in figure 4.12(c). For the region between the two flow rates, P_{thr} overlaps P_{vc} and some of the daughters first advance simultaneously. But the early ones will be caught up by the latecomers at a downstream bifurcation, as shown in figure 4.12(b) for example.

In contrast, only fast daughters can reach the exits of the $\mathcal{W}$ network while others get blocked at intermediate bifurcations. When $P_{\mathrm{vc}} < P_{\mathrm{thr}}$, only one daughter can advance while all the others are blocked at different level bifurcations, in agreement with the experiment shown in figure 4.13(a) for $Q_{\mathrm{dr}} = 2 \ \mu\mathrm{L/min}$. However, since $P_{\mathrm{vc}} > P_{\mathrm{thr}}$ for $Q_{\mathrm{dr}} = 20 \ \mu\mathrm{L/min}$, all the daughters are pushed to the exits (figure 4.13(c)). Given a network with more generations, we can predict that P_{thr} will intersect the predicted range of P_{vc} after the divisions of a few plugs due to the strong decrease of P_{vc} with the generation number. At this stage, some plugs will stop before reaching the exits. This phenomenon is also observed when P_{thr} intersects the range of P_{vc} predicted for $Q_{\mathrm{dr}} = 4 \ \mu\mathrm{L/min}$ in the experiment shown in figure 4.13(b).

4.4 Summary

In studying the flow evolution when a single plug is pushed into the network at either a constant pressure or a constant flow rate, we have identified the capillary pressure difference across the plug introduced by the deformation of air-liquid interfaces during the passage through a bifurcation. The resulted nonlinear pressure–position relation can influence the velocity at which the plug advances in the bifurcation. When several daughter plugs and bifurcations are present, these nonlinearities can further introduce strong long-range interactions between plugs in different parts of the network when the flow is pushed at constant flow rate. This is particularly visible when the flow rate is low and some plugs stop at bifurcations and wait for long periods of time while others continue to advance.

In a branching network with narrowing channels, the liquid plug pushed at constant pressure can penetrate all the branches with daughters moving in synchrony as long as the driving pressure is higher than the thresholds in the network. But in a tree that is sufficiently deep with many generations, the driving pressure will become lower than local threshold at a later bifurcation, since the threshold increases with the bifurcation number. Therefore, the liquid cannot reach the end of network. However, when the plug is pushed at constant flow rate, the tree with narrowing branches can be fully invaded and this is regardless of the value of the driving flow rates. Although daughters advance one after another at low driving flow rate, the fast ones always wait for others at downstream bifurcations.

Conversely, a constant pressure can push plugs to the end of the widening tree when the pressure is higher than the threshold at the first bifurcation. Since the threshold decreases with the bifurcation number, the plug will advance to the network exits once it passes bifurcation I. In the other case, when the flow is driven at constant flow rate, only fast daughters can reach the end of the tree since they always reach the next bifurcation associated with a lower threshold and the daughters blocked at a upstream bifurcation cannot advance any more. Although the fully invasion of the $\mathcal{W}$ is observed in experiments, it is predicted that a network with more generations will not be invaded by plugs driven at constant flow rate.

For a network other than the microfluidic models, the analysis of the plug passage through a bifurcation also leads to the existence of a threshold value of the driving pressure. A similar threshold is expected to exist in the case of the circular tubes forming the pulmonary airway tree, although its value will strongly depend on the details of the geometry at the bifurcation. In this sense, a better understanding of the penetration of liquid plugs into the branching tree and of the long-range interactions in the tree should lead to improved models of liquid dispersion in the lung, which is an important problem in view of its application to pathology and drug delivery.

More broadly, a basic building element consisting of three adjacent bifurcations is identified for the analysis of the dynamically determined viscocapillary pressure and the geometrically controlled threshold value. This element can be used to build any network topology and the analysis approach can be adapted to the general case. Therefore, the global transport of liquid plugs in the network can be inferred from the interactions inside one element and between different elements. Generalizing these results can have insights for many technological applications.

Chapter 5

A train of plugs in the network

Article appeared in *Medical Engineering & Physics* (2010), published online.

When several plugs are injected successively into the network, the nonlinearities associated with one plug motion can influence the advancement of other plugs, which makes the flow evolution more complex. Besides interactions between daughters of the single plug in different subregions of the network, there also exist interactions between daughters of different plugs. In this chapter, the flow containing successive plugs pushed at constant pressures is studied in the $\mathcal{N}$ network and a simple empirical relation is found to predict the total flow rate in the presence of a train of plugs. We begin from the case of a single plug injected into the network, build a relation reproducing the results and then show that this relation can be applied to the case of a train of plugs successively injected.

5.1 Empirical resistance to flow associated with one plug

In this section, we focus on the lengths and velocities of daughters of a single plug pushed at a constant pressure $P_{\mathrm{dr}} = 250$ Pa as they travel in the straight channels between two successive bifurcations in the $\mathcal{N}$ network. The daughter plugs are constantly subjected to the same pressure difference and should therefore all move at the same speed which in addition should be constant during their passage in their respective branches.

For one plug moving in a straight channel, its velocity is measured as: $U = [x_{\mathrm{r}}(t) - x_{\mathrm{r}}(t - \mathrm{d}t)]/\mathrm{d}t$, which is rewritten here for convenience. During the plug travel in one branch, U varies slightly as a function of t. The time-averaged value of plug velocity U in one branch is taken and plotted as one symbol $\Diamond$ in figure 5.1 according to the plug position in the network, generation i. There are therefore 2^i data points in generation i. The solid line drawn through these points
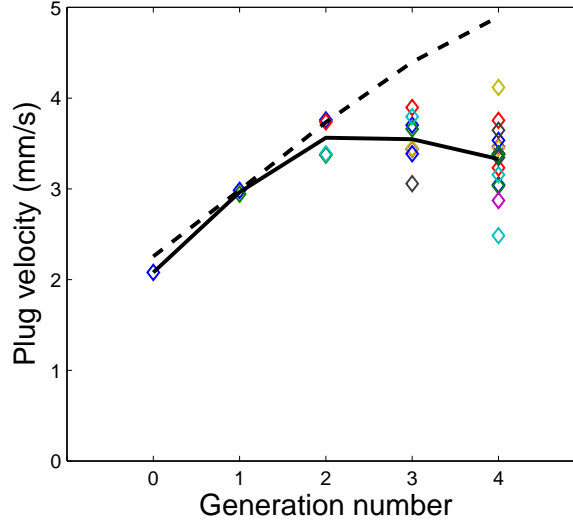
Figure 5.1: Average plug velocity as a function of the generation number i. Experimental conditions: $P_{\mathrm{dr}} = 250$ Pa and $L_0 = 2.3$ mm. Symbols correspond to values recorded in each branch and the solid line to their average. The prediction from (2.4) is shown as a dashed line.

gives the average obtained over the 2^i branches. Variations from branch to branch and within a branch, to be attributed to imperfections in the microfabrication, are observed however. As the channels get narrower, the flow becomes more sensitive to wall conditions, which brings bigger separations between data points in later generations.

At this stage, it is interesting to compare these observations to the theoretical prediction of (2.4), which is used to compute the velocities in all the generations by assuming that plugs divide equally at each bifurcation while taking into account the narrowing of the channels, $w_i = w_0 \rho^i$, hence $L_i = L_0/(2\rho)^i$. The result is given as a dashed line in figure 5.1, from which it is immediately seen that the daughters experience a resistance larger than predicted as they progress in the network. Since the formula is well validated in the case of long plugs, the discrepancy is attributed here to the exponential shortening of the plugs with the generation number: For the experiment corresponding to the data in figure 5.1, the plug length in the last generation is $L_4 = 310$ μm while the channel width is $w_4 = 340$ μm. Plugs are therefore comparatively short and the resistance is underestimated in later generations.

The limitations of the theory led to the development of an empirical relation that is described in the following. As for an electrical network, we define a resistance $R_i L_i$ associated with the presence of daughter plugs in generation i, where the role of the voltage is played by the driving pressure P_{dr} and the role of the current intensity by the total volumetric flow rate Q_{t} that varies with the generation number. By assuming further that each plug divides into two
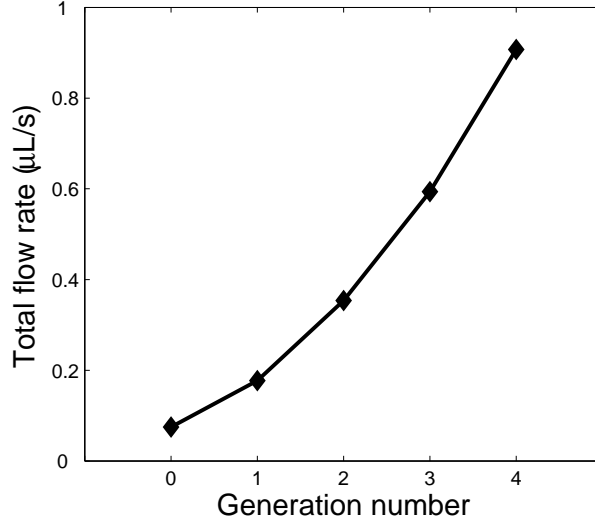
Figure 5.2: Evolution of the total flow rate in the network. Experimental data is obtained from a single plug case: $P_{\mathrm{dr}} = 250$ Pa and $L_0 = 2.3$ mm and used for computing R_i.

daughters of essentially equal lengths at every bifurcation, $L_i = L_0/(2\rho)^i$, which is consistent with experimental observations, we can therefore write:

$$P_{\mathrm{dr}} = R_i L_i Q_{\mathrm{t}}. \tag{5.1}$$

For the experiment shown in figure 5.1, Q_{t} is given in figure 5.2 by $Q_{\mathrm{t}} = \sum_{ii} Q_{i,ii} = \sum_{ii} U_{i,ii} h w_i$ with $Q_{i,ii}$ and $U_{i,ii}$ being the mean flow rate and velocity of the daughter plug in branch ii of generation i, in which ii denotes the numbering of branches in generation i. The values of R_i can be computed from the measurements since the driving pressure, the initial length of the plug and the flow rate based on velocity measurements are known. The resistance $R_i L_i$ is found to decrease when the plug advances, as shown in figure 5.3, which leads to the increase of the total flow rate as the plug reaches later generations (figure. 5.2).

5.2 Two plugs injected into the network

5.2.1 Flow rate dependence on the initial distance between plugs

An image from a two-plug experiment is shown in figure 5.4, where the two plugs are injected successively into the network. The daughters (A and B) of the plug initially injected have reached generation 1 while the second plug (C) is moving in generation 0.

This time the plugs are pushed at $P_{\mathrm{dr}} = 500$ Pa through the network entrance, upstream the second plug, and the initial lengths of the two plugs are 1.8 ± 0.2 mm while the initial distance between them is varied in different experiments. The initial states of the plugs are chosen as

Figure 5.3: Dependence of the resistance $R_i L_i$ on the generation number i. The resistance decreases as the generation number increases.

Figure 5.4: Experimental image of two plugs injected successively into the network. Two early plugs (A and B) in generation 1 are daughters of the plug first injected. The second plug (C) is moving in generation 0.

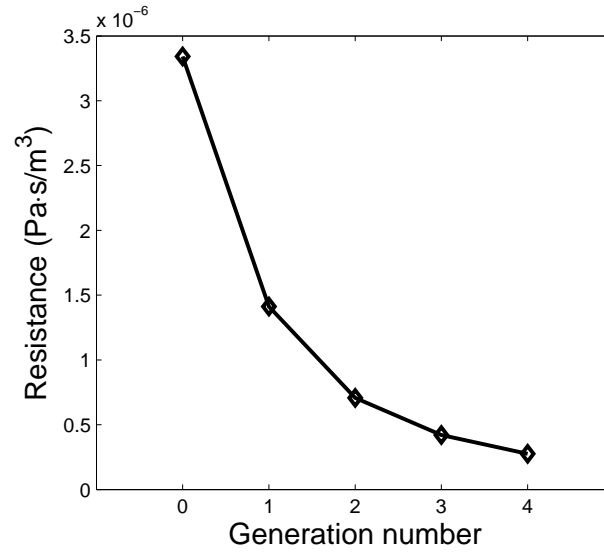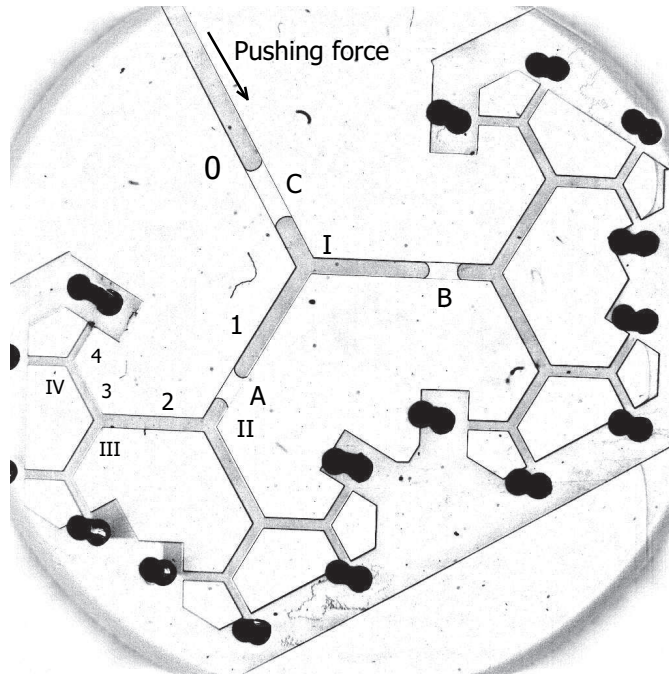shown in figure 5.5, which yields different flow patterns in the network. In case (a), the two plugs are injected closely one after the other through the network entrance, generation 0. The initial distance between them is ΔD=3.0 mm, ΔD being defined as the distance between the rear interface of the first plug and the front interface of the second plug. In case (b), two plugs are far apart from each other in generation 0 and the initial distance between them is increased to 10 mm. In case (c), two plugs are positioned in different generations initially and ΔD is measured as its projection on the direction of the channel length in generation 0. ΔD is easily measured in this way and has a one-to-one correspondence to the real positions of the plugs. In the case shown in figure 5.5(c), the initial distance between plugs is ΔD=13.4 mm.

Since we are interested in the flow rate variation with the generation number, the flow patterns to be discussed below is strictly for the time period when both plugs, or the daughters of them, move in the straight channels, i.e. neither of them is passing the bifurcation. When the plugs are initially close to each other as in case (a), their daughters mostly move in the same generation, as shown in figure 5.6(a). This implies the distance between two plugs in the straight channel is always smaller than one generation and is noted by $\Delta G = 0$ later in this chapter. When the initial distance between plugs increases in case (b), the two successive plugs will always move in two successive generations in the network, as shown in figure 5.6(b) and noted as $\Delta G = 1$. With the initial state (c), there remains a separation of one generation between daughters of two initial plugs as they advance, as shown in figure 5.6(c) and noted as $\Delta G = 2$.

In the two-plug experiments shown in figure 5.6, the flow rates of the first plug $Q_{\mathrm{t}}^{[1]}$ and the second plug $Q_{\mathrm{t}}^{[2]}$ are plotted versus the generation number in figure 5.7, where the superscripts '[1]' and '[2]' denote the first and the second plug. As the plugs advance in the network, the flow rates increase in all the three cases. There is little difference between the curves for $Q_{\mathrm{t}}^{[1]}$ and $Q_{\mathrm{t}}^{[2]}$, which indicates that the air between the two plugs is not compressed and thus $Q_{\mathrm{t}}^{[1]} = Q_{\mathrm{t}}^{[2]}$ holds during the flow evolution. Although the driving pressure is kept the same and the lengths of the plugs do not change much, the total flow rate displays a clear dependence on the initial distance between the two plugs. As the plugs get further apart, a higher flow rate is observed. This is to be explained in the next subsection using the empirical relation.

5.2.2 Applicability of the empirical relation

Linearity of (5.1) provides the possibility to analyze the dynamics when two plugs are injected successively into the network. Like for two resistors mounted in series, the relation between the driving pressure and the volumetric flow rate can be written as:

$$P_{\mathrm{dr}} = R_i^{[1]} L_i^{[1]} Q_{\mathrm{t}}^{[1]} + R_j^{[2]} L_j^{[2]} Q_{\mathrm{t}}^{[2]}, \tag{5.2}$$
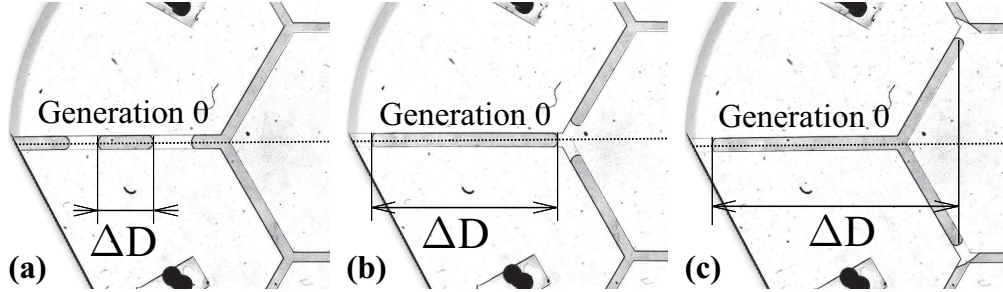
Figure 5.5: Initial states of the two-plug experiments. The difference is marked by the distance between the rear interface of the first plug and the front interface of the second plug. This distance ΔD increases as (a), (b) and (c). The dashed line denotes the direction of the channel length in generation 0 and the horizontal solid segment with arrows measures ΔD.
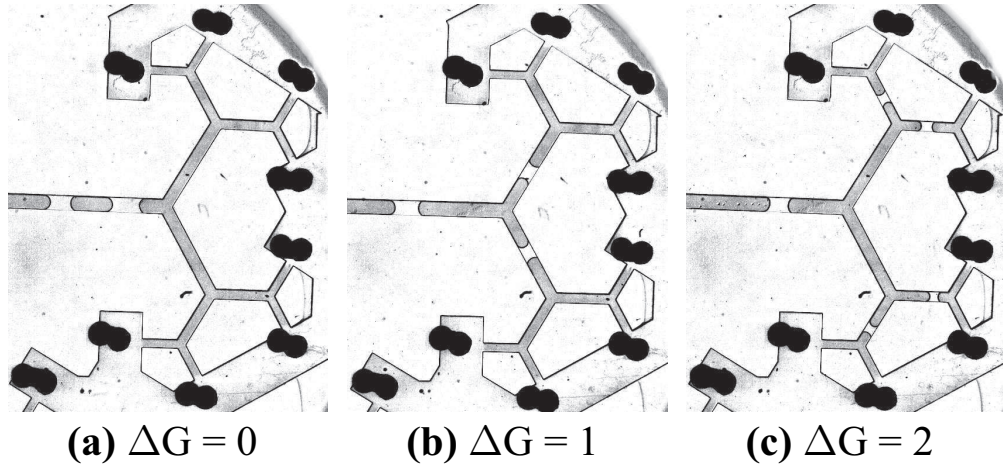
Figure 5.6: Flow patterns involving two plugs with different initial distances. Half of the network is shown for clarify. As the initial distance increases, the two plugs are (a) close together, (b) moving in two successive generations and (c) advancing with a separation of one generation.
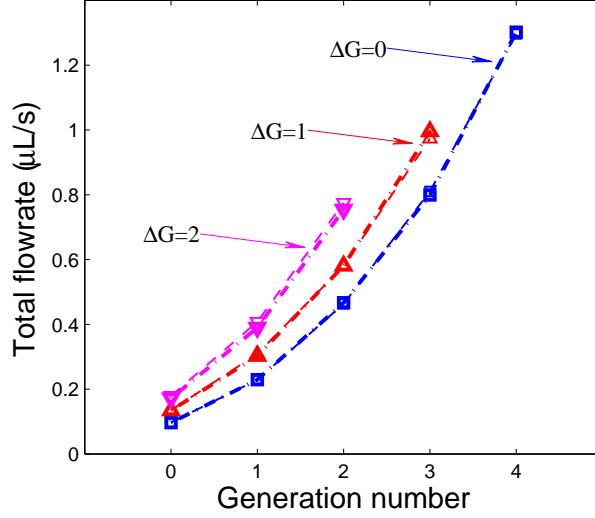
Figure 5.7: Flow rates measurements at $P_{\mathrm{dr}} = 500\,\mathrm{Pa}$ when two plugs flow in the same generation $\Delta G = 0$ ($\square$), in two successive generations $\Delta G = 1$ ($\triangle$) and with a separation of one generation $\Delta G = 2$ ($\triangledown$). Symbols connected by dash-dotted lines denote flow rates measured based on the motion of the second plug injected, $Q_{\mathrm{t}}^{[2]}$, and dashed lines connect the points based on the motion of the first plug $Q_{\mathrm{t}}^{[1]}$. Data is plotted according to the position, generation number i, of the daughters of the second plug.

where the subscripts 'i' and 'j' indicate the position of the plugs in the network by the corresponding generation numbers.

With the measurements in figure 5.7, we can note $Q_{\mathrm{t}}^{[1]} = Q_{\mathrm{t}}^{[2]}$ for (5.2), which can be then expressed as:

$$P_{\mathrm{dr}} = (R_i^{[1]} L_i^{[1]} + R_j^{[2]} L_j^{[2]}) Q_{\mathrm{t}}, \tag{5.3}$$

in which Q_{t} is the total flow rate in the network. Using the values of R_i determined above and the initial lengths of two plugs, $R_i L_i$ for both plugs can be computed. Flow rates for a two-plug train predicted by (5.3) are compared to the experimental findings in figure 5.8, where data points are plotted according to the position, generation number i, of the daughters of the second plug. Open symbols connected by dash-dotted lines denote experimental data and closed ones connected by solid lines are values derived from the linear law. Satisfactory agreement is obtained for all the three experimental conditions, indicating that the linear description of the flow in the network is applicable for a two-plug train and gives a good approximation.

Equation (5.3) can also be used for understanding the flow dependence on the initial distance between plugs. As two plugs are treated as resistors mounted in series, the total resistance becomes $(R_i^{[1]} L_i^{[1]} + R_j^{[2]} L_j^{[2]})$ that relates to the positions of both plugs in the network. For the
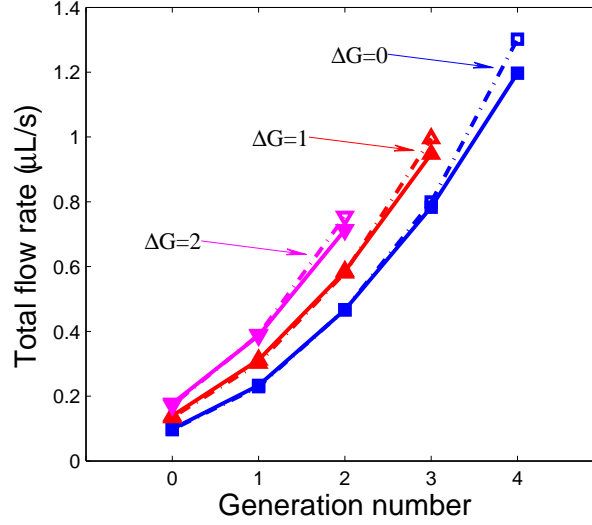
Figure 5.8: Predicted and measured flow rates in two-plug experiments ($P_{dr} = 500$ Pa) when they flow in the same generation $\Delta G = 0$ ($\square$), in two successive generations $\Delta G = 1$ ($\triangle$) and with a separation of one generation $\Delta G = 2$ ($\triangledown$). Open symbols connected by dash-dotted lines denote experimental data and closed ones connected by solid lines are values derived from the linear relation. Flow rate data is plotted according to the position, generation number i, of the daughters of the second plug.

second plug positioned in a given generation j, the position of the first plug depends on their initial distance ΔD. As ΔD increases, the first plug that flows downstream becomes further apart from the second plug, which results in a smaller resistance due to the first plug since $R_i L_i$ decreases with the generation number as shown in figure 5.3. In this way, $(R_i^{[1]} L_i^{[1]} + R_j^{[2]} L_j^{[2]})$ also decreases, which yields a higher flow rate in the network.

5.3   A train of plugs injected

Experiments are run with three successive plugs injected into the network, as shown in figure 5.9, where the four daughters of the first plug has reached generation 2 while the last plug, the third one injected, is advancing in generation 0. The driving pressure and the plug lengths are kept to be 500 Pa and 1.8 ± 0.2 mm, respectively. During the experiment, plugs are always moving in three successive generations and the flow remains in the state of $\Delta G = 1$ between plugs. The total flow rate in the network is plotted and compared to the two-plug experiment with $\Delta G = 1$ in figure 5.10, where the data for three-plug experiment is shown by $\bigcirc$ while $\triangle$ represents the same data as in figure 5.8. Again the solid line connects data derived from the empirical relation and this prediction is also in good agreement with the experimental data (dash-dotted line with open symbols).
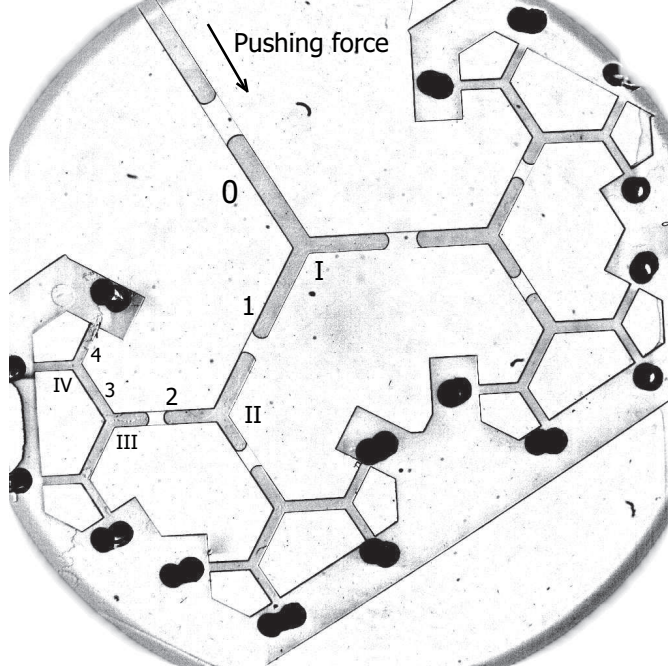
Figure 5.9: The $\mathcal{N}$ network with three plugs injected successively. The four plugs in generation 2 are daughters of the first plug injected, two daughters of the second plug are moving in generation 1 and the last plug is in generation 0.

When the last plug moves in generation 0, there is little difference between the flow rates in two-plug and three-plug situations. In the three plug case, the total resistance $(R_0L_0 + R_1L_1 + R_2L_2)$ almost equals the resistance of a two plug train $(R_0L_0 + R_1L_1)$, since $R_2L_2 << R_0L_0 + R_1L_1$ as shown in figure 5.3. This implies that the resistance to flow can be dominated by the upstream plugs in the network. However, the flow rate difference between two situations increases as plugs advance and the biggest difference in the figure appears when the last plug reaches generation 2. At this stage, the difference between $\sum R_iL_i$ for three-plug $(R_2L_2 + R_3L_3 + R_4L_4)$ and two-plug $(R_2L_2 + R_3L_3)$ becomes visible, since R_4L_4 is comparable to R_3L_3 and R_2L_2.

For many plugs of initially same sizes injected continuously into the network, the relation between P_{dr} and Q_{t} is $P_{\mathrm{dr}} = Q_{\mathrm{t}} \sum R_iL_i$, where $\sum R_iL_i$ sums up the resistances due to different plugs. As plugs enter the network with the initial state of case (b), the overall resistance $\sum R_iL_i$ increases before the daughters of the first plug reach the network exits, resulting a decrease in the flow rate. Noticing that the variation of $\sum R_iL_i$ is due to the addition of contribution from the most downstream plug in the train, $\sum R_iL_i$ increases slowly after the downstream plug arrives at generation 2, since the resistances in the following generations are much smaller than those in generation 0 and 1. As a result, the total flow rate will not bear strong decrease once plugs arrive at generation 2, since $\sum R_iL_i$ can be then essentially fixed by the upstream plugs. After
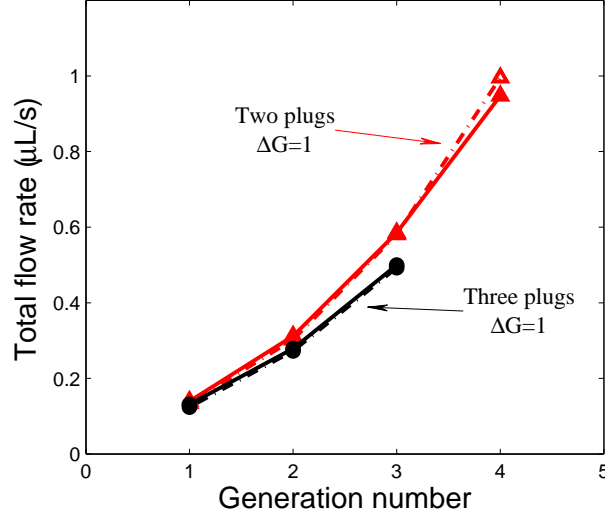
Figure 5.10: Comparison of flow rate evolutions in two-plug ($\triangle$) and three-plug ($\bigcirc$) experiments at the driving pressure $P_{\mathrm{dr}} = 500$ Pa. Flow rate data is plotted according to the position, generation number i, of the daughters of the last plug. Open symbols connected by dash-dotted lines denote experimental data and closed ones connected by solid lines are values derived from the linear relation.

the first daughters reach the exits, $\sum R_i L_i$ becomes constant and the flow rate does not vary any more.

5.4   Summary and discussion

Besides the long range interaction between daughter plugs at different positions in the network, interactions between successively injected plugs, in the $\mathcal{N}$ network, are also found to exist. The total flow rate in the network can be controlled by varying the initial distance between plugs.

An empirical relation is derived in the investigation of the pressure–flow rate evolution of the two-phase flow and found to account for the resistance associated with daughters of a single plug. Given the initial condition of the experiments, e.g. driving pressure and plug lengths, this relation quantitatively predicts the flow rates in the presence of a train of successive plugs.

The flow rate in the network can be essentially fixed by the upstream plug when the succeeding plugs are separated by a large distance. The downstream plug perceives a flow rate forcing, even if the actual driving condition is through pressure. This is confirmed by the flow rates in the two-plug and three-plug experiments in figure 5.10. Although a third plug is transported through the network, the flow rate in the three-plug experiment increases comparably to the two-plug case.

Furthermore, if there are plugs injected continuously into generation 0, the flow rate in the network can remain constant since the total resistance is dominated by the upstream plugs. This provides a possible method, from the application point of view, to control the flow rate after the injection of liquid at the network entrance. At the same time, the fact that downstream plugs are exposed to a flow rate driving may modify the flow distribution in a branching tree through inter-generation effects, which are expected to feed back on the flow everywhere in the tree.

Chapter 6

Airway reopening through cascades

6.1 Introduction

In contrast to a few plugs present in the network discussed in the previous chapters, the catastrophic cascades involving trains of liquid plugs will be studied here. Since the airway is coated by a thin film of liquid (Grotberg, 1994), the formation of liquid plugs, due to the elasticity of the airways (Heil *et al.*, 2008) or hydrodynamic instability (Macklem *et al.*, 1970), may cause the closure of the airways. In these situations, the subsequent reopening of airways becomes fatal in sustaining the functions of the lung. Gaver *et al.* (1990) have studied the reopening process by penetrating a finger of air into a flexible tube filled with liquid and later research about the reopening in flexible tubes has also been presented (Majumdar *et al.*, 2001; Hazel & Heil, 2003; Grotberg & Jensen, 2004).

However, considering plug ruptures in rigid tubes, previous work has been focused on the single plug movement in a straight channel (Huh *et al.*, 2007; Fujioka *et al.*, 2008) or its division at one bifurcation (Cassidy *et al.*, 2001*b*; Ody *et al.*, 2007). Using a microfluidic model to mimic the structure of the airway, we here show that the flow of several plugs is unstable at very high pressures in the branching network, which is unlike the flow studied in Chapters 4 and 5. This can happen through cascades of plug ruptures and flow acceleration brought by the cascades. At the same time, the dynamics of plug ruptures can play a dominant role in the distribution of the flow and in how much of the tree is reopened.

In our binary network, cascades occur along particular paths, which display dependence on the initial distribution of the plugs and the conditions just before the cascades. Plug divisions at bifurcations introduce further complexity to the system since the short daughters after the division are easy to rupture, which can thus lead to an accelerated cascade. The experiments in the network with branching channels capture the main attributes of multiphase fluid transport in the airway and show that the cascades may happen through the movement of the liquid plugs

Figure 6.1: Experimental setup for the investigation of cascades of liquid plugs at high driving pressures in the straight channel. A syringe filled with liquid is connected to one inlet of the entrance and can be pushed by a pump so that the liquid inside goes into the channel. The other inlet of the entrance is connected to a water column which provides a constant pressure that pushes the air. The exit of the channel is open, which fixes the boundary condition to atmospheric pressure P_{atm}. The flow inside the channel is recorded with the high speed camera through a microscope and image sequences are stored in the computer.

(Majumdar *et al.*, 2003) in the absence of the elastic effects of the wall. In this chapter, we describe some preliminary study of the reopening.

6.2   Experimental setups

The experimental setups for flows in the straight channel are similar to those illustrated in figure 3.5 in Section 3.2. The difference exists in the configuration for pushing the air as shown in figure 6.1. The air is pushed at a constant pressure which is provided by a water column, whose pressure is known as $\Delta P = \rho_w g \Delta h$ where ρ_w is the density of water, g is the acceleration due to gravity and Δh is the height difference between two surfaces of water. Δh can be controlled by positioning the water containers at different heights. For simplicity, ΔP will be noted as P_{dr} later in this chapter, which is the pressure driving the plugs.
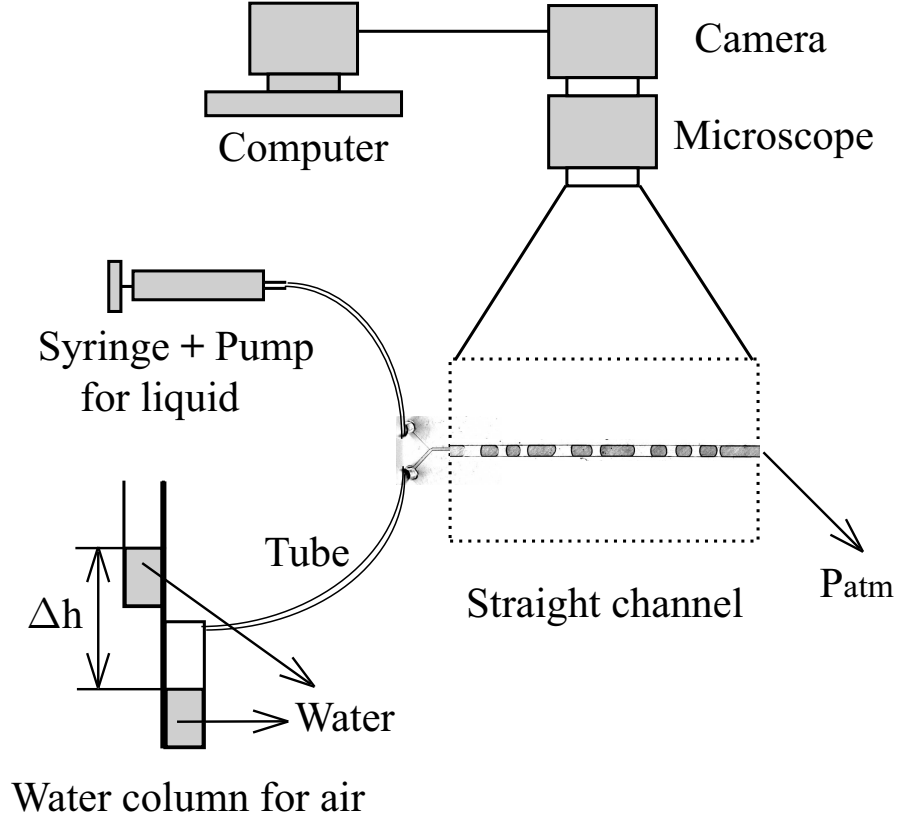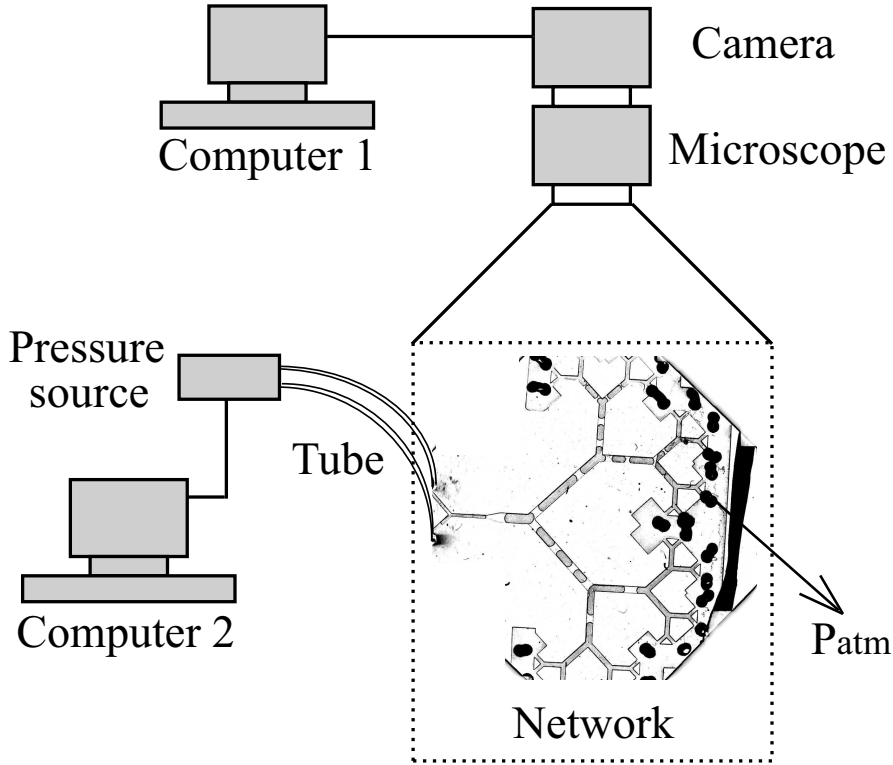
Figure 6.2: Experimental setup for the investigation of cascades of liquid plugs at high driving pressures in the network. The inlets for the air and the liquid are both connected to the pressure source controlled by computer 2. At the end of the network, thirty-two holes are punched to fix the exit pressure to P_{atm}. The flow evolution is recorded with the high speed camera through a microscope and image sequences are stored in computer 1.

Experiments are conducted in a straight channel with width $w = 700$ μm and height $h = 50$ μm. The entrance to the straight channel consists of a Y-junction with two inlets and the exit is open to the atmosphere pressure. A train of several PFD plugs is created inside the straight channel and pushed at a very high pressure by the water column through the entrance.

For the experiments in the network, the setups are illustrated in figure 6.2, where the inlets for the air and the liquid are connected to two channels of the pressure source (FLUIGENT, MFCS-8C) controlled by computer 2. Therefore, the air and liquid can be pushed at different pressures at the same time since the machine provides different pressures through different channels.

The network here has six generations and the bifurcation half-angle $\alpha = 45°$, which yields a right angle between two daughter branches in the same generation. All the branches are 50 μm high. The first generation is 720 μm wide and the widths of the channels in successive generations decrease at the ratio 0.83. Several plugs are injected into the network at the beginning of the experiments, which is done by alternatively pushing liquid and air. Plugs are created automatically by the pressure source once the input program is fixed. The plug creation can

(a) $t = 0$ s

(b) $t = 0.12$ s

(c) $t = 0.18$ s

(d) $t = 0.27$ s

(e) $t = 0.35$ s

Figure 6.3: Images of a cascade of plug ruptures in the straight channel. (a) Ten plugs of variable sizes are created inside the chann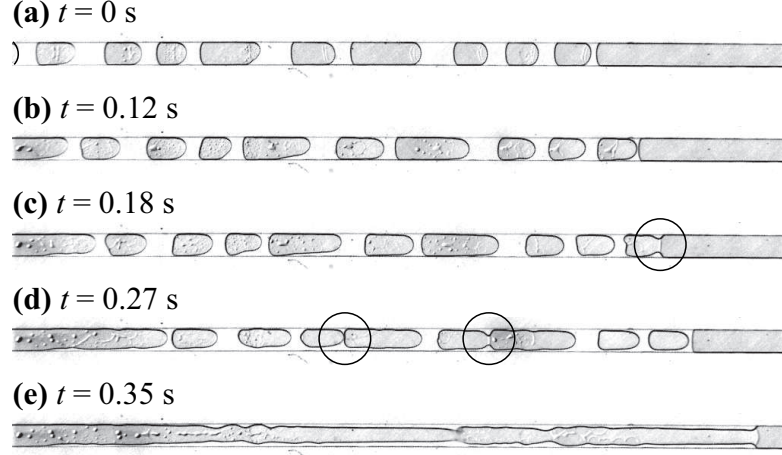el at the beginning of the experiment. (b) Plugs are pushed at $P_{dr} = 4800$ Pa toward the end of the channel. All of them are deformed and small droplets are left behind. (c) The first plug breaks on the right of the channel, marked by the circle. (d) Two plugs break nearby at the same time, both marked by circles. (e) All plugs have ruptured in the cascade and the channel is opened to air.

be repeated in different experimental runs and the initial distribution of plugs in the network can be kept over experiments. The air then pushes the plugs to advance. The flow evolution is recorded by the camera through the microscope.

6.3   Cascades of plug ruptures

6.3.1   Cascades in a straight channel

We first simplify the problem and start from the investigation of plug ruptures in a straight channel, which the network consists of. For the experiment in figure 6.3, ten plugs of variable sizes are created inside the straight channel and their initial distribution is shown in image (a). The plugs are pushed at $P_{dr} = 4800$ Pa and the motion is recorded at 1000 images per second by the camera. As the plugs advance in the channel, their interfaces deform and many small droplets are left behind the plugs due to the high velocity, which is observed in figure 6.3(b). Later on, the plug that is first injected breaks at $t = 0.18$ s, which is pointed out by the circle in image (c). After the first plug ruptures, all the other plugs accelerate and later two of them break at the same time, marked by two circles in image (d). 0.35 s after the start of the experiment, all the plugs have broken and the entire channel is opened.

The positions of the plugs on the central line of the channel are plotted as a function of time in the spatio-temporal diagram in figure 6.4. The bright parts represent the plugs and the horizontal distance between the two borders of the bright area equals the length of the plug at
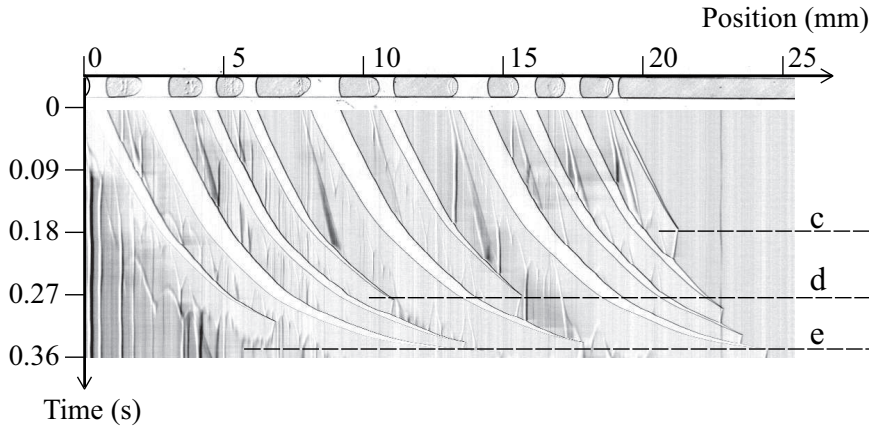
Figure 6.4: Spatio-temporal diagram of the cascade involving ten plugs in the straight channel. The spatial evolution of position is tracked along the central line of the channel so the horizontal distance between the two borders of the bright part equals the length of the plug. The slope of the bright border represents the velocity of the plug interface. The dashed lines labeled by letters c, d and e denote the events corresponding to figure 6.3(c), (d) and (e), respectively.

that moment. In this way, the plug rupture can be recognized by the merging of two borders. Along the y-axis, the times when important events have happened can be known. Moreover, the slope of the curves denotes the velocity of the plug.

When the pressure is applied between the entrance and the exit of the channel, all plugs advance at the same velocity and accelerate very slowly due to the decrease of resistance resulted from the liquid deposited on the channel walls, which in turn shortens the moving plugs. (The liquid deposition is important here since the plugs move at high velocities.) The time-averaged value of the plug velocity is $V = 12$ mm/s before $t = 0.18$ s, when the first plug breaks. This plug rupture strongly decreases the total resistance to flow because of the disappearance of two air-liquid interfaces and a large velocity increase is observed when the slopes of all the curves are strongly modified between $t = 0.18$ s and 0.27 s. The time-averaged velocity of the plug increases to 26 mm/s, which is more than double of the velocity before the first plug rupture. A second strong increase in velocity is found when other two plugs break at $t = 0.27$ s. Therefore, the rupture of plugs strongly decreases the total resistance to flow and results in sudden increase of velocity. Meanwhile, the velocity increase leads to more liquid being deposited on the wall, which shortens the liquid plugs and introduces the rupture of more plugs. We refer to the successive ruptures of liquid plugs occurring in a short time as a cascade.

6.3.2   Observations in a network

Now we come back to our network to see how the cascade evolves when there are more than one straight channels. A series of images taken during a typical experiment is displayed in figure 6.5,

Table 6.1: Variables in the fit of $N_p = m_1 t^* + m_2$

P_{dr}	m_1	m_2	t^*
2000	12	3	t
3500	34	-5	$t^{1/3}$
5000	32.5	0.3	$t^{1/3}$

where seven plugs are initially injected into the network and then pushed at $P_{\mathrm{dr}} = 3500$ Pa. With the initial distribution of plugs in image (a), the first cascade happens along one path in the network, labeled in green in image (b), while plugs in other parts of the network continue to move and divide. The cascade in the network involves a few generations of straight channels and the opening of an upstream branch may result in the opening of downstream daughter branches. For example four exits originating from the same upstream branch are opened in the first cascade. The second cascade in the network happens far from the first one and also opens four exits, as shown in image (c). As the flow develops, cascades happen in the network and open more exits. The paths, where the first cascades occur, are labeled in figure 6.5(d) and the earlier cascade involves opening of more exits than the later ones.

Since the plug ruptures are closely related to the happening of cascade, we sum up the number of broken plugs in different experiments under three driving conditions in figure 6.6. Each symbol corresponds to the averaged number in several experimental realizations under the same pressure. Although the same amount of plugs break at three different pressures, it takes more time to break the plugs when the driving pressure is low, 2000 Pa. When $P_{\mathrm{dr}} = 2000$ Pa, the cumulative number of broken plugs increases as a linear function of the time, as presented by the solid line through $\diamond$. However, this number increases more rapidly when the driving pressure is higher, 3500 and 5000 Pa. In these cases, the relation between the total number of broken plugs N_p and time t can be expressed as $N_p = m_1 t^* + m_2$, where t^* represents t for $P_{\mathrm{dr}} = 2000$ Pa and $t^{1/3}$ for $P_{\mathrm{dr}} = 3500$ and 5000 Pa, and m_1 and m_2 are constant for a given experimental condition. Therefore, the evolution of plug numbers can be summarized by a simple fit $N_p = m_1 t^* + m_2$ and the variables for three driving conditions are given in table 6.1 for obtaining the solid curves in figure 6.6.

There also exists a power law fit for the cumulative number of opened exits N_e in the network under three driving conditions as shown in figure 6.7, where each symbol gives the averaged number over a few experiments and the solid curve represents the fit of $N_e = n_1 t^* + n_2$. While $t^* = t$ for low driving pressure 2000 Pa and $t^{1/3}$ for the other two pressures, n_1 and n_2 are given

(a) $t = 0$ s

(b) $t = 0.16$ s

(c) $t = 0.26$ s

(d) $t = 1$ s
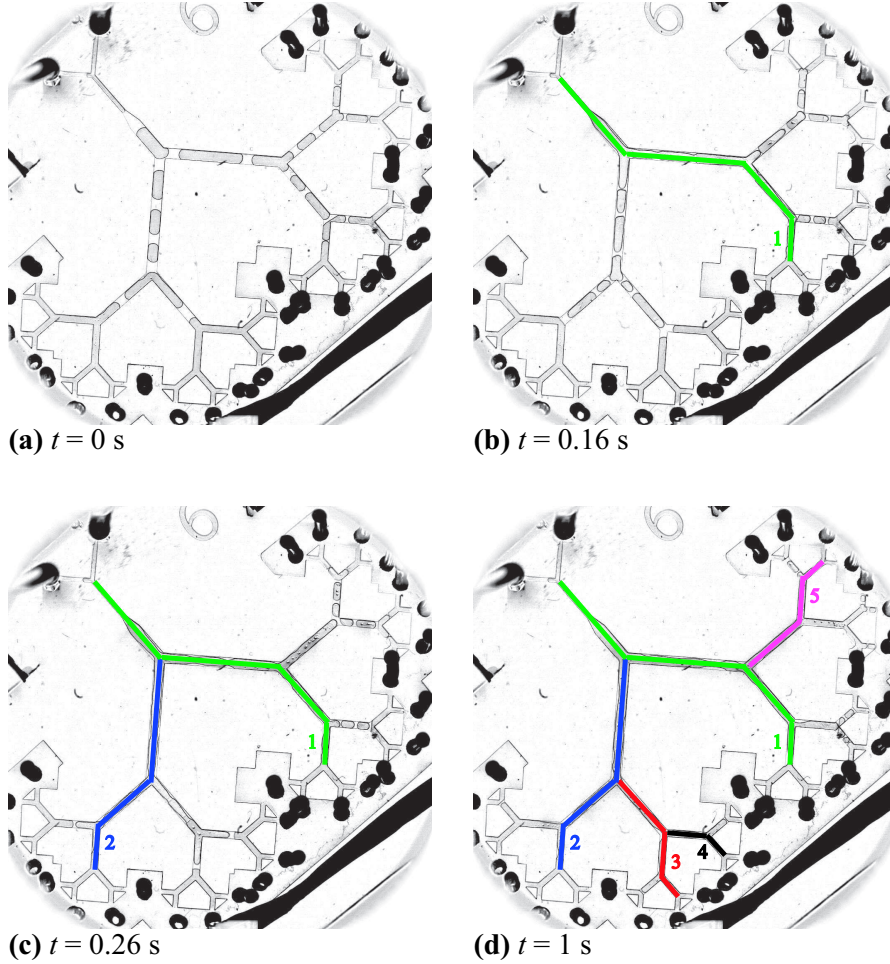
Figure 6.5: Images of cascades in the branching network when the driving pressure is 3500 Pa. (a) The initial distribution of plugs in the network when seven plugs are injected. (b) Some plugs break at the same time and the first cascade happens along the path in green at $t = 0.16$ s. The green path is opened by air flow and the number besides it denotes the order of the cascade. (c) A second cascade happens through plug ruptures, as labeled in blue. Far from the green path, this blue path lies in another half of the network. (d) In the end, many paths are opened through cascades, of which the first five are labeled in color.
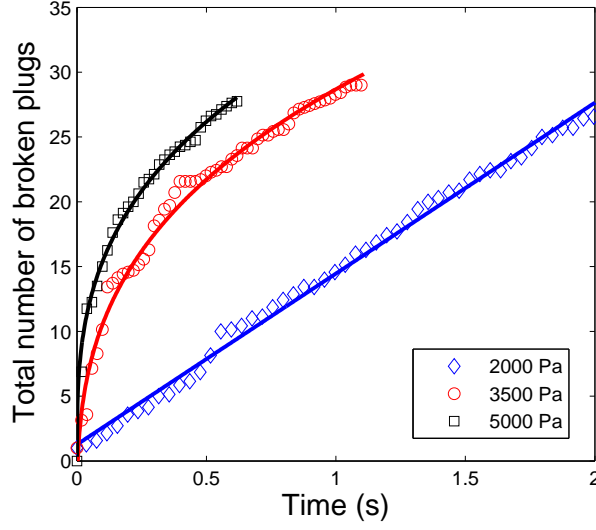
Figure 6.6: Cumulative number of broken plugs in experiments under different driving pressures. Each symbol represents the averaged value over several experiments and the solid line the fit by the expression $N_p = m_1 t^* + m_2$.

Table 6.2: Variables in the fit of $N_e = n_1 t^* + n_2$

P_{dr}	n_1	n_2	t^*
2000	1.4	0.45	t
3500	16	0	$t^{1/3}$
5000	11	0.8	$t^{1/3}$

in table 6.2. The transition of t^* implies a transition between two statistic states in the process of network reopening, where the driving pressure can play an important role.

Since the plug division at the bifurcation introduces more daughters in the system, the number of broken plugs does not always reveal the number of opened exits. The differences in the total number of opened exits are found in figure 6.7 for different driving conditions. It is interesting that the largest number of opened exits appears when $P_{\mathrm{dr}} = 3500 \ Pa$, which is neither the highest nor the lowest pressure. It can be explained basically by the competition between plug advancements and their ruptures. The opening of an exit requires ruptures of all the plugs in the path connecting that exit to the network entrance, which implies all plugs in that path have to break before reaching the exit. When the driving pressure is too high, the plugs advance very fast and their divisions introduce many daughters. Although some daughters break in cascades, some others reach the exits before the happening of possible cascades, which makes those exits not opened. However, when the driving pressure is low, fewer cascades can happen although
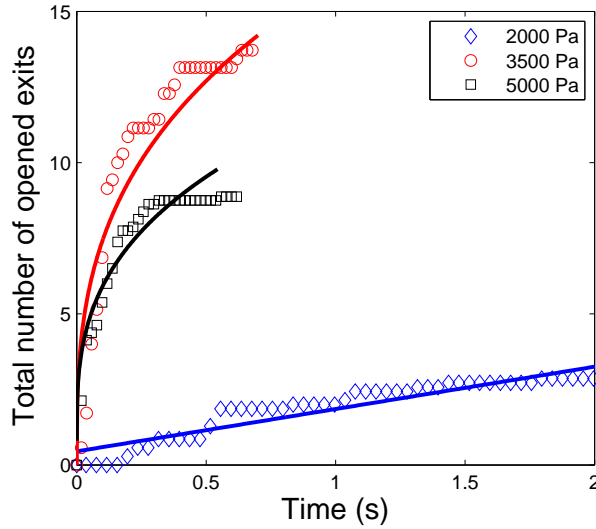
Figure 6.7: Cumulative number of opened exits in the network, out of thirty-two exits in total. Each symbol represents the averaged value over several experiments at the same driving condition and the solid line the fit by the expression $N_e = n_1 t^* + n_2$.

plugs have not reached the exits. This is consistent with the findings in figure 6.6, where the rapid increase of broken plugs is associated with cascades in which many plugs break at the same time, $P_{dr} = 5000$ Pa. When the plugs break separately, $P_{dr} = 2000$ Pa, their accumulative number increases slowly.

6.4 Summary

Microfluidic models are employed to investigate the airway reopening through cascades of plug ruptures. A succession of plug ruptures within a short time interval is observed in both the straight channel and the network when the flow is pushed at high pressures. This cascade of plug ruptures involves the opening of the straight channel or a few exits in the network.

When several plugs are pushed at a high pressure in the straight channel, each of them deposits a thin film of liquid on the wall, which shortens the plug itself and thus decreases the total resistance to flow. Therefore, the plugs have a small acceleration while advancing. This acceleration can increase rapidly because of the breaking of a single plug, which decreases the total resistance in a very short time by the sudden disappearance of air-liquid interfaces. However, the velocity increase increases the liquid deposition on the walls and makes the plugs even shorter and easier to break. All these effects lead to the cascade of plug ruptures and the opening of the entire channel thereafter.

Different from the case in a straight channel, plugs in the network do not move at the same velocity even at the beginning of the experiment. Due to the geometry variation of the channels in different generations, the plug velocity also varies depending on the generation number and this introduces a new mechanics to the cascade. Meanwhile, the division of plugs at bifurcations results in more daughter plugs in the system and the plugs normally get shorter after the division. The presence of short plugs speeds up the happening of cascade in a particular path, which will influence the spatial distribution of other cascades in the network. As there can be a few cascades happening in a row in the network, several exits can be opened in the end of the experiment.

The cumulative number of broken plugs in the network increases as a function of time: Linearly with t at a low driving pressure and with $t^{1/3}$ at medium and high pressures. These fits are also obtained for cumulative number of opened exits under different driving conditions. Furthermore, a medium pressure opens more exits than low and high pressures in the experiments.

Chapter 7

Conclusions

The transport of liquid plugs in binary branching networks is studied experimentally with microfluidic techniques to make networks of generations of connected channels. Liquid plugs are pushed through networks of either narrowing channels or widening channels at different driving conditions. The flow behavior is explained by plug interactions that can be demonstrated in a fundamental element of the network, which consists of three adjacent bifurcations.

At constant pressure driving, daughter plugs divide in synchrony at bifurcations since they are all subjected to the same pressure difference and there are no interactions between plugs. This results in liquid penetration to the same bifurcation level in all the branches of the network. However, plugs cannot reach the exits of a narrowing tree with infinite generations, since the threshold will become larger than the driving pressure somewhere in the tree. Conversely, a widening tree can be invaded by plugs as long as the initial plug passes the first bifurcation.

Differences are found when the plug is pushed at constant flow rate, when the flow is influenced by the interactions of the pressure drop required for viscocapillary motion of plugs in straight channels and the threshold pressure necessary for plugs to pass the bifurcation. For the network with narrowing channels, plugs always reach the exits although daughters may advance in distinct steps. In contrast, networks with sufficient generations of widening channels can never be fully penetrated by liquid plugs pushed at constant flow rate.

By focusing on the relation between the pressure and total flow rate in the network, we have derived an empirical linear relation from the data of a single plug experiment. The resistance associated with the presence of daughters of one plug in the network is found to provide good predictions for the flow involving a train of plugs pushed at constant pressure. This simple relation can be used when the flow evolves in the given range and it can be improved by taking into account more aspects in the future investigations, such as the effects brought by liquid deposition on the wall after the first plug and the variations in the lengths of daughter plugs due to uneven divisions. Generalizing these results can lead to better understanding of related

biological issues, for example, the reopening process of airways occluded by discrete plugs, about which some preliminary results were also presented at the end of this thesis.

The prediction of two-phase flow based on plug interactions in the fundamental element connects the understanding of one plug motion in a straight tube (or at a bifurcation) and the global evolution of two-phase flows in complex geometries. The flow containing one plug is well studied through the comparison of interactions in the fundamental element and this element can serve as a building block for many network topologies. Therefore, this element and the accompanying approach can be adapted in the studies about two-phase flows in other networks where the flow can be inferred from an analysis of interactions in one element and between different elements.

Although the results in the thesis have been obtained in networks of rectangular channels within two-dimensional considerations, the physical analysis in the fundamental element is applicable for channels with other cross-sectional areas and in three-dimensional realizations. The narrowing network captures the main characteristic structure of the lung and thus a similar fundamental element is expected to exist in pulmonary airways, while the value of the threshold in that element depends on the local geometry of bronchioles. Since the sizes of actual airways vary even in the same generation, the resulting variation of thresholds can introduce further interactions between daughter plugs in different branches. This can account for the different paths taken by liquid boluses in medical treatments of drug delivery into the airway.

This study provides insight for the process of liquid instillation into the lung, the airway occlusion in pathological situations, fluid transport in porous media, and many technological applications. Future work may include interactions between daughters of different plugs in the element of three connected bifurcations under different drivings, since the presence of multiple plugs in a train can strongly modify the interactions between them. It is also interesting to have trains of plugs pushed at constant flow rate, where the introduction of later plugs may improve the liquid transport at some conditions by changing the local resistance in one branch and yielding the opening of more branches. Furthermore, liquid plugs exposed to oscillating pressure differences can better model the flow that takes place in the lung during breath cycles.

Bibliography

AJAEV, V. S. & HOMSY, G. M. 2006 Modeling shapes and dymics of confined bubbles. *Annu. Rev. Fluid Mech.* **38** (1), 277–307.

ALENCAR, A. M., AROLD, S. P., BULDYREV, S. V., MAJUMDAR, A., STAMENOVIC, D., STANLEY, H. E. & SUKI, B. 2002 Dynamic instabilities in the inflating lung. *Nature* **417**, 809 – 811.

ALENCAR, A. M., BULDYREV, S. V., MAJUMDAR, A., STANLEY, H. E. & SUKI, B. 2001 Avalanche dynamics of crackle sound in the lung. *Phys. Rev. Lett.* **87** (8), 088101.

AUSSILLOUS, P. & QUÉRÉ, D. 2000 Quick deposition of a fluid on the wall of a tube. *Phys. Fluids* **12** (10), 2367–2371.

BAROUD, C. N., TSIKATA, S. & HEIL, M. 2006 The propagation of low-viscosity fingers into fluid-filled branching networks. *J. Fluid Mech.* **546**, 285–294.

BEREJNOV, V., DJILALI, N. & SINTON, D. 2008 Lab-on-chip methodologies for the study of transport in porous media: energy applications. *Lab Chip* **8** (5), 689–693.

BERTRAM, C. D. & GAVER, D. P. 2005 Biofluid mechanics of the pulmonary system. *Ann. Biomed. Eng.* **33**, 1681–1688.

BHATTACHARYA, S., DATTA, A., BERG, J. M. & GANGOPADHYAY, S. 2005 Studies on surface wettability of poly(dimethyl) siloxane (pdms) and glass under oxygen-plasma treatment and correlation with bond strength. *J. Microelectromech. Syst.* **14** (3), 590 – 597.

BICO, J. & QUÉRÉ, D. 2001 Falling slugs. *J. Colloid Interface Sci.* **243** (1), 262 – 264.

BOYLE, R. 1662 *New Experiments Physico-Mechanical, Touching the Air: Whereunto is Added A Defence of the Authors Explication of the Experiments, Against the Obiections of Franciscus Linus and Thomas Hobbes*. Oxford: H. Hall.

BRETHERTON, F. P. 1961 The motion of long bubbles in tubes. *J. Fluid Mech.* **10** (02), 166–188.

BULL, J. L., TREDICI, S., KOMORI, E., BRANT, D. O., GROTBERG, J. B. & HIRSCHL, R. B. 2004 Distribution dynamics of perfluorocarbon delivery to the lungs: an intact rabbit model. *J. Appl. Physiol.* **96** (5), 1633–1642.

CALDERON, A. J., FOWLKES, J. B. & BULL, J. L. 2005 Bubble splitting in bifurcating tubes: a model study of cardiovascular gas emboli transport. *J. Appl. Physiol.* **99** (2), 479–487.

CASSIDY, K. J., BULL, J. L., GLUCKSBERG, M. R., DAWSON, C. A., HAWORTH, S. T., HIRSCHL, R., GAVRIELY, N. & GROTBERG, J. B. 2001*a* A rat lung model of instilled liquid transport in the pulmonary airways. *J. Appl. Physiol.* **90** (5), 1955–1967.

CASSIDY, K. J., GAVRIELY, N. & GROTBERG, J. B. 2001*b* Liquid plug flow in straight and bifurcating tubes. *J. Biomech. Eng.* **123** (6), 580–589.

CHAKRABORTY, D., GORKIN, R., MADOU, M., KULINSKY, L. & CHAKRABORTY, S. 2009 Capillary filling in centrifugally actuated microfluidic devices with dynamically evolving contact line motion. *J. Appl. Phys.* **105** (8), 084904.

CHANDLER, R., KOPLIK, J., LERMAN, K. & WILLEMSEN, J. F. 1982 Capillary displacement and percolation in porous media. *J. Fluid Mech.* **119**, 249–267.

CHEN, J. M., CHEN, C.-Y. & LIU, C.-H. 2008 Pressure barrier in an axisymmetric capillary microchannel with sudden expansion. *Jpn. J. Appl. Phys.* **47** (3), 1683 – 1689.

CHO, H., KIM, H.-Y., KANG, J. Y. & KIM, T. S. 2007 How the capillary burst microvalve works. *J. Colloid Interface Sci.* **306** (2), 379 – 385.

CORSON, F. 2010 Fluctuations and redundancy in optimal transport networks. *Phys. Rev. Lett.* **104** (4), 048703.

COURBIN, L., DENIEUL, E., DRESSAIRE, E., ROPER, M., AJDARI, A. & STONE, H. A. 2007 Imbibition by polygonal spreading on microdecorated surfaces. *Nat. Mater.* **6** (9), 661–664.

DARHUBER, A. A. & TROIAN, S. M. 2005 Principles of microfluidic actuation by modulation of surface stresses. *Annu. Rev. Fluid Mech.* **37** (1), 425–455.

DELAMARCHE, E., BERNARD, A., SCHMID, H., BIETSCH, A., MICHEL, B. & BIEBUYCK, H. 1998 Microfluidic networks for chemical patterning of substrates: Design and application to bioassays. *J. Am. Chem. Soc.* **120**, 500–508.

DUFFY, D. C., GILLIS, H. L., LIN, J., SHEPPARD, N. F. & KELLOGG, G. J. 1999 Microfabricated centrifugal microfluidic systems: Characterization and multiple enzymatic assays. *Anal. Chem.* **71**, 4669 – 4678.

DUSSAN, E. B. 1979 On the spreading of liquids on solid surfaces: Static and dynamic contact lines. *Annu. Rev. Fluid Mech.* **11** (1), 371–400.

EDDINGS, M. A., JOHNSON, M. A. & GALE, B. K. 2008 Determining the optimal pdms-pdms bonding technique for microfluidic devices. *J. Micromech. Microeng.* **18** (6), 067001.

ENGL, W., ROCHE, M., COLIN, A., PANIZZA, P. & AJDARI, A. 2005 Droplet traffic at a simple junction at low capillary numbers. *Phys. Rev. Lett.* **95** (20), 208304.

ENGLE, W. A. & THE COMMITTEE ON FETUS & NEWBORN 2008 Surfactant-replacement therapy for respiratory distress in the preterm and term neonate. *Pediatrics* **121** (2), 419–432.

VAN ERTBRUGGEN, C., HIRSCH, C. & PAIVA, M. 2005 Anatomically based three-dimensional model of airways to simulate flow and particle transport using computational fluid dynamics. *J. Appl. Physiol.* **98** (3), 970–980.

ESPINOSA, F. F. & KAMM, R. D. 1999 Bolus dispersal through the lungs in surfactant replacement therapy. *J. Appl. Physiol.* **86** (1), 391–410.

FUERSTMAN, M. J., LAI, A., THURLOW, M. E., SHEVKOPLYAS, S. S., STONE, H. A. & WHITESIDES, G. M. 2007 The pressure drop along rectangular microchannels containing bubbles. *Lab Chip* **7** (11), 1479–1489.

FUJIOKA, H. & GROTBERG, J. B. 2004 Steady propagation of a liquid plug in a two-dimensional channel. *J. Biomech. Eng.* **126** (5), 567–577.

FUJIOKA, H., TAKAYAMA, S. & GROTBERG, J. B. 2008 Unsteady propagation of a liquid plug in a liquid-lined straight tube. *Phys. Fluids* **20** (6), 062104.

GARSTECKI, P., FISCHBACH, M. A. & WHITESIDES, G. M. 2005 Design for mixing using bubbles in branched microfluidic channels. *Appl. Phys. Lett.* **86** (24), 244108.

GAVER, D. P., R., SAMSEL, R. W. & SOLWAY, J. 1990 Effects of surface tension and viscosity on airway reopening. *J. Appl. Physiol.* **69** (1), 74–85.

GERRITSEN, M. G. & DURLOFSKY, L. J. 2005 Modeling fluid flow in oil reservoirs. *Annu. Rev. Fluid Mech.* **37** (1), 211–238.

GERVAIS, L. & DELAMARCHE, E. 2009 Toward one-step point-of-care immunodiagnostics using capillary-driven microfluidics and pdms substrates. *Lab Chip* **9** (23), 3330–3337.

GROTBERG, J. B. 1994 Pulmonary flow and transport phenomena. *Annu. Rev. Fluid Mech.* **26**, 529–571.

GROTBERG, J. B. 2001 Respiratory fluid mechanics and transport processes. *Annu. Rev. Biomed. Eng.* **3** (1), 421–457.

GROTBERG, J. B. & JENSEN, O. E. 2004 Biofluid mechanics in flexible tubes. *Annu. Rev. Fluid Mech.* **36** (1), 121–147.

GUNTHER, A. & JENSEN, K. F. 2006 Multiphase microfluidics: from flow characteristics to chemical and materials synthesis. *Lab Chip* **6** (12), 1487–1503.

GUNTHER, A., JHUNJHUNWALA, M., THALMANN, M., SCHMIDT, M. A. & JENSEN, K. F. 2005 Micromixing of miscible liquids in segmented gas-liquid flow. *Langmuir* **21**, 1547–1555.

HALPERN, D. & GROTBERG, J. B. 1992 Fluid-elastic instabilities of liquid-lined flexible tubes. *J. Fluid Mech.* **244**, 615–632.

HALPERN, D., JENSEN, O. E. & GROTBERG, J. B. 1998 A theoretical study of surfactant and liquid delivery into the lung. *J. Appl. Physiol.* **85** (1), 333–352.

HAZEL, A. L. & HEIL, M. 2003 Three-dimensional airway reopening: the steady propagation of a semi-infinite bubble into a buckled elastic tube. *J. Fluid Mech.* **478**, 47–70.

HEIL, M., HAZEL, A. L. & SMITH, J. A. 2008 The mechanics of airway closure. *Respir. Physiol. Neurobiol.* **163** (1-3), 214 – 221, respiratory Biomechanics.

HODGES, S. R., JENSEN, O. E. & RALLISON, J. M. 2004 The motion of a viscous drop through a cylindrical tube. *J. Fluid Mech.* **501**, 279–301.

HOFFMAN, R. L. 1975 A study of the advancing interface. i. interface shape in liquid–gas systems. *J. Colloid Interface Sci.* **50** (2), 228 – 241.

HOWELL, P. D., WATERS, S. L. & GROTBERG, J. B. 2000 The propagation of a liquid bolus along a liquid-lined flexible tube. *J. Fluid Mech.* **406**, 309–335.

HSU, S. H., STROHL, K. P., HAXHIU, M. A. & JAMIESON, A. M. 1996 Role of viscoelasticity in the tube model of airway reopening. ii. non-newtonian gels and airway simulation. *J. Appl. Physiol.* **80** (5), 1649–1659.

HUH, D., FUJIOKA, H., TUNG, Y.-C., FUTAI, N., PAINE, R., GROTBERG, J. B. & TAKAYAMA, S. 2007 Acoustically detectable cellular-level lung injury induced by fluid mechanical stresses in microfluidic airway systems. *Proc. Natl. Acad. Sci. U.S.A.* **104** (48), 18886–18891.

JANSONS, K. M. 1985 Moving contact lines on a two-dimensional rough surface. *J. Fluid Mech.* **154**, 1–28.

JOUSSE, F., FARR, R., LINK, D. R., FUERSTMAN, M. J. & GARSTECKI, P. 2006 Bifurcation of droplet flows within capillaries. *Phys. Rev. E* **74** (3), 036311.

KATIFORI, E., SZÖLLŐSI, G. J. & MAGNASCO, M. O. 2010 Damage and fluctuations induce loops in optimal transport networks. *Phys. Rev. Lett.* **104** (4), 048704.

KITAOKA, H., TAKAKI, R. & SUKI, B. 1999 A three-dimensional model of the human airway tree. *J. Appl. Physiol.* **87** (6), 2207–2217.

KLEINSTREUER, C., ZHANG, Z., LI, Z., ROBERTS, W. L. & ROJAS, C. 2008 A new methodology for targeting drug-aerosols in the human respiratory system. *Int. J. Heat Mass Transfer* **51** (23-24), 5578 – 5589, biomedical-Related Special Issue.

KOPLIK, J. 1982 Creeping flow in two-dimensional networks. *J. Fluid Mech.* **119**, 219–247.

KRISHNAMURTHY, S. & PELES, Y. 2007 Gas-liquid two-phase flow across a bank of micropillars. *Phys. Fluids* **19** (4), 043302.

LACROIX-FRALISH, A., TEMPLETON, E. J., SALIN, E. D. & SKINNER, C. D. 2009 A rapid prototyping technique for valves and filters in centrifugal microfluidic devices. *Lab Chip* **9** (21), 3151–3154.

LAI, S., WANG, S., LUO, J., LEE, L. J., YANG, S.-T. & MADOU, M. J. 2004 Design of a compact disk-like microfluidic platform for enzyme-linked immunosorbent assay. *Anal. Chem.* **76**, 1832 – 1837.

LARSON, R., SCRIVEN, L. & DAVIS, H. 1981 Percolation theory of two phase flow in porous media. *Chem. Eng. Sci.* **36** (1), 57 – 73.

LEACH, C. L., GREENSPAN, J. S., RUBENSTEIN, S. D., SHAFFER, T. H., WOLFSON, M. R., JACKSON, J. C., DELEMOS, R. & FUHRMAN, B. P. 1996 Partial liquid ventilation with perflubron in premature infants with severe respiratory distress syndrome. *N. Engl. J. Med.* **335** (11), 761.

LEE, J. N., PARK, C. & WHITESIDES, G. M. 2003 Solvent compatibility of poly(dimethylsiloxane)-based microfluidic devices. *Anal. Chem.* **75**, 6544–6554.

LENORMAND, R. 1990 Liquids in porous media. *J. Phys.: Condens. Matter* **2** (S), SA79–SA88.

LENORMAND, R. & ZARCONE, C. 1985 Invasion percolation in an etched network: Measurement of a fractal dimension. *Phys. Rev. Lett.* **54** (20), 2226–2229.

LENORMAND, R., ZARCONE, C. & SARR, A. 1983 Mechanisms of the displacement of one fluid by another in a network of capillary ducts. *J. Fluid Mech.* **135**, 337–353.

LINK, D. R., ANNA, S. L., WEITZ, D. A. & STONE, H. A. 2004 Geometrically mediated breakup of drops in microfluidic devices. *Phys. Rev. Lett.* **92** (5), 054503.

LOW, H. T., CHEW, Y. T. & ZHOU, C. W. 1997 Pulmonary airway reopening: Effects of non-newtonian fluid viscosity. *J. Biomech. Eng.* **119** (3), 298–308.

MACKLEM, P. T., PROCTOR, D. F. & HOGG, J. C. 1970 The stability of peripheral airways. *Respir. Physiol.* **8**, 191–203.

MADOU, M., ZOVAL, J., JIA, G., KIDO, H., KIM, J. & KIM, N. 2006 Lab on a cd. *Annu. Rev. Biomed. Eng.* **8** (1), 601–628.

MAJUMDAR, A., ALENCAR, A. M., BULDYREV, S. V., HANTOS, Z., STANLEY, H. E. & SUKI, B. 2001 Characterization of the branching structure of the lung from "macroscopic" pressure-volume measurements. *Phys. Rev. Lett.* **87** (5), 058102.

MAJUMDAR, A., ALENCAR, A. M., BULDYREV, S. V., HANTOS, Z., STANLEY, H. E. & SUKI, B. 2003 Fluid transport in branched structures with temporary closures: A model for quasistatic lung inflation. *Phys. Rev. E* **67** (3), 031912.

MAN, P. F., MASTRANGELO, C. H., BURNS, M. A. & BURKE, D. T. 1998 Microfabricated capillarity-driven stop valve and sample injector. *Proc. 11th Annu. Int. Workshop Micro Electro Mechanical Systems, Heidelberg, Germany* pp. 45–50.

MCCULLOH, K. A., SPERRY, J. S. & ADLER, F. R. 2003 Water transport in plants obeys murray's law. *Nature* **421**, 939 – 942.

MURRAY, C. D. 1926 The physiological principle of minimum work. i. the vascular system and the cost of blood volume. *Proc. Natl. Acad. Sci. U.S.A.* **12** (3), 207–214.

NEWMAN, M. E. J. 2003 The structure and function of complex networks. *SIAM Review* **45** (2), 167–256.

ODY, C. P. 2007 Dynamique de microbouchons dans un canal et une bifurcation. Phd thesis, Ecole Polytechnique.

ODY, C. P., BAROUD, C. N. & DE LANGRE, E. 2007 Transport of wetting liquid plugs in bifurcating microfluidic channels. *J. Colloid Interface Sci.* **308** (1), 231 – 238.

OLBRICHT, W. L. 1996 Pore-scale prototypes of multiphase flow in porous media. *Annu. Rev. Fluid Mech.* **28** (1), 187–213.

OTIS, D. R., J., JOHNSON, M., PEDLEY, T. J. & KAMM, R. D. 1993 Role of pulmonary surfactant in airway closure: a computational study. *J. Appl. Physiol.* **75** (3), 1323–1333.

PEHLIVAN, K., HASSAN, I. & VAILLANCOURT, M. 2006 Experimental study on two-phase flow and pressure drop in millimeter-size channels. *Appl. Therm. Eng.* **26** (14-15), 1506 – 1514.

QUAKE, S. R. & SCHERER, A. 2000 From micro- to nanofabrication with soft materials. *Science* **290** (5496), 1536–1540.

SAHIMI, M. 1993 Flow phenomena in rocks: from continuum models to fractals, percolation, cellular automata, and simulated annealing. *Rev. Mod. Phys.* **65** (4), 1393–1534.

SCHINDLER, M. & AJDARI, A. 2008 Droplet traffic in microfluidic networks: A simple model for understanding and designing. *Phys. Rev. Lett.* **100** (4), 044501.

SONG, H., TICE, J. D. & ISMAGILOV, R. F. 2003 A microfluidic system for controlling reaction networks in time. *Angew. Chem. Int. Ed.* **42**, 768–772.

STEPHAN, K., PITTET, P., RENAUD, L., KLEIMANN, P., MORIN, P., OUAINI, N. & FER-RIGNO, R. 2007 Fast prototyping using a dry film photoresist: microfabrication of soft-lithography masters for microfluidic structures. *J. Micromech. Microeng.* **17** (10), N69–N74.

STONE, H. A., STROOCK, A. D. & AJDARI, A. 2004 Engineering flows in small devices. *Annu. Rev. Fluid Mech.* **36** (1), 381–411.

STROGATZ, S. H. 2001 Exploring complex networks. *Nature* **410**, 268 – 276.

TANNER, L. H. 1979 The spreading of silicone oil drops on horizontal surfaces. *J. Phys. D: Appl. Phys.* **12** (9), 1473–1484.

VIG, A. L., HALDRUP, K., ENEVOLDSEN, N., THILSTED, A. H., ERIKSEN, J., KRISTENSEN, A., FEIDENHANS'L, R. & NIELSEN, M. M. 2009 Windowless microfluidic platform based on capillary burst valves for high intensity x-ray measurements. *Rev. Sci. Instrum.* **80** (11), 115114.

WEIBEL, E. R. 1984 *The pathway for oxygen*. Cambridge, MA., USA: Harvard U. press.

WEST, G. B., BROWN, J. H. & ENQUIST, B. J. 1999 A general model for the structure and allometry of plant vascular systems. *Nature* **400**, 664–667.

WEST, J. B. 1999 The original presentation of boyle's law. *J. Appl. Physiol.* **87** (4), 1543–1545.

WONG, H., RADKE, C. J. & MORRIS, S. 1995 The motion of long bubbles in polygonal capillaries. part 2. drag, fluid pressure and fluid flow. *J. Fluid Mech.* **292**, 95–110.

XIA, Y. & WHITESIDES, G. M. 1998 Soft lithography. *Angew. Chem. Int. Ed.* **37** (5), 550–575.

XU, L., DAVIES, S., SCHOFIELD, A. B. & WEITZ, D. A. 2008 Dynamics of drying in 3d porous media. *Phys. Rev. Lett.* **101** (9), 094502.

YAMADA, M., DOI, S., MAENAKA, H., YASUDA, M. & SEKI, M. 2008 Hydrodynamic control of droplet division in bifurcating microchannel and its application to particle synthesis. *J. Colloid Interface Sci.* **321** (2), 401 – 407.

ZIMMERMANN, M., SCHMID, H., HUNZIKER, P. & DELAMARCHE, E. 2007 Capillary pumps for autonomous capillary systems. *Lab Chip* **7** (1), 119–125.

Appendix A

Variation of the capillary pressure difference

A.1 Plug at the bifurcation

During the plug passage of a bifurcation, its front and rear interfaces will deform because of the geometry restrict of the channel. At a given plug position, there exits a capillary pressure difference between the front and rear interfaces of the plug. This pressure difference P_{cap} is a function of the plug position and can be expressed as:

$$P_{\mathrm{cap}} = P_{\mathrm{r}} - P_{\mathrm{a}} = \frac{\gamma}{r_{\mathrm{r}}} - \frac{\gamma}{r_{\mathrm{a}}}, \tag{A.1}$$

where P_{r} and P_{a} are the capillary pressure at the rear and the front interfaces, r_{r} and r_{a} are the radii of curvature of the interfaces, and γ is the surface tension of the liquid. It is also defined that P_{r} and P_{a} are positive when the plug deforms as shown in figure A.1. Therefore, a positive P_{cap} resists the driving pressure and tends to push the plug backwards while a negative P_{cap} pulls the plug forwards.

There are three stages during the passage, in which (A.1) can be derived quantitatively and differently. These expressions will be discussed in this section.

When the plug arrives at a bifurcation, its front interface is deformed because of the change of channel geometry before the rear interface is affected by the bifurcation, as shown in figure A.1. The curvature of the front interface decreases as the plug advances and, as a result, P_{cap} increases (r_{a} increases).

Here, it is assumed that the plug is long enough, so the rear interface enters the bifurcation after the front one touches the facing tip. Therefore, P_{r} remains the same as $2\gamma \cos\theta/w_i$ in stage one and only P_{a} varies. With all the parameters noted in figure A.1, r_{a} can be obtained as (A.2) in triangle $S_1 S_2 S_3$ based on the law of sines. In figure A.1, α is the bifurcation half-angle, d the distance of the front interface from the horizontal channel, w_i the width of the horizontal channel
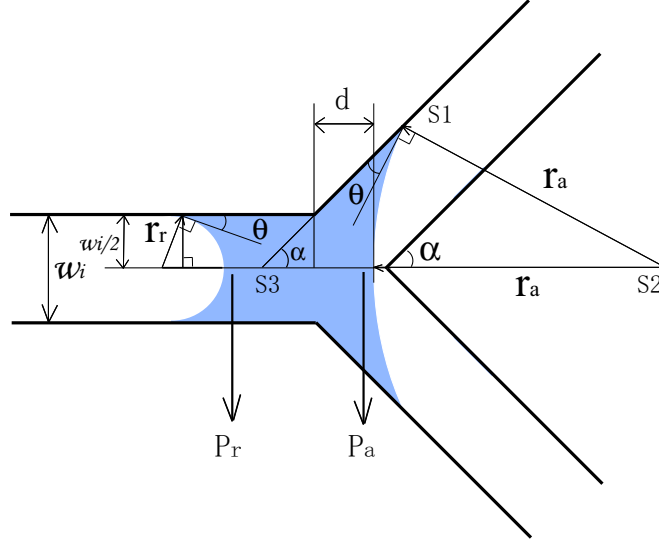
Figure A.1: Plug at the bifurcation: Stage one, the front interface enters the bifurcation. The radius of curvature $r_a > r_r$ and r_a increases while the plug is advancing. Parameters for calculation: P_r (P_a) capillary pressure at the rear (front) interface, r_r (r_a) the radius of curvature, θ the contact angle of liquid on the channel wall, α the bifurcation half-angle, w_i the channel width, d the distance of the front interface from the horizontal channel, S_1, S_2, S_3 three vertexes of the triangle $S_1S_2S_3$.

and θ the contact angle of liquid on the channel wall. Thus the capillary pressure difference P_{cap} is expressed as (A.3).

$$\frac{r_a}{\sin\alpha} = \frac{r_a + d + (w_i/2)\cot\alpha}{\sin(\theta + 90°)}$$

$$\Rightarrow r_a = \frac{\sin\alpha((w_i/2)\cot\alpha + d)}{\sin(\theta + 90°) - \sin\alpha} \tag{A.2}$$

$$P_{cap} = P_r - P_a = \frac{\gamma}{r_r} - \frac{\gamma}{r_a}$$

$$= \frac{2\gamma\cos\theta}{w_i} - \frac{\gamma(\sin(\theta + 90°) - \sin\alpha)}{\sin\alpha((w_i/2)\cot\alpha + d)} \tag{A.3}$$

There exists a maximum value of r_a, $r_{a,max}$, reached just before the front interface touches the facing tip, as shown in figure A.2. At this point, P_{cap} also reaches its maximum value $P_{cap,max}$, which is called the threshold pressure at the bifurcation, P_{thr}. Similarly, $r_{a,max}$ can be calculated (A.4) in triangle $S_1S_2S_3$ in figure A.2, where w_{i+1} is the width of the branching channel and $w_{i+1} = \rho w_i$ in our network topology. P_{thr} is thus obtained from (A.5).

$$\frac{r_{a,max}}{\sin(\theta + 90°)} = \frac{r_{a,max} - w_{i+1}/\cos\theta}{\sin\alpha}$$

$$\Rightarrow r_{a,max} = \frac{w_{i+1}}{\cos\theta - \sin\alpha} \tag{A.4}$$
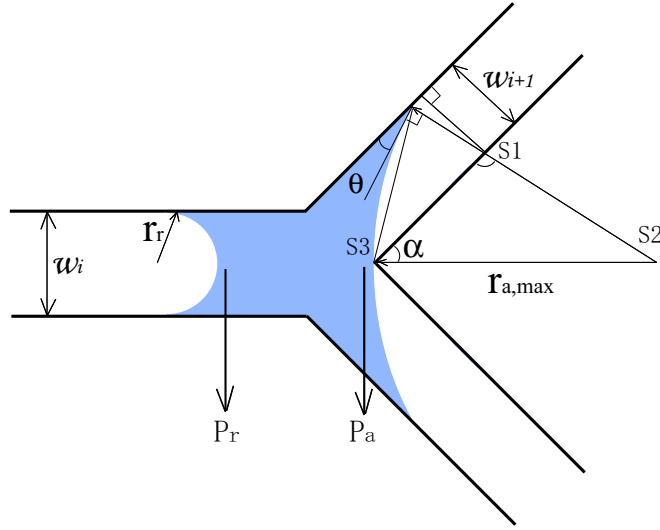
Figure A.2: The front interface is touching the facing tip. r_a and P_{cap} reach their maximum values respectively.

$$P_{thr} = P_{cap,max} = \frac{\gamma}{r_r} - \frac{\gamma}{r_{a,max}}$$
$$= \frac{2\gamma \cos \theta}{w_i} - \frac{\gamma(\cos \theta - \sin \alpha)}{w_{i+1}} \tag{A.5}$$

Given (A.1, A.3 and A.5), the capillary pressure difference is positive and increases until it reaches the threshold value. In stage one of the plug passage, P_{cap} resists the driving force that pushes the plug to advance.

After its front interface touches the facing tip, the plug starts to divide into two daughters as shown in figure A.3. In stage two, the capillary pressure at the new front interface equals $2\gamma \cos \theta / w_{i+1}$, where w_{i+1} is the width of the branching channel. P_{cap} remains constant before the rear interface enters the bifurcation.

$$P_{cap} = P_r - P_a$$
$$= \frac{2\gamma \cos \theta}{w_i} - \frac{2\gamma \cos \theta}{w_{i+1}} \tag{A.6}$$

During stage two, the sign of P_{cap} depends on the width of two successive channels in the network, which is associated with the geometry ratio ρ. If $\rho > 1$, P_{cap} is positive in (A.6) and it continues resisting the driving force. Conversely, if $\rho < 1$, P_{cap} becomes negative and this capillary pressure difference helps the plug advance through the bifurcation.

When the rear interface enters the bifurcation as shown in figure A.4, r_r starts to increase as the plug advances. By knowing the width of the horizontal channel w_i and the distance of the rear interface to it d_e, r_r is also known by (A.7), based on the law of sines in triangle $S_1 S_2 S_3$.
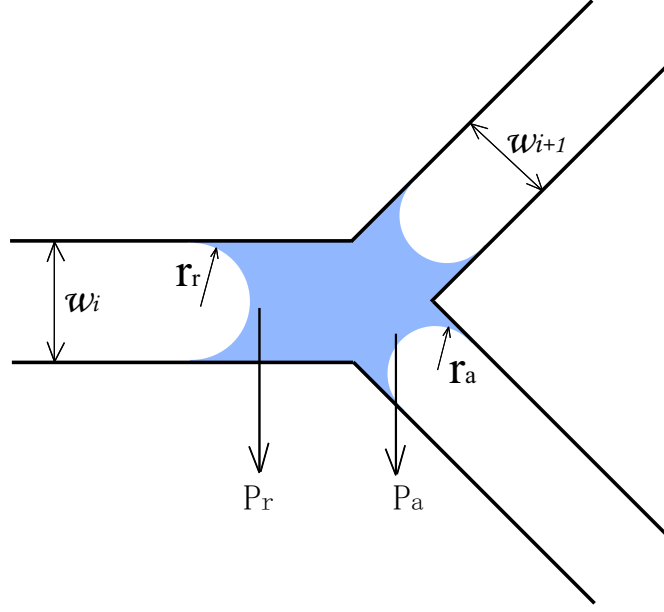
Figure A.3: Plug at the bifurcation: Stage two, from the front interface touching the facing tip to the rear interface entering the bifurcation, r_a decreases rapidly and then remains constant.

Therefore, P_cap can be expressed as (A.8). In the network with $\rho < 1$, P_cap pulls the plug to divide in this stage since $r_\mathrm{r} > r_\mathrm{a}$. However, in a network with $\rho > 1$, P_cap may still resist the driving force since r_r can be smaller than r_a.

$$\frac{r_\mathrm{r}}{\sin \alpha} = \frac{d_e - r_\mathrm{r} + (w_i/2)\cot \alpha}{\sin(90° - \theta)}$$
$$\Rightarrow r_\mathrm{r} = \frac{\sin \alpha((w_i/2)\cot \alpha + d_e)}{\sin(90° - \theta) + \sin \alpha} \tag{A.7}$$

$$P_\mathrm{cap} = P_\mathrm{r} - P_\mathrm{a}$$
$$= \frac{\gamma(\sin(90° - \theta) + \sin \alpha)}{\sin \alpha((w_i/2)\cot \alpha + d_e)} - \frac{2\gamma \cos \theta}{w_{i+1}} \tag{A.8}$$

Although the above formulas are derived by assuming the interface shapes as shown in the figures, there can always be a sign for the radius of curvature. In this way, the shape and curvature of the interface are automatically taken into account by changing the value of the contact angle. This indicates that the equations are applicable for any other situations, i.e. liquid with other contact angle. A positive direction of the capillary pressure is already defined in (A.1), which yields that a positive P_cap resists the plug motion.
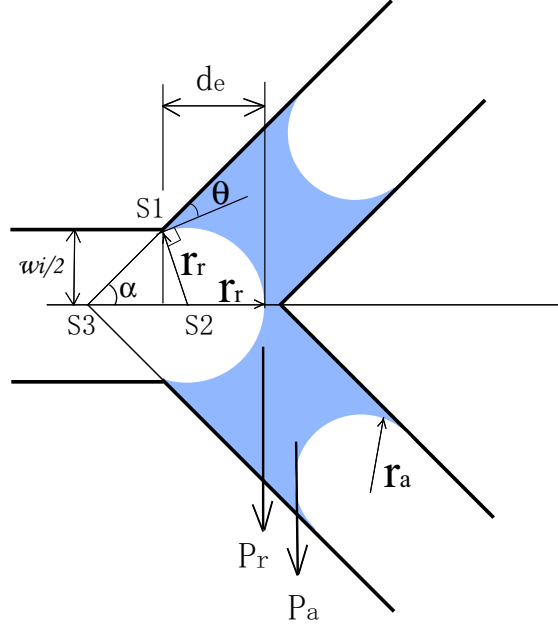
Figure A.4: Plug at the bifurcation: Stage three, the rear interface enters the bifurcation. r_r increases as the plug is advancing. d_e denotes the distance of the rear interface from the horizontal channel.

A.2 Plug at the exit

At the end of the last generation, the exit of the network has the same shape of a bifurcation but without daughter channels. When the plug reaches the exit (figure A.5), its front interface deforms in a similar way as the plug at the bifurcation. The capillary pressure difference $P_\mathrm{cap,e}$ across the plug can be derived from (A.3) by replacing r_a, d and w_i by R_exit, d_E and w_e respectively, where w_e is the channel width in the last generation of the network. The new expressions are given in (A.9, A.10).

$$R_\mathrm{exit} = \frac{\sin\alpha((w_e/2)\cot\alpha + d_E)}{\sin(\theta + 90°) - \sin\alpha} \tag{A.9}$$

$$\begin{aligned} P_\mathrm{cap,e} = P_\mathrm{r} - P_\mathrm{a} &= \frac{2\gamma\cos\theta}{w_e} - \frac{\gamma}{R_\mathrm{exit}} \\ &= \frac{2\gamma\cos\theta}{w_e} - \frac{\gamma(\sin(\theta + 90°) - \sin\alpha)}{\sin\alpha((w_e/2)\cot\alpha + d_E)} \end{aligned} \tag{A.10}$$

$P_\mathrm{cap,e}$ keeps increasing until the rear interface also enters the exit as shown in figure A.6, after which point the radius of curvature of the rear interface r_exit starts to increase. r_exit can be obtained by replacing r_r and w_i in (A.7) by r_exit and w_e respectively and written as (A.11). $P_\mathrm{cap,e}$ is then written as (A.12). During stage two at the exit, the radii of curvature at both
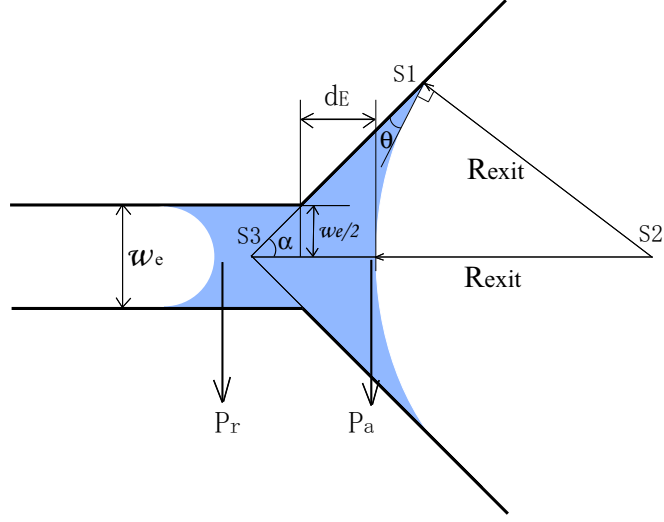
Figure A.5: Plug at the exit: Stage one, the front interface enters the exit. w_e is the channel width in the last generation of the network.

interfaces increase as the plug advances and $P_{\text{cap,e}}$ remains positive. If the plug is pushed to advance, the rear interface will catch up with the front one, at which moment the plug breaks and $P_{\text{cap,e}}$ cancels.

$$r_{\text{exit}} = \frac{\sin\alpha((w_e/2)\cot\alpha + d_e)}{\sin(\theta + 90°) - \sin\alpha} \tag{A.11}$$

$$
\begin{aligned}
P_{\text{cap,e}} = P_{\text{r}} - P_{\text{a}} &= \frac{\gamma}{r_{\text{exit}}} - \frac{\gamma}{R_{\text{exit}}} \\
&= \frac{\gamma(\sin(90° - \theta) + \sin\alpha)}{\sin\alpha((w_e/2)\cot\alpha + d_e)} - \frac{\gamma(\sin(\theta + 90°) - \sin\alpha)}{\sin\alpha((w_e/2)\cot\alpha + d_E)}
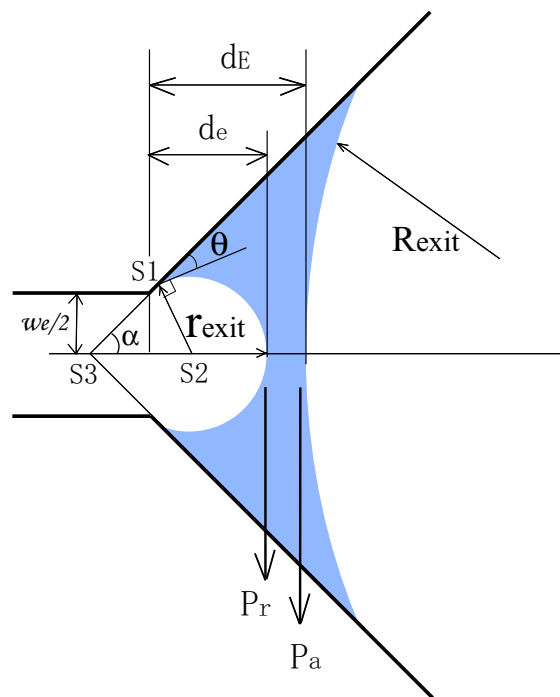\end{aligned}
\tag{A.12}
$$

Figure A.6: Plug at the exit: Stage two, the rear interface also enters the exit. Both r_{exit} and R_{exit} increase as the interfaces advance.

Appendix B

Estimation of the air compressibility

The ideal gas law, which origin dates back to Boyle's law first published in 1662 (Boyle, 1662; West, 1999), is employed here to estimate the effects of the air compressibility.

This law is an equation of state and generally applicable for real gas under standard temperature and pressure. At constant temperature, the equation of state for a given mass of gas can be written as:

$$PV = const., \tag{B.1}$$

where P and V are the pressure and volume of the gas. When the gas is compressed by $(-\Delta V)$, its pressure can increase to $(P + \Delta P)$ and the first order expansion of Taylor series gives

$$P\Delta V = V\Delta P, \tag{B.2}$$

when ΔV and ΔP are very small compared to V and P.

To be used in the flow rate driving case, (B.2) can be rewritten as:

$$PQ\Delta t = V\Delta P, \tag{B.3}$$

in which P is the air pressure pushing the plug, Q is the driving flow rate and Δt is the time of pressure and volume variation. The pressure variation ΔP needed to preserve the flow rate is determined by the network geometry and experimental conditions. P, Q and ΔP in (B.3) are all fixed for a single experiment. The time Δt for compression is proportional to the initial air volume V. The decrease in V results in a decrease in Δt, meaning more rapid variation in pressure and ultimately better preservation of the flow rate.

The air between the liquid in the syringe and the plug in the network consists of three parts: the air in the syringe, in the microtube connecting the syringe to the network and in the network inlet. The syringe is capable for 100 μL and we normally fill half of it, which gives the air volume

in the syringe to be $V_S = 50$ μL. The tube is 20 cm long with an inner diameter of 0.56 mm, so the volume is $V_T \approx 49$ μL. The network inlet measures 240 μm $\times$50 μm $\times$2 mm in width, height and length, respectively, and the air in the inlet is $V_I = 0.024$ μL. The total volume of air makes $V = V_S + V_T + V_I = 99$ μL.

When the syringe and most of the microtube are filled with water as stated in Section 3.2, the air volume is $V' = V_T' + V_I = 2.46 + 0.024 = 2.5$ μL with V_T' for 1 cm of air left in the tube. A comparison of V' to V reveals that the decrease of air volume reduces the compressibility effects by $(V - V')/V = 98\%$.

At the same time, the channel length L_i equals 16 mm in generation 0 and decreases as $L_i = 7 \times 0.6^{i-1}$ mm starting from generation 1. The total volume of the network is $V_N = \sum (whLN)_i = 2.2$ μL, where w, h, L and N denote the channel width, height, length and the number of branches in generation i. Since $V_N \approx 2\%V$, a small variation ΔV (or $Q\Delta t$) of V can be very big compared to the volume of the network and Δt can be comparable to the time to fill the whole network, i.e. the time for a complete experiment. However, noticing that $V' \approx V_N$, the air left in the latter case is necessary to conduct the experiment and the side effects are satisfactorily limited.

Appendix C

Publications and proceedings

Local interactions and the global organization of a two-phase flow in a branching tree.

SONG, Y., MANNEVILLE, P. & BAROUD, C. N.

Physical Review Letters (2010), **105**, 134501.

The air-liquid flow in a microfluidic airway tree.

SONG, Y., BAUDOIN, M., MANNEVILLE, P. & BAROUD, C. N.

Medical Engineering & Physics (2010), published online.

Penetration pattern in networks of connected channels.

SONG, Y., MANNEVILLE, P. & BAROUD, C. N.

16th U.S. National Congress of Theoretical and Applied Mechanics,

June 27-July 2, 2010, State College, Pennsylvania, USA.

The air-liquid flow in a microfluidic airway tree.

SONG, Y., BAUDOIN, M., MANNEVILLE, P. & BAROUD, C. N.

2nd Micro and Nano Flows Conference,

September 1-2, 2009, London, UK.

Airways reopening and cascades of plugs ruptures: an experimental investigation.

BAUDOIN, M., SONG, Y., MANNEVILLE, P. & BAROUD, C. N.

7th International Conference on Nanochannels, Microchannels, and Minichannels,

June 22-24, 2009, Pohang, South Korea.

Reopening of a microfluidic airway tree in the presence of liquid plugs.

Song, Y., Baudoin, M., Manneville, P. & Baroud, C. N.

61st Annual Meeting of the APS Division of Fluid Dynamics,

November 23-25, 2008, San Antonio, Texas, USA.

The air-liquid flow in bifurcating networks of microchannels.

Song, Y., Baudoin, M., Manneville, P. & Baroud, C. N.

7th EUROMECH Fluid Mechanics Conference,

September 14-18, 2008, Manchester, UK.